Université de Montréal

Imagerie à haut contraste et caractérisation d'exoplanètes par la spectroscopie intégrale de champ

par
Jean-François Lavigne

Département de physique
Faculté des arts et des sciences

Thèse présentée à la Faculté des études supérieures
en vue de l'obtention du grade de Philosophiæ Doctor (Ph.D.)
en physique

Novembre, 2009

Université de Montréal
Faculté des études supérieures

Cette thèse intitulée:

Imagerie à haut contraste et caractérisation d'exoplanètes par la spectroscopie intégrale de champ

présentée par:

Jean-François Lavigne

a été évaluée par un jury composé des personnes suivantes:

Pierre Bastien,	président-rapporteur
René Doyon,	directeur de recherche
Jean-Pierre Véran,	codirecteur
Daniel Nadeau,	membre du jury
Kjetil Dohlen,	examinateur externe
François Cavayas,	représentant du doyen de la FES

Thèse acceptée le: . . . . . .

RÉSUMÉ

Cette thèse porte sur l'amélioration des techniques d'imagerie à haut-contraste permettant la détection directe de compagnons à de faibles séparations de leur étoile hôte. Plus précisément, elle s'inscrit dans le développement du *Gemini Planet Imager* (GPI) qui est un instrument de deuxième génération pour les télescopes Gemini. Cette caméra utilisera un spectromètre à champ intégral (SCI) pour caractériser les compagnons détectés et pour réduire le bruit de tavelure limitant leur détection et corrigera la turbulence atmosphérique à un niveau encore jamais atteint en utilisant deux miroirs déformables dans son système d'optique adaptative (OA) : le *woofer* et le *tweeter*. Le *woofer* corrigera les aberrations de basses fréquences spatiales et de grandes amplitudes alors que le *tweeter* compensera les aberrations de plus hautes fréquences ayant une plus faible amplitude.

Dans un premier temps, les performances pouvant être atteintes à l'aide des SCIs présentement en fonction sur les télescopes de 8-10 m sont investiguées en observant le compagnon de l'étoile GQ Lup à l'aide du SCI NIFS et du système OA ALTAIR installés sur le télescope Gemini Nord. La technique de l'imagerie différentielle angulaire (IDA) est utilisée pour atténuer le bruit de tavelure d'un facteur 2 à 6. Les spectres obtenus en bandes JHK ont été utilisés pour contraindre la masse du compagnon par comparaison avec les prédictions des modèles atmosphériques et évolutifs à $8-60\ M_{\rm Jup}$, où $M_{\rm Jup}$ représente la masse de Jupiter. Ainsi, il est déterminé qu'il s'agit plus probablement d'une naine brune que d'une planète.

Comme les SCIs présentement en fonction sont des caméras polyvalentes pouvant être utilisées pour plusieurs domaines de l'astrophysique, leur conception n'a pas été optimisée pour l'imagerie à haut-contraste. Ainsi, la deuxième étape de cette thèse a consisté à concevoir et tester en laboratoire un prototype de SCI optimisé pour cette tâche. Quatre algorithmes de suppression du bruit de tavelure ont été testés sur les données obtenues : la simple différence, la double différence, la déconvolution spectrale ainsi qu'un nouvel algorithme développé au sein de cette thèse baptisé l'algorithme des

spectres jumeaux. Nous trouvons que l'algorithme des spectres jumeaux est le plus performant pour les deux types de compagnons testés : les compagnons méthaniques et non-méthaniques. Le rapport signal-sur-bruit de la détection a été amélioré d'un facteur allant jusqu'à 14 pour un compagnon méthanique et d'un facteur 2 pour un compagnon non-méthanique.

Dernièrement, nous nous intéressons à certains problèmes liés à la séparation de la commande entre deux miroirs déformables dans le système OA de GPI. Nous présentons tout d'abord une méthode utilisant des calculs analytiques et des simulations Monte Carlo pour déterminer les paramètres clés du *woofer* tels que son diamètre, son nombre d'éléments actifs et leur course qui ont ensuite eu des répercussions sur le design général de l'instrument. Ensuite, le système étudié utilisant un reconstructeur de Fourier, nous proposons de séparer la commande entre les deux miroirs dans l'espace de Fourier et de limiter les modes transférés au *woofer* à ceux qu'il peut précisément reproduire. Dans le contexte de GPI, ceci permet de remplacer deux matrices de 1600×69 éléments nécessaires pour une séparation "classique" de la commande par une seule de 45×69 composantes et ainsi d'utiliser un processeur prêt à être utilisé plutôt qu'une architecture informatique plus complexe.

Mots clés: exoplanètes, imagerie à haute gamme dynamique, traitement d'image, instrumentation astronomique, optique adaptative

ABSTRACT

The main goal of this thesis is the improvement of high-contrast imaging techniques enabling the direct detection of faint companions at small separations from their host star. More precisely, it answers some questions linked to the development of the *Gemini Planet Imager* (GPI), a second generation instrument for the Gemini telescopes. This instrument will use an integral field spectrometer (IFS) to characterize the detected faint companions and to attenuate the speckle noise limiting their detection. Moreover, it will use a combination of two deformable mirrors, the woofer and the tweeter, in its adaptive optics (AO) system in order to reach the atmospheric turbulence correction sought. The woofer corrects the low spatial frequency high amplitude aberrations while the ones with a high frequency and a low amplitude are compensated by the tweeter.

First, the high-contrast imaging performance achieved by current on-line IFS on 8-10 m telescopes are investigated through the observation of the faint companion to the star GQ Lup using the IFS NIFS and the AO system ALTAIR presently in function on the telescope Gemini North. The angular differential imaging (ADI) technique is used to reach an attenuation of the speckle noise by a factor of 2 to 6. The JHK spectra obtained were used to constrain the mass of the companion to $8-60\ M_{\rm Jup}$ making it most likely a brown dwarf. $M_{\rm Jup}$ represents the mass of Jupiter.

Current on-line IFS were conceived to be versatile so that they could be used in many astrophysical fields. Hence, their conception was not optimized for high-contrast imaging. The second part of this thesis objective was to build and test in the laboratory an IFS optimized for this task. Four speckle suppression algorithms were tested on the resulting data: the simple difference, the double difference, the spectral deconvolution and a novel algorithm developed in this thesis dubbed the spectral twin algorithm. We found the spectral twin algorithm to be the most efficient to detect both types of companions tested: methanated and non-methanated. The detection signal-to-noise ratio was improved by a factor up to 14 for the methanated companion and up to 2 for a

non-methanated one.

In the last part, problems linked to the wavefront correction split between two deformable mirrors are investigated. First, a method allowing to select the woofer key parameters such as its diameter, its number of actuators and its required stroke which influenced the overall instrument design is presented. Second, since GPI will use a Fourier reconstructor, we propose to split the command in the Fourier domain and to limit the modes sent to the woofer to the ones it can accurately reproduce. In GPI, this results in replacing two matrices of 1600×69 elements in the case of a classic command split scheme by a single matrix of 45×69 components with the proposed method.

Keywords: exoplanets, high-contrast imaging, image processing, astronomical instrumentation

TABLE DES MATIÈRES

LISTE DES TABLEAUX

LISTE DES FIGURES

LISTE DES ANNEXES

LISTE DES SIGLES ET ABRÉVIATIONS

ADI	Angular differential imaging
ALTAIR	ALTitude conjugate Adaptive optics for the InfraRed
AMNH	American Museum of Natural History
AO	Adaptive optics
AS	Actuator Stroke
ASO	Analyseur de surface d'onde
AU	Astronomical unit
BD	Brown dwarf
CIA	Collision induced absorption
CMC	Caméra multi-canale
CONICYT	COmisiòn Nacional de Investigaciòn Científica Y Tecnológica
DD	Double difference
DM	Deformable mirror
DSP	Densité spectrale de puissance
EW	Equivalent width
FÉP	Fonction d'étalement de point
FFT	Fast Fourier transform
FOV	Field of view
FTR	Fourier transform
FWHM	Full-width-at-half-maximum
GPI	Gemini Planet Imager
HARPS	High Accuracy Radial velocity Planet Searcher
HAT	Hungarian-made automated telescope
HST	Hubble Space Telescope
IAS	Inter-actuator stroke

IAU	International Astronomical Union
IDA	Imagerie différentielle angulaire
IDS	Imagerie différentielle spectrale simultanée
IFS	Integral field unit
IHA	Institut Herzberg d'astrophysique
JPL	Jet Propulsion Laboratory
LLNL	Lawrence Livermore National Laboratory
LOCI	Locally optimized combination of images
MCC	Multi-channel camera
MD	Miroir déformable
MEMS	Micro-electrical mechanical system
NACO	Nasmyth Adaptive optics system + COnica
NFIRAOS	Narrow-Field InfraRed Adaptive Optics System
NICMOS	Near-Infrared Camera and Multi-Object Spectrometer
NIFS	Near-infrared Integral Field Spectrometer
NSF	National Science Foundation
OA	Optique adaptative
OSIRIS	OH-Suppressing Infrared Integral Field Spectrograph
PMO	Planetary mass object
PSD	Power spectral density
PSF	Point-spread function
RMS	Root-mean-square
RS	Rapport de Strehl
S/N	Signal-to-noise ratio
SCI	Spectromètre à champ intégral
SDI	Simultaneous spectral differential imaging
SD	Simple difference

SED	Spectral energy distribution
SM	Stroke margin
SOFIA	Stratospheric Observatory For Infrared Astronomy
STD	Standard deviation
TRIDENT	TRiple-Imageur DÉcouvreur de Naine T
UAI	Union Astronomique Internationale
UA	Unité astronomique
UCB	University of California in Berkeley
UCLA	University of California in Los Angeles
UCSC	University of California in Santa Cruz
VLT	Very Large Telescope
VMM	Vector-matrix multiply
WFPC2	Wide-Field Planetary Camera
WFS	Wavefront sensor

REMERCIEMENTS

J'adresse tout d'abord mes sincères remerciements à mon directeur de thèse, René Doyon. Merci pour ta passion contagieuse pour ta recherche et les multiples discussions scientifiques et politiques liés aux différents projets auxquels nous avons participés. J'en ai beaucoup appris et en sort grandi. Je tiens aussi à te remercier pour ta patience et ta persévérance envers un ingénieur qui partait de loin en astrophysique. À mon co-directeur, Jean-Pierre Véran, merci pour m'avoir appris à ne pas pousser la mémé dans les orties quand il y avait une couille dans le fromage. Ton professionnalisme et ton humanisme seront toujours un exemple à suivre pour moi. Je veux aussi remercier Simon Thibault pour avoir supervisé mes débuts à l'INO, Laurent Jolissaint, David Lafrenière et Christian Marois pour leur aide et support durant la réalisation de cette thèse, toute l'équipe de l'IHA pour tous les échanges et discussions. Vous avez tous grandement participé à mon émancipation professionnelle et je vous en serai éternellement reconnaissant. Je me sens aussi extrêmement privilégié d'avoir été entouré d'autant de gens d'excellence, leaders mondiaux dans leur domaine respectif tout au long de ces années.

J'aimerais aussi remercier les différents organismes qui m'ont assuré un support financier pendant la réalisation de ce projet dont le CRSNG, l'ICIP, le CNRC et tout particulièrement, l'INO qui m'a accueilli en son sein avec un intérêt marqué pour mes travaux et avec qui je poursuis maintenant ce périple.

Je ne pourrais pas terminer mes remerciements sans une pensée spéciale pour tous ceux qui m'ont supporté moralement durant toutes ces années. À ma famille, André, Louise et Philippe, merci d'avoir toujours été là même quand j'étais loin de vous. Merci à ma famille d'accueil victorienne, Norm, Kailey et Nan pour m'avoir accueilli dans votre maison et m'y avoir fait sentir autant bienvenu. Finalement, je veux remercier tous mes amis, de longue date comme ceux que j'ai rencontrés dans les différentes villes que j'ai été amené à habiter, pour leur support et leur amitié qui ont donné une dimension humaine inespérée à cette aventure.

CHAPITRE 1

INTRODUCTION

La détection du premier compagnon de masse planétaire en révolution autour de l'étoile de la séquence principale 51 Pegasi par Mayor et Queloz (1995) a ouvert les portes à un nouveau domaine de recherche en astrophysique : l'étude des planètes extra-solaires. Depuis, l'imagerie directe de ces corps par l'isolement de leur lumière de celle de leur étoile hôte est devenue un sujet chaud de l'astrophysique moderne. De telles détections permettront, entre autres, de compléter les données statistiques recueillies par les méthodes indirectes et ainsi de mieux contraindre les mécanismes liés à leur formation. L'accès direct à la lumière de ces planètes permettra aussi d'en obtenir un spectre plus aisément qu'avec les méthodes de détections indirectes et ainsi de mieux connaître les processus physiques régissant leur atmosphère et leur évolution.

L'Union astronomique internationale (UAI) a statué sur une définition de travail d'une planète basée sur sa masse. Cette définition stipule qu'une planète est un objet qui orbite une étoile ou un reste d'étoile et dont la masse est inférieure à 13 $M_{\rm Jup}$, soit la plus faible masse permettant la fusion du deutérium. $M_{\rm Jup}$ représente ici la masse de Jupiter. Un objet ayant une masse supérieure à cette limite, mais inférieure à la masse critique permettant le démarrage de la fusion d'hydrogène (soit $\sim 75\ M_{\rm Jup}$) est une naine brune. Un corps ayant une masse suffisante pour initier la fusion d'hydrogène est une étoile. Un objet de masse planétaire qui n'est pas en orbite autour d'une étoile est un planémo ou une sous-naine brune.

Plusieurs exoplanètes candidates ont été détectées lors des dernières années. Chauvin et al. (2004, 2005a) ont ouvert le bal avec la détection d'un compagnon de masse planétaire ($8 \pm 2\ M_{\rm Jup}$; Mohanty et al., 2007) autour de la naine brune de $5 - 10 \times 10^6$ années 2M1207. Ont suivi les détections du compagnon d'AB Pic ayant une masse de $13 - 14\ M_{\rm Jup}$ (Chauvin et al., 2005b) et de celui de GQ Lup ayant une masse à la limite

entre celle d'une planète et celle d'une naine brune ($1-42\ M_{\rm Jup}$, Neuhäuser et al., 2005 ; $10-20\ M_{\rm Jup}$, Marois et al., 2007 ; $10-40\ M_{\rm Jup}$, McElwain et al., 2007 ; $4-36\ M_{\rm Jup}$, Seifahrt et al., 2007). L'année 2008 a été particulièrement fructueuse avec, tout d'abord, la détection confirmée des premières exoplanètes dans le système orbitant autour de HR8799 (Marois et al., 2008) qui en compte trois ($\sim 7\ M_{\rm Jup}$, $\sim 10\ M_{\rm Jup}$, $\sim 10\ M_{\rm Jup}$) et d'une autre autour de Fomalhaut ($< 3\ M_{\rm Jup}$; Kalas et al., 2008) ainsi que de deux planètes potentielles nécessitant une seconde observation pour confirmer leur lien gravitationnel avec leur étoile hôte, soit le compagnon de $8^{+4}_{-2}\ M_{\rm Jup}$ de 1RXS J160929.1 (Lafrenière et al., 2008) et celui de β *Pic* ayant une masse évaluée à $\sim 8\ M_{\rm Jup}$ (Lagrange et al., 2008).

Le faible nombre de détections directes d'exoplanètes à ce jour s'explique principalement par la grande différence de luminosité entre celles-ci et leur étoile hôte et la grande proximité des deux objets. La détection de planètes est alors limitée par la lumière parasite de l'étoile hôte. Les techniques actuelles permettent l'investigation des régions externes des systèmes planétaires. Ainsi, différents sondages tels que ceux menés par Lafrenière et al. (2007a) et Biller et al. (2007) ont permis de mettre les premières contraintes statistiques sur ces régions par leur non-détection d'objets. Lafrenière et al. (2007a) observent 85 étoiles et trouvent, avec une certitude de 95 %, qu'une limite maximale de 28 % des étoiles ont des planètes ayant des masses se situant entre 0.5 et 13 $M_{\rm Jup}$ à des séparations entre 10 et 25 UA, qu'au plus 13 % en possèdent entre 25 et 50 UA et 9.3 % entre 50 et 250 UA. De son côté, Nielsen et al. (2008) utilisent les données recueillies par Biller et al. (2007) sur 59 jeunes étoiles pour déterminer avec une certitude de 95 % que 20 % ou moins des étoiles possèdent des planètes ayant une masse supérieure à $4\ M_{\rm Jup}$ entre 20 et 100 UA. L'amélioration de ces statistiques passe alors nécessairement par l'amélioration des techniques instrumentales et de traitement d'image permettant de réduire cette lumière parasite et ainsi d'investiguer des régions se situant à de plus faibles séparations et d'être sensible à des objets de plus faible luminosité.

Dans ce chapitre, une revue des connaissances acquises à l'aide des méthodes de dé-

tection indirectes est tout d'abord présentée. Il sera ensuite question des objectifs scientifiques liés à la détection d'exoplanètes qui seront suivis par une description des différentes techniques instrumentales permettant de réduire la lumière parasite de l'étoile hôte. Finalement, la recherche effectuée dans cette thèse sera située dans le contexte général de l'imagerie directe d'exoplanètes.

1.1 Méthodes indirectes

1.1.1 Vitesse radiale

La détection de planètes par la mesure des variations périodiques de la vitesse radiale en utilisant l'effet Doppler a été la plus prolifique des méthodes indirectes avec l'identification de plus de 90% des exoplanètes connues. Cette technique permet la mesure de $M_p \sin i$ où M_p est la masse de la planète et i est l'inclinaison de son orbite par rapport à la ligne de visée (i=90° correspondant à une orbite dans le plan de la ligne de visée). La confirmation d'une détection nécessite une orbite complète de la planète pour assurer la périodicité des variations détectées. La séparation maximale entre une planète pouvant être détectée et son étoile hôte en UA, a, est alors calculée à l'aide de la 3e loi de Kepler : $a^3 = (M_s + M_p)P^2$ où M_s est la masse de l'étoile hôte en unité de masse solaire et P est la période de révolution de la planète en années. Ainsi, la recherche de compagnons de faible masse autour d'étoiles de masse solaire est présentement limitée à une séparation de ~ 6 UA et augmentera à ~ 8.5 UA dans 10 ans. Cette technique est aussi présentement limitée aux étoiles sans pulsations, qui n'ont pas d'activité de surface importante, qui ne sont pas binaires et qui n'ont pas un taux de rotation élevé. Certains sondages notables utilisant cette technique sont le sondage du Lick+Keck+AAT (Marcy et al., 2005) observant 1330 étoiles FGKM, CORALIE (Udry et al., 2000) qui investigue 1650 étoiles de type FGK et son expansion HARPS (Mayor et al., 2003) sondant 1200 étoiles tout en élargissant le champ de recherche aux étoiles de type spectral M.

Udry & Santos (2007) présentent une revue des statistiques des planètes trouvées essentiellement par ces derniers sondages. Ainsi, $\sim 1\%$ des étoiles possèdent des Jupiters chaudes situées à des rayons < 0.1 UA et $\sim 6\%$ d'étoiles sont pourvues de planètes géantes gazeuses à des rayons < 5 UA. La loi que semble suivre le nombre de planètes géantes gazeuses ayant une masse donnée est $dN/dM_p \propto M_p^{-1.05}$ (Marcy et al., 2005) favorisant ainsi les planètes de plus faible masse.

1.1.2 Transit

La seconde méthode indirecte consiste à détecter les variations photométriques périodiques induites par l'éclipse de l'étoile primaire par le passage du compagnon entre celle-ci et l'observateur. Cette technique qui ne comptait qu'une quinzaine de détections avant 2007 en possède maintenant 52 à son actif depuis la mise en service de nouveaux systèmes de sondage à grand champ tels que XO (McCullough et al., 2005), HAT (Bakos et al., 2002) et SuperWASP (Pollacco et al., 2006). Cette technique est, comme la précédente, biaisée vers les planètes se situant à de courtes séparations de leur étoile hôte dû à la décroissance exponentielle de la probabilité qu'une planète se situe sur une orbite éclipsant son étoile hôte avec une séparation croissante. Elle permet toutefois d'obtenir des informations supplémentaires sur la planète. Les paramètres orbitaux tels que i, et donc la masse, et le rayon de la planète peuvent être déterminés suite à une analyse de la courbe photométrique obtenue. La densité de la planète est ensuite calculée à l'aide de ces paramètres.

Deux méthodes permettent aussi l'étude spectroscopique de l'atmosphère de ces exoplanètes. La première est la spectroscopie de transmission (Charbonneau et al., 2002) qui consiste à différencier les spectres de l'étoile obtenus pendant et hors transit pour obtenir de l'information sur les variations spectrales de transmission de l'atmosphère planétaire causées par l'absorption de ses atomes et molécules. La deuxième technique consiste à différencier un spectre observé lors de l'éclipse secondaire, c'est-à-dire lorsque le compagnon est occulté par l'étoile hôte, et un spectre avant ou après cette éclipse pour

mesurer le spectre réfléchi par le compagnon. Le transit des planètes permet donc non seulement la comparaison de la densité des planètes observées avec les prédictions des modèles atmosphériques de planètes irradiées, mais aussi d'obtenir les premières mesures spectrales de ces mondes.

1.1.3 Microlentilles gravitationnelles

La dernière méthode indirecte ayant permis la détection d'exoplanètes à ce jour est l'amplification par microlentilles gravitationnelles. Dans ce cas-ci, un système planétaire amplifie la lumière d'une étoile de fond en déviant les rayons lumineux vers l'observateur par l'action de sa gravité. Un premier pic d'intensité est détecté lors de l'amplification causée par l'étoile hôte et un second pic de moindre importance est détecté lors de l'amplification causée par l'exoplanète. Cette technique nécessite un alignement précis de l'observateur, du système planétaire et de l'étoile de fond qui est improbable, mais non impossible dû à la grande quantité d'étoiles présentes dans la galaxie. Huit planètes ont été détectées en utilisant cette méthode (e.g. Bond et al., 2004; Beaulieu et al., 2006; Gaudi et al., 2008). Son désavantage principal est que l'alignement des trois étoiles ne se produit qu'une fois, ne laissant qu'une chance pour effectuer la mesure. Elle permet la détermination de la masse, du demi-grand axe et de la période de la planète suite à une analyse méticuleuse de la courbe de lumière amplifiée.

1.2 Modèles évolutifs et atmosphériques

Bien que la définition de travail d'une planète telle que dictée par l'UAI soit basée sur sa masse, la détermination observationnelle de ce paramètre est complexe. La technique la plus directe permettant de mesurer la masse d'un objet céleste en orbite autour d'un second est de tracer les orbites de ces deux objets autour du centre de masse du système. Or, l'étoile hôte étant habituellement significativement plus massive qu'une planète, son déplacement autour du centre de masse est faible, rendant généralement les mesures as-

trométriques sous les limites des instruments actuels. Le croisement entre les techniques indirectes de détection des planètes et leur imagerie directe pourra aussi permettre de déterminer précisément leur masse. Par contre, ces deux méthodes explorent présentement des régions orbitales significativement différentes. De plus, les méthodes indirectes sont utilisées sur des étoiles évoluées stables alors que l'imagerie directe est plus sensible aux planètes jeunes. L'amélioration des techniques d'imagerie directe qui permettront de sonder des régions orbitales à plus faible séparation et de détecter des compagnons de plus faible intensité rendra ainsi possible le recoupement de ces méthodes.

Actuellement, les masses des exoplanètes sont plutôt déterminées en comparant certains de leurs paramètres observationnels avec les prédictions des modèles évolutifs et atmosphériques. Ces modèles prédisent les variations de différents paramètres observationnels en fonction de la masse et de l'âge de l'objet observé. Burrows et al. (2001) font une revue des mécanismes impliqués dans l'évolution d'objets de différentes masses qui sont ici résumés. Un corps de masse stellaire légèrement supérieure à $\sim 75\ M_{\rm Jup}$ se refroidit, se contracte et sa luminosité diminue jusqu'à ce que l'énergie générée par la fusion d'hydrogène en son cœur s'équilibre avec la perte d'énergie sous forme de radiation. Dans le cas de naines brunes, la fusion de deutérium est initiée et elle ralentit la contraction pendant quelques millions d'années. La pression de radiation étant insuffisante pour contrer la gravité après cette période, les naines brunes poursuivent leur contraction jusqu'à ce que la force de dégénérescence des électrons l'arrête à $\sim\ 1\ R_{\rm Jup}$ où $R_{\rm Jup}$ est le rayon de Jupiter. L'évolution des objets de masse planétaire est similaire, mais sans l'impact de la fusion du deutérium. Les principaux modèles évolutifs sont donnés par le groupe de Tucson (Burrows et al., 1997) et de Lyon (Chabrier et al., 2000; Baraffe et al., 2003). Les courbes de l'évolution de la luminosité, L, et du rayon, R, telles que données par le modèle de Chabrier et al. (2000) sont présentées à la Figure 1.1.

La distribution spectrale de la luminosité d'un objet est déterminée à l'aide de modèles atmosphériques. Ces derniers utilisent les profils de température et de pression de l'atmosphère, la position des zones de convection et de radiation et l'opacité des

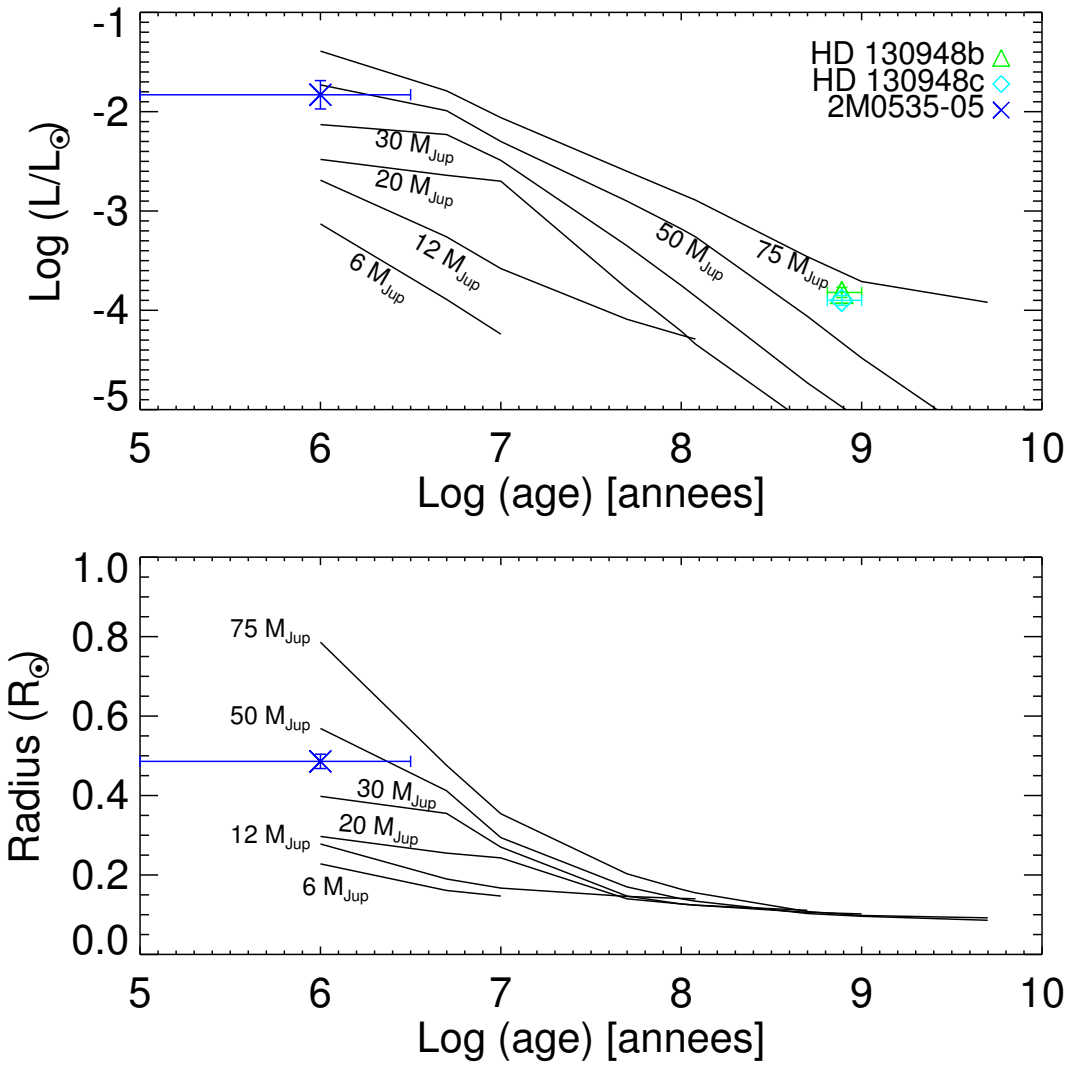

Figure 1.1 Évolution de la luminosité (figure du haut) et du rayon (figure du bas) d'un corps en fonction de son âge et de sa masse. Les objets 2M0535-05, HD 130948b et c ayant une masse déterminée indépendamment des modèles sont aussi illustrés.

différentes espèces présentes pour déterminer la nature des éléments présents dans la photosphère et le spectre émergeant. De façon générale, les éléments les plus abondants sont aussi ceux qui contribuent le plus à l'opacité de l'atmosphère. Ainsi, l'oxyde de titane (TiO), l'oxyde de vanadium (VO), le H_2O, le CO et les grains de silicates dominent l'opacité pour des atmosphères ayant des températures effectives (T_{eff}) supérieures à

$\sim$ 2000 K. Sous cette température, le TiO et le VO condensent et disparaissent de la photosphère. Les sources principales d'opacité deviennent alors le H_2O, le CH_4, le NH_3, le H_2 et les raies alcalines à des T_{eff} sous $\sim$ 1500 K. La formation de nuages de H_2O dans la photosphère d'objets étant à des $T_{eff} <$ 500 K suivie par l'apparition de nuages de NH_3 à des $T_{eff} <$ 200 K dominent l'opacité des corps de plus faible température.

L'absorption induite par les collisions du H_2 et les transitions rotationnelles du H_2O et du CH_4 jouent aussi un rôle majeur dans le spectre émergeant des objets sous-stellaires. Ils ont pour effet de déplacer le flux idéal du corps noir des longueurs d'ondes > 10 μm vers les plus courtes (> 1 μm) résultant en un flux deux à cinq fois plus important dans ces régions spectrales améliorant ainsi les chances de détection de ces compagnons à ces longueurs d'onde. La combinaison des modèles évolutifs et atmosphériques permettent de prédire le spectre d'un objet en fonction de son âge et de sa masse. Le spectre d'un objet ayant une masse de 1 $M_{\rm Jup}$ à différents âges est illustré à la Figure 1.2.

Seuls quelques objets ont permis de tester ces modèles à ce jour à l'aide d'une détermination indépendante de leur masse. De ceux-ci, seuls HD 130948B et C (Dupuy et al., 2009) ont un âge qui a pu être déterminé précisément à l'aide de la gyrochronologie de leur étoile hôte HD 130948A ($0.79^{+0.22}_{-0.15}$ Gyr) ainsi qu'une mesure de leur luminosité et une mesure dynamique de leur masse (masse totale des deux objets = 114 ± 2 $M_{\rm Jup}$, rapport de masse déterminé à l'aide des modèles évolutifs = 0.962 ± 0.003). Ce test démontre que les modèles évolutifs du groupe de Lyon et de Tucson prédisent une luminosité deux à trois fois plus faible que les observations. De plus, la température effective prédite par les modèles évolutifs et atmosphériques diffère de 150 à 300 K démontrant qu'au moins un des deux types de modèles souffre d'erreurs systématiques.

Un second système digne de mention est la binaire éclipsante 2M0535-05 (Stassun et al., 2006, 2007) âgée de 1^{+2}_{-1} Myr. Ces deux objets ont des masses de 36 ± 3 $M_{\rm Jup}$ (A) et de 57 ± 5 $M_{\rm Jup}$ (B). Avec leur jeune âge, ils permettent de tester les modèles évolutifs qui sont incertains au-dessous de $\sim 10^7$ années, ceux-ci étant dépendant des conditions initiales utilisées (Baraffe et al., 2002). Ce test montre que la luminosité de

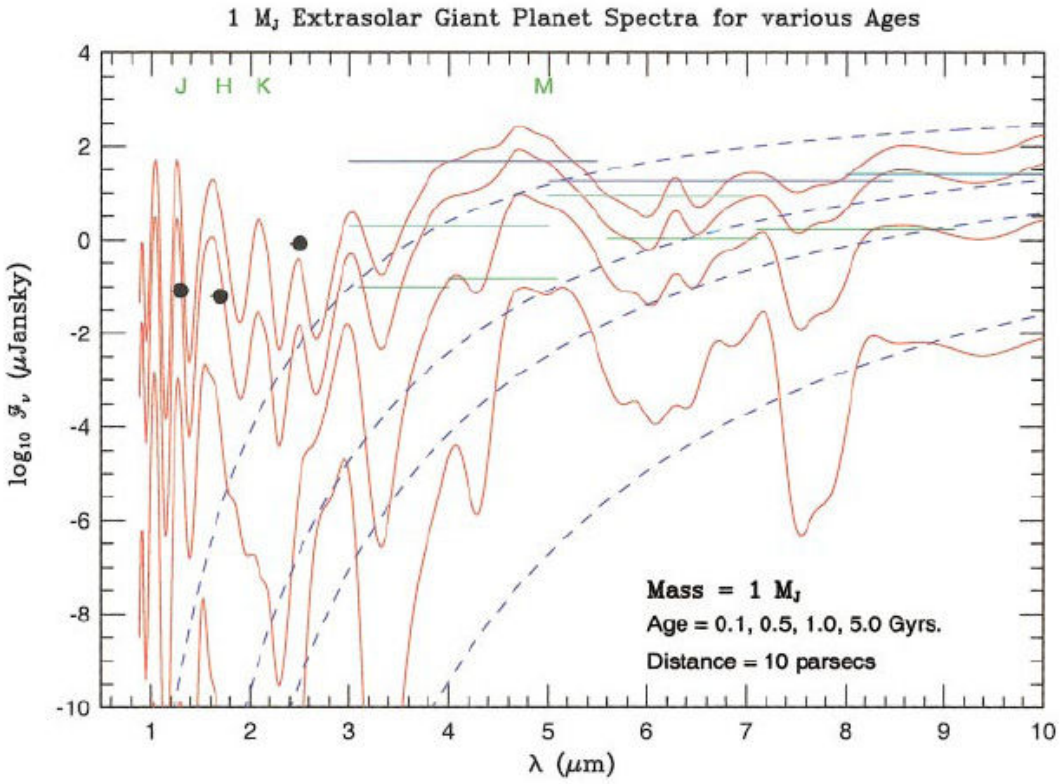

Figure 1.2 Flux en fonction de la longueur d'onde pour une planète isolée de 1 $M_{\rm Jup}$ à différents âges. Les spectres du corps noir associés à chaque courbe spectrale y sont représentés pour comparaison (tirets bleus). Une approximation de la sensibilité pouvant être atteinte avec NICMOS (ligne noire), SPITZER (ligne olive), Gemini (ligne verte pâle) et SOFIA (ligne bleue) est aussi illustrée ainsi que les bandes infrarouges J, H, K et M (figure tirée de Burrows et al. (2001)).

l'objet le moins massif est sous-estimée par les modèles évolutifs du groupe de Lyon par un facteur ~ 1.5. De son côté, l'objet le plus massif est significativement moins lumineux que la prédiction des modèles. Cette différence pourrait s'expliquer si les deux objets n'ont pas le même âge ou encore par la présence d'un champ magnétique important dans l'objet le plus massif qui aurait influencé son évolution. Dû à cette incertitude, seul l'objet moins massif est illustré à la Figure 1.1 pour une comparaison avec les prédictions des modèles évolutifs. L'éclipse de ces deux objets permet aussi d'obtenir une mesure directe de leur rayon (A : $0.486 \pm 0.018\ R_\odot$ et B : $0.675 \pm 0.023\ R_\odot$). La comparaison

avec les prédictions du modèle de Lyon démontre que ce dernier sous-évalue les rayons de $\sim 10\%$.

La dépendance des modèles évolutifs envers les conditions initiales utilisées est particulièrement importante pour la prédiction de la luminosité des jeunes planètes. En effet, Marley et al. (2007) démontrent qu'une planète formée par le scénario d'accrétion d'un cœur solide pourrait avoir une luminosité jusqu'à $\sim 10^3$ fois plus faible que celle prédite par les modèles actuels. Il sera donc d'autant plus important d'obtenir des images des planètes à de faibles distances de leur étoile hôte afin de mesurer dynamiquement leur masse tout en obtenant des données spectrales permettant de tester ces modèles.

Ainsi, l'amélioration des techniques d'imagerie directe des exoplanètes permettra éventuellement un recoupement avec les techniques indirectes de détection qui, à son tour, permettra de mieux tester les modèles évolutifs et atmosphériques et de mieux comprendre les phénomènes physiques en cause. Les modèles pourront être améliorés en conséquence pour une détermination plus précise de la masse des objets.

1.3 Formation

La comparaison des données statistiques recueillies sur les exoplanètes avec les prédictions des différents modèles de formation permettra de mieux comprendre et contraindre les processus physiques menant à l'existence de ces corps. Deux théories principales permettent d'expliquer les processus menant à la formation des planètes géantes gazeuses : par agglomération d'un cœur solide suivi de la capture de gaz et, par fragmentation du disque protoplanétaire. Le premier constitue le modèle canonique de formation des planètes terrestres et gazeuses du système solaire tandis que le deuxième ne concerne que la formation des planètes gazeuses.

Dans le modèle d'accrétion, un cœur solide se forme par l'accrétion et l'agglomération de grains de poussières dans le disque protoplanétaire entourant l'étoile naissante. Dans les régions internes du disque qui sont dénuées de gaz dû à la pression de radia-

tion exercée par l'étoile, ce processus mène à la formation de planètes terrestres comme celles du système solaire. Dans les régions externes, au-delà de la *snow line* où le gaz et la glace abondent, la formation d'un cœur rocheux de quelques masses terrestres est suivie d'une accrétion rapide, par capture gravitationnelle, du gaz environnant, menant à la formation d'une planète gazeuse (Perri & Cameron, 1974; Mizuno, 1980; Lissauer, 2001, 2006). Bien que les mécanismes menant à la formation de planétésimaux à l'échelle du kilomètre ne soient pas encore bien compris, la formation d'agglomérats de poussières jusqu'à une échelle du décimètre est prouvée expérimentalement (Blum & Wurm, 2008). Une difficulté des premiers modèles d'accrétion était qu'ils prédisaient des temps de formation beaucoup trop long – de l'ordre de plusieurs dizaines de millions d'années – en contradiction avec les données observationnelles qui suggéraient plutôt des temps de vie de quelques millions d'années pour les disques protoplanétaires (Bally et al., 1998; Briceño et al., 2001; Haisch et al., 2001). Aujourd'hui, les simulations et tests expérimentaux suggèrent des temps de formation de l'ordre du million d'années (Lissauer, 2001; Alibert et al., 2005), en accord avec les observations. Comme la densité de gaz et de poussière décroit rapidement avec le rayon du disque, la formation de planètes gazeuses par accrétion est fort probablement restreinte à des distances orbitales inférieures à ~ 20 UA.

Une alternative au modèle d'accrétion, initialement proposée par Cameron (1978) et réintroduite par Boss (1997, 2001), est la formation d'instabilités gravitationnelles dans le disque protoplanétaire. Ces dernières entraînent la formation de nœuds denses qui s'effondrent pour former la planète dans un processus qui s'apparente à la formation des étoiles et des naines brunes. Une revue récente de ce processus, dont le texte qui suit s'inspire, est présentée par Durisen et al. (2007). Les simulations récentes ont permis de mettre en évidence l'importance des processus de chauffage et de refroidissement dans la formation des nœuds denses. Or, le traitement adéquat de ces processus nécessite une connaissance détaillée des sources externes de radiation et de leur influence sur le disque à chaque position, du taux de perte d'énergie du disque causée par le refroidissement ra-

diatif, des processus dynamiques qui produisent une augmentation de la température du disque par la viscosité et les chocs et d'une équation d'état détaillée permettant d'évaluer la quantité d'énergie introduite par ces processus. Un traitement détaillé de tous ces processus physiques est au-delà des capacités des modèles actuels. De plus, le traitement adéquat des processus thermiques nécessite une bonne connaissance des propriétés physiques des disques protoplanétaires (composition, taille des grains de poussières et leur distribution spatiale) qui demeurent encore peu contraintes observationnellement. Les simulations d'instabilités gravitationnelles démontrent que des planètes gazeuses peuvent être formées très rapidement ($\sim 10^3$ années ; Mayer et al., 2002) à des séparations orbitales allant jusqu'à 20-30 UA autour d'étoiles de masse solaire.

Des tests observationnels de ces modèles seront nécessaires pour identifier le processus menant à la formation des planètes géantes gazeuses ou pour mieux comprendre les limites de chaque processus dans le cas où les deux se retrouvent dans la nature. Une première prédiction est celle de Laughlin et al. (2004) qui trouvent que le processus d'accrétion nécessite plus de 10^7 années pour former des planètes géantes gazeuses autour d'étoiles de type M et que ces planètes devraient donc y être rares alors que Boss (2006) trouve qu'il est beaucoup plus probable que de telles planètes se forment par instabilité gravitationnelle autour de ce type d'étoile. Aussi, l'observation de planètes géantes gazeuses à des séparations de plus de $\sim$ 10 UA autour d'étoiles de faible métallicité serait largement en faveur de la formation de planètes par instabilités gravitationnelles. L'observation de disques protoplanétaires plus lisses ou une diminution importante du nombre de ce type de planètes au-delà de $\sim$ 5 UA serait plutôt en faveur du modèle d'accrétion.

Un fait intéressant est que les données présentement recueillies par les sondages de détection indirecte montrent une corrélation entre la métallicité des étoiles et la présence d'exoplanètes ce qui semble appuyer la théorie de l'accrétion d'un cœur solide. Par contre, une partie de cette corrélation pourrait être due à un biais observationnel favorisant la détection de planètes par vitesse radiale autour d'étoiles ayant des raies mé-

talliques bien définies et, donc, de métallicité supérieure. Jones (2004) et Sozzetti (2004) démontrent à l'aide des données de ces sondages que les étoiles hôtes ayant une métallicité importante sont aussi plus susceptibles de posséder une planète géante gazeuse en orbite à faible rayon. Ceci serait causé par une plus grande efficacité du processus de migration chez les étoiles de métallicité supérieure. Ainsi, les sondages indirects étant biaisés vers les planètes à plus faible rayon, la corrélation observée pourrait plutôt être causée par la plus grande efficacité du processus migratoire pour les étoiles de plus grande métallicité.

1.4 Instrumentation liée à l'imagerie directe d'exoplanètes

Tel que discuté précédemment, le sondage des régions externes des systèmes planétaires, qui permettra de mieux connaître les processus de formation des planètes ainsi que de tester et d'améliorer les modèles évolutifs et atmosphériques, passe nécessairement par l'amélioration des techniques d'imagerie directe de ces corps. Ces différentes techniques sont revues dans cette section.

1.4.1 Description de la fonction d'étalement de point

Le facteur principal limitant la détection directe d'exoplanètes est la distribution de l'intensité de l'étoile hôte (sa fonction d'étalement de point ; FÉP) dans le plan image du télescope. Dans le cas idéal où aucune surface du système n'a de défauts optiques, la FÉP est donnée par l'approximation du champ lointain de la diffraction de Fraunhofer. Elle est alors donnée par le carré de la transformée de Fourier de la fonction d'illumination de la pupille du télescope. La largeur à mi-hauteur de la FÉP obtenue est alors de λ/D où λ est la longueur d'onde observée et D est le diamètre du miroir primaire du télescope. Les défauts optiques ont pour effet d'introduire des tavelures dans la FÉP. Ces tavelures évoluent selon les variations d'alignement des composantes optiques causées, par exemple, par des variations de température ou encore des variations de flexion

du télescope. Elles ont des temps de vie typiques allant de quelques minutes à quelques heures et sont généralement appelées tavelures quasi-statiques.

La FÉP d'un télescope au sol est aussi dépendante de la déformation du front d'onde introduite par la turbulence de l'atmosphère terrestre. On réfère le lecteur à Roddier (1981) pour une discussion détaillée de l'effet de la turbulence atmosphérique sur l'observation astronomique. Cette déformation du front d'onde est introduite par des variations locales de l'indice de réfraction de l'air le long de la ligne de visée causées par la turbulence qui mélange des zones atmosphériques ayant différentes températures et différentes concentrations de vapeur d'eau. La largeur à mi-hauteur de la FÉP limitée par la turbulence atmosphérique, aussi appelée *seeing* (w_0), devient alors $\lambda/r_0(\lambda)$ où $r_0(\lambda)$ est le paramètre de Fried ou la longueur de cohérence spatiale de l'atmosphère. Ce paramètre dépend de la longueur d'onde, $r_0 \propto \lambda^{6/5}$ et est typiquement $r_0(0.5\ \mu\text{m}) \approx 0.15$ m et $w_0 \approx 0.7$ arcsec aux bons sites astronomiques. La déformation du front d'onde par l'atmosphère introduit aussi des tavelures dans la FÉP qui ont des temps de vie de l'ordre de la milliseconde.

La turbulence atmosphérique est généralement représentée par le modèle de Kolmogorov et la distribution de la variance du front d'onde en fonction de la fréquence spatiale η ou la densité spectrale de puissance (DSP), nous est donnée par :

$$W_\phi(\eta) = 0.023 r_0^{-5/3} \eta^{-11/3}, \tag{1.1}$$

ou encore par le spectre de von Karman dans le cas où la limite supérieure L_0 de la dimension d'une cellule turbulente est considérée :

$$W_\phi(\eta) = 0.023 r_0^{-5/3} (\eta^2 + L_0^{-2})^{-11/6}. \tag{1.2}$$

La variance de la déformation du front d'onde introduite par l'atmosphère décroît donc exponentiellement avec une fréquence spatiale croissante.

1.4.2 Correction de la turbulence atmosphérique

La pleine résolution du télescope peut être retrouvée à l'aide d'un système d'optique adaptative (OA) qui compense la turbulence atmosphérique en observant une étoile guide. Ce type de système opère en boucle fermée à l'aide d'un miroir déformable (MD) qui corrige le front d'onde, d'un analyseur de surface d'onde (ASO) détectant la déformation résiduelle du front d'onde provenant de l'étoile après sa correction par le MD et d'un ordinateur de contrôle ou un reconstructeur de front d'onde qui transforme les déformations lues par l'ASO en commandes à appliquer au MD. Ce MD possède n_{MD} degrés de libertés qui correspondent au nombre d'éléments actifs (les actionneurs) utilisés pour déformer sa surface.

Le contrôle de ces actionneurs peut être implémenté selon deux approches principales. Un contrôle zonal associe chaque actionneur à une zone de l'ASO et les contrôle individuellement avec un gain qui leur est propre. Le problème principal associé à cette approche est que la déformation induite par un actionneur donné est couplée aux commandes appliquées à ses voisins ; ceci nécessite donc des calculs complexes pour trouver la juste commande. Il est donc plus commun d'utiliser un contrôle modal. Ce type de contrôle utilise une base de modes orthogonaux. Ceci permet de découpler chaque mode et, ainsi, d'utiliser une boucle de contrôle indépendante pour chacun. Le gain de chaque boucle peut alors être ajusté indépendamment pour optimiser la commande (Gendron & Léna, 1994a,b; Dessenne et al., 1998; Ellerbroek & Rhoadarmer, 1997, 2001). Les bases modales typiques utilisées en OA sont les fonctions de Karhunen-Loève (Fried, 1978), les polynômes de Zernike (Noll, 1976) et les modes de Fourier (e.g. Freischlad & Koliopoulos, 1985; Poyneer et al., 2002). Par exemple, un tel système de contrôle automatisé a été implémenté dans le système OA PUEO sur le télescope Canada-France-Hawaï (Rigaut et al., 1998) et le système ALTAIR sur le télescope Gemini Nord (Herriot et al., 1998).

Plus précisément, un vecteur $\vec{s}_{ASO}$ contenant les n_{ASO} déformations du front d'onde

lues dans chaque sous-ouverture de l'ASO est transformé en un vecteur ($\vec{c}_{MD}$) de n_{MD} commandes à être appliquées aux actionneurs du miroir déformable par une multiplication par une matrice (M) de dimensions $n_{MD} \times n_{ASO}$:

$$\vec{c}_{MD} = M \cdot \vec{s}_{ASO}. \tag{1.3}$$

M est construite à partir de la multiplication de trois matrices. La première de celles-ci, la matrice STM, est utilisée pour transformer $\vec{s}_{ASO}$ en un vecteur de coefficients modaux ($\vec{m}$). La deuxième, G, est une matrice diagonale contenant les gains à être appliqués à chaque mode. La dernière matrice, MTA, transforme les coefficients modaux multipliés par les gains en commandes à être appliquées aux actionneurs. En multipliant ces matrices, on obtient :

$$M = MTA * G * STM. \tag{1.4}$$

Le nombre d'opérations effectuées pour calculer les commandes à être appliquées au MD est alors proportionnel à n_{MD}^2 en considérant que $n_{MD} \approx n_{ASO}$. Lorsque le gain est optimisé, une nouvelle matrice M est calculée hors-ligne et remplace ensuite l'ancienne dans l'équation 1.3. Dans le cas précis de l'utilisation d'un reconstructeur de Fourier, la matrice M n'est pas calculée. Les matrices MTA et STM sont plutôt remplacées par des transformées de Fourier rapides nécessitant un nombre de calculs proportionnel à $n \log\, n$.

Le nombre de degrés de liberté du MD étant fini, les modes au-dessus de sa fréquence de coupure ne sont pas corrigés par celui-ci résultant en une erreur résiduelle sur le front d'onde atmosphérique (σ_{Spa}). Cette dernière est donnée par Noll (1976) pour une correction des n_{zer} premiers polynômes de Zernike. Elle peut aussi être calculée en considérant que le MD agit comme un filtre spatial ayant une fréquence de coupure $\eta_c = 1/d$ où d est l'espace inter-actionneur pour les modes de Fourier. Il suffit alors d'intégrer

la DSP ($W_\phi(\eta)$) résiduelle pour calculer l'erreur résiduelle sur le front d'onde :

$$\sigma^2_{Spa} = \int_{\eta_c}^{\infty} W_\phi(\eta) d\eta. \tag{1.5}$$

À cette erreur s'ajoutent, entre autres, l'erreur de retard de boucle due à l'évolution de l'atmosphère entre le moment auquel le front d'onde est lu et le moment auquel il est corrigé, les erreurs de modélisation du MD, le bruit sur la lecture du front d'onde introduit par l'ASO et le bruit de repliement spatial dû à l'échantillonnage spatial fini de l'ASO. Le résultat est une FÉP généralement modélisée par un cœur limité par la diffraction et un halo atmosphérique résultant des aberrations non compensées. Les performances du système d'OA sont traditionnellement exprimées sous forme de rapport de Strehl (RS) qui correspond au pic d'intensité de la FÉP obtenue divisé par le pic d'intensité d'une FÉP "parfaite" limitée par la diffraction.

1.4.3 Atténuation de la FÉP de l'étoile hôte

Racine et al. (1999) ont identifié les tavelures présentes dans la FÉP comme étant la principale source de bruit limitant la détection directe de compagnons. Ce bruit de tavelure suit les statistiques des petits nombres et suit donc la loi de Poisson. Sa variance, σ^2_{tav}, est alors proportionnelle au nombre de réalisations indépendantes du patron de tavelure et dépend aussi de l'amplitude de la variation d'intensité qu'elles introduisent. Ils trouvent que :

$$\sigma^2_{tav} \simeq \frac{F_s^2}{16} \frac{t}{\tau_0}, \tag{1.6}$$

où F_s est le flux dans une tavelure à un rayon donné de la FÉP, t est le temps d'observation et τ_0 est le temps de vie caractéristique des tavelures. Ainsi, les tavelures quasi-statiques provenant des erreurs sur les surfaces optiques du télescope sont plus dommageables que les tavelures atmosphériques ayant un temps de vie significativement plus court lorsque $t \gg (\tau_0)_{atm}$.

Une première approche possible pour réduire ce bruit de tavelure est de l'atténuer à

sa source. Ceci peut se faire en réduisant les défauts sur les surfaces optiques et en améliorant la correction du front d'onde à l'aide du système d'OA. Une meilleure correction du front d'onde à l'aide du système d'OA permet d'atteindre un RS plus élevé et permet ainsi d'atténuer le bruit de tavelure en réduisant F_s dans l'équation 1.6. De plus, la coronographie peut être utilisée pour atténuer la figure de diffraction du télescope et le bruit de tavelure lorsqu'un RS supérieur à ~ 0.8 est atteint (Sivaramakrishnan et al., 2001). Cette technique consiste à utiliser une combinaison de masques dans le plan focal et le plan pupille afin d'atténuer l'intensité de l'étoile primaire en affectant le moins possible le flux du compagnon (Lyot, 1939). Une panoplie de combinaisons de masques ont été proposées ces dernières années pour atteindre ce but (e.g. Kasdin et al., 2003; Guyon, 2003; Soummer, 2005).

Une seconde approche non exclusive à la première est de soustraire une FÉP de référence de celle de l'étoile observée pour réduire F_s. Cette FÉP peut être construite en observant une étoile de référence, en observant une étoile à différentes polarisations pour distinguer la lumière non-polarisée émise par l'étoile de la lumière polarisée réfléchie par une planète, en utilisant la corrélation spectrale des tavelures en observant une étoile à différentes longueurs d'onde ou encore en utilisant le long temps de vie des tavelures quasi-statiques pour observer une étoile avec différentes orientations du champ de vue.

En particulier, l'imagerie différentielle spectrale simultanée (IDSS ; Marois et al., 2005), tirant avantage de la corrélation spectrale des tavelures, et l'imagerie différentielle angulaire (IDA ; Marois et al., 2006; Lafrenière et al., 2007b), utilisant la corrélation temporelle des tavelures quasi-statiques, sont abordées dans cette thèse et sont ici détaillées. L'IDSS consiste à acquérir des images à différentes longueurs d'onde et à utiliser une différence de signature spectrales entre le compagnon et son étoile hôte pour différencier un compagnon des tavelures de la FÉP de l'étoile hôte. Ceci peut se faire à l'aide d'une caméra multi-canaux (CMC) qui permet l'imagerie de la FÉP à différentes longueurs d'onde en utilisant différents canaux optiques. Généralement, ces caméras sont utilisées pour la recherche de compagnons méthaniques et la FÉP de référence est

construite à l'aide d'images prises dans la bande d'absorption du méthane autour de 1.6 μm alors que la FÉP dans laquelle le compagnon est recherché est prise hors de celle-ci.

La dimension de la FÉP étant proportionnelle à la longueur d'onde, les tavelures se déplacent radialement en fonction de la longueur d'onde alors que le compagnon reste fixe, sa position étant déterminée par sa position dans le champ de vue. Cette différence de déplacement radial entre le compagnon et les tavelures peut aussi être exploitée pour les différencier. Les FÉP sont alors mises à la même échelle et différenciées pour atténuer le bruit de tavelure. Si un compagnon est recherché à un rayon de $r = n\lambda/D$ rad et qu'un déplacement radial minimal du compagnon de λ/D est nécessaire pour éviter qu'il y ait une perte significative du flux du compagnon lors de la soustraction des images, l'intervalle de longueur d'onde entre les deux images soustraites doit alors être : $\Delta\lambda = \lambda/n$.

Sparks & Ford (2002) ont proposé l'utilisation d'un spectromètre à champ intégral pour acquérir les FÉP à différentes longueurs d'onde. L'utilisation d'une telle caméra a pour avantage de rendre disponible l'information spatiale et spectrale permettant d'identifier un compagnon parmi les tavelures et l'information spectrale permettant la caractérisation de ce compagnon.

L'IDA se base sur le long temps de vie des tavelures quasi-statiques pour bâtir une image de référence à l'aide d'une séquence temporelle. Cette technique consiste à fixer dans le temps le rotateur d'instrument d'un télescope alt-azimutal pour permettre une rotation du champ de vue due à la rotation de la Terre. Ceci permet aussi de conserver l'alignement entre le télescope et la caméra. Dans le cas d'un patron de tavelures statiques, la séquence temporelle résultant de l'observation d'une étoile et de son compagnon est donc composée d'une série d'images ayant la même FÉP comprenant un compagnon se déplaçant en rotation autour de l'étoile hôte d'une image de la séquence à l'autre.

1.5 Le *Gemini Planet Imager*

Le *Gemini Planet Imager* (GPI ; Macintosh et al., 2006) est un instrument de deuxième génération conçu pour les télescopes de 8-m Gemini situés au sommet du Cerro Pachón au Chili (2722 m d'altitude) et du Mauna Kea à Hawaï (4213 m d'altitude) dont la première lumière est prévue pour le début 2011. Son coût s'élèvera au-dessus de 20 millions de dollars américains et son développement est une collaboration internationale entre divers instituts et universités de renom tels que l'American Museum of Natural History (AMNH), l'Institut Herzberg d'astrophysique (IHA), le Jet Propulsion Laboratory (JPL), le Lawrence Livermore National Laboratory (LLNL), l'Université de Californie à Berkeley (UCB), à Los Angeles (UCLA) et à Santa Cruz (UCSC) et l'Université de Montréal.

Au niveau des exoplanètes, GPI aura comme objectifs la détection et la caractérisation de planètes se situant à des orbites > 5 UA dans les systèmes planétaires avoisinant le Soleil. Ses buts principaux seront d'établir la fréquence des systèmes planétaires, de tester les modèles de formation des planètes, d'éclaircir les phénomènes physiques à l'origine des Jupiters chaudes et de découvrir si les systèmes planétaires similaires au système solaire, avec des planètes géantes gazeuses entre 5 et 10 UA, sont rares ou fréquents.

Pour ce faire, GPI sera composé de quatre sous-systèmes. Premièrement, un système d'optique adaptative qualifié d'extrême sera utilisé pour corriger la turbulence atmosphérique et atteindre un rapport de Strehl > 0.9. Pour atteindre une telle performance, ce système aura besoin d'utiliser 45 x 45 actionneurs sur son MD. Une première option est d'utiliser un MD ayant des actionneurs de type piezo-électriques. Ce type de MD nécessite un espacement inter-actionneur de ~ 5 mm. La pupille d'un tel système aurait alors un diamètre de 225 mm qui résulterait en un système dépassant l'enveloppe mécanique disponible au foyer Cassegrain des télescopes Gemini. Une seconde option est d'utiliser un MD basé sur la technologie des microsystèmes électromécaniques (MEMS)

ayant un espacement inter-actionneur typique de l'ordre de 0.5 mm réduisant ainsi significativement la taille de la pupille ; c'est la solution retenue pour GPI. Par contre, cette technologie est moins mature et permet présentement d'obtenir une course maximale de l'ordre de ~ 3 μm (Morzinski et al., 2009) sur le MD. Il doit donc être utilisé en combinaison avec un second MD qui compense les déformations du front d'onde de plus grande amplitude et de plus basse fréquence spatiale. Par analogie avec les systèmes acoustiques, le premier de ces MDs est nommé *woofer* alors que le MEMS compensant les défauts de plus faible amplitude et de plus haute fréquence spatiale est nommé *tweeter*. Un reconstructeur de Fourier sera utilisé afin de minimiser les calculs nécessaires à la détermination des commandes à appliquer aux MDs. L'ASO sera un analyseur de Shack-Hartmann utilisant un filtre spatial pour minimiser les erreurs de repliement spatial qui domineraient sans lui. La fréquence d'échantillonnage sera de 2 kHz pour réduire l'erreur de retard de boucle tout en conservant une magnitude limite raisonnable pour l'étoile guide et ainsi, une couverture du ciel acceptable.

Les trois autres systèmes seront 1) un coronographe de Lyot utilisant une pupille apodisée à son entrée, 2) un interféromètre d'étalonnage qui mesurera les variations d'aberrations non-communes entre le faisceau se rendant au senseur de front d'onde et celui se rendant au plan focal du coronographe et 3) un spectromètre à champ intégral. Ce dernier permettra la réduction du bruit de tavelure et la caractérisation des compagnons détectés à l'aide de l'information spatiale et spectrale recueillie (voir Figure 1.3 pour une représentation schématique des différents sous-systèmes de GPI).

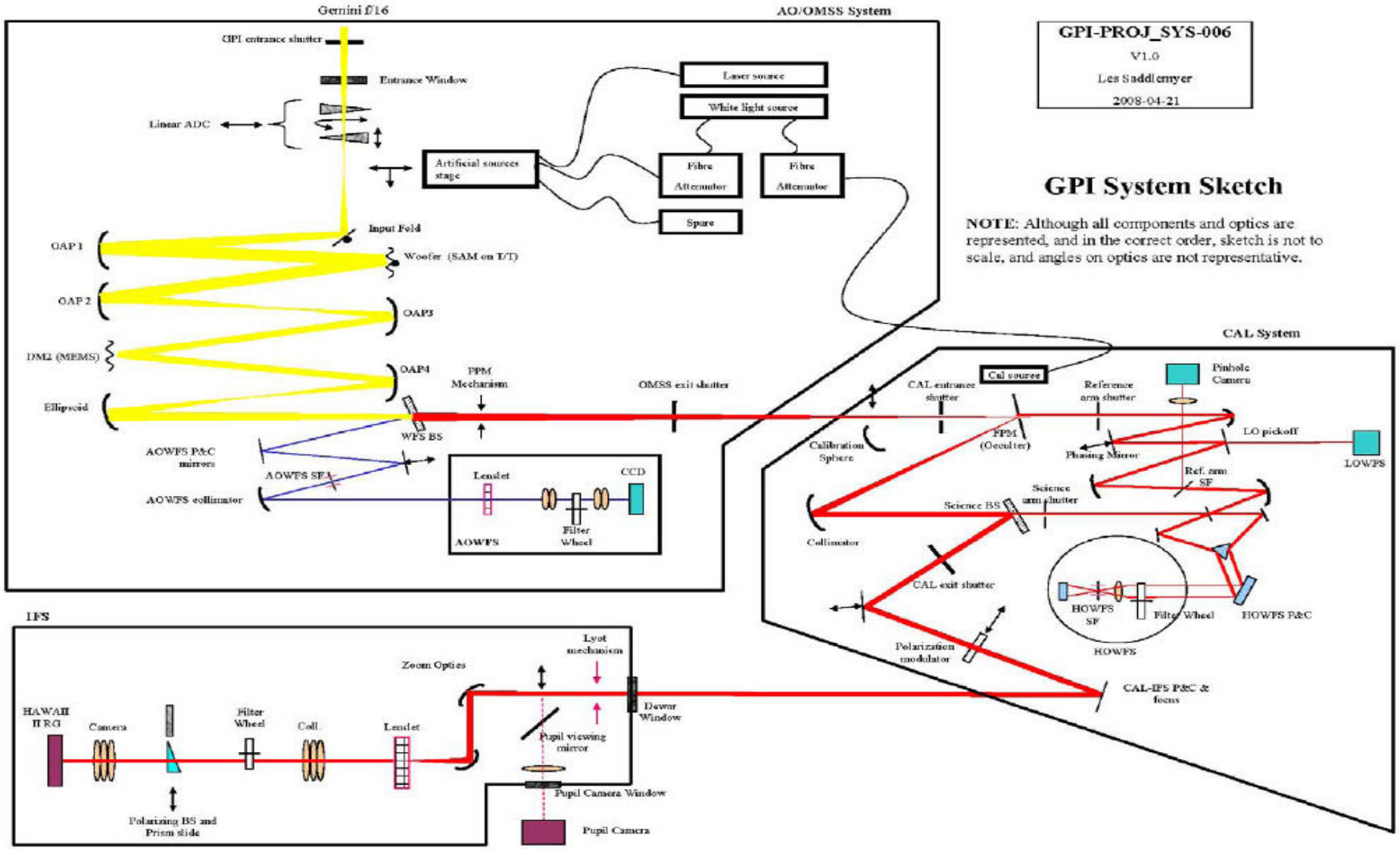

Figure 1.3 Représentation schématique de GPI et de ses sous-systèmes

.

1.6 Sujet de cette thèse

Cette thèse s'inscrit dans le développement de GPI. Au chapitre 2, la spectroscopie intégrale de champ du compagnon de faible masse de l'étoile GQ Lup effectuée à l'aide de la caméra NIFS en fonction sur le télescope Gemini Nord est présentée. Ceci représente un exemple concret de ce qui peut actuellement être accompli en imagerie à haut-contraste à l'aide des spectromètres à champ intégral existants. Les performances de NIFS en atténuation du bruit de tavelure à l'aide de la technique IDA y sont d'abord évaluées. Ensuite, le spectre du compagnon est extrait et une technique minimisant l'impact de l'IDA sur ce spectre est développée. Le spectre est finalement utilisé pour évaluer la température effective et la gravité de surface de GQ Lup b à l'aide de modèles atmosphériques et pour estimer sa masse à l'aide des modèles évolutifs.

NIFS étant un instrument généraliste pouvant être utilisé pour différents domaines de recherche en astrophysique, sa conception n'a pas été optimisée pour l'imagerie à haut-contraste. En fait, aucun SCI présentement en fonction sur les télescopes de 8-10 m de diamètre n'a été conçu spécifiquement pour accomplir cette tâche. Les performances qui pourront être atteintes à l'aide du SCI de GPI sont donc mal connues. Ainsi, un SCI de démonstration optimisé pour l'imagerie à haut-contraste a été développé et testé en laboratoire. Les résultats sont présentés au chapitre 3 avec un nouvel algorithme d'atténuation du bruit de tavelure spécifique à ce type d'instrument.

Le chapitre 4 s'attaque à l'amélioration de la correction du front d'onde à l'aide d'un système d'optique adaptative extrême pour 1) réduire le halo lumineux et, ainsi, l'intensité des tavelures et 2) permettre l'utilisation d'un coronographe. GPI effectuera cette correction à l'aide de ses deux miroirs déformables, le *woofer* et le *tweeter*. La stratégie utilisée pour sélectionner le bon ordre de correction du *woofer* en fonction de l'amplitude maximale pouvant être compensée par le *tweeter*, ainsi qu'un algorithme permettant la séparation optimale de la commande entre les deux miroirs sont présentés. Lors de l'évaluation de la course des actionneurs, une marge de sécurité de 5σ est

choisie, où σ est la déviation standard de l'actionneur nécessitant la plus grande course sur le MD. Cette marge de sécurité permet de rendre statistiquement négligeable la fréquence de saturation des actionneurs et ainsi, de limiter la lumière diffusée liée à ces évènements.

1.7 Déclaration de l'étudiant

J'ai écrit les trois articles présentés et réalisé les travaux leur étant rattachés. Le deuxième article est le résultat d'observations prises à Gemini à l'aide de l'instrument NIFS. René Doyon, David Lafrenière, Christian Marois et Travis Barman m'ont tous grandement aidé à la rédaction de la demande de temps et à la revue de l'analyse des données. J'ai réduit les données, atténué le bruit de tavelure en utilisant un algorithme développé par David Lafrenière, caractérisé l'effet des algorithmes utilisés sur les résultats finaux et conduit l'analyse permettant d'arriver à une estimation de la masse de l'objet observé.

Dans le deuxième article, le travail que j'ai accompli a tout d'abord consisté à concevoir le système optique et mécanique du spectromètre à champ intégral testé, à aligner les composantes optiques dans leur monture, à concevoir le banc de test en laboratoire et à optimiser les performances de la caméra sous la supervision de René Doyon. J'ai ensuite développé l'algorithme de traitement d'images de la caméra avec l'aide de David Lafrenière et René Doyon. Ce dernier m'a aussi fourni de précieuses idées pour le développement de l'algorithme de suppression du bruit de tavelure présenté.

Les travaux présentés dans le dernier article ont été réalisés en étroite collaboration avec Jean-Pierre Véran pour établir la stratégie adoptée. J'ai programmé les simulations Monte Carlo présentées et développé un modèle analytique permettant de vérifier les résultats des simulations. Dans cet article comme dans les deux premiers, les commentaires des co-auteurs ont contribué à solidifier l'argumentation présentée et, ainsi, à en augmenter la qualité.

Bibliographie

Alibert, Y., Mordasini, C., Benz, W., & Winisdoerffer, C., 2005, A&A, 434, 343

Bakos, G. Á., Lázár, Papp, I., Sári, P., & Green, E. M., 2002, PASP, 114, 974

Bally, J., Testi, L., Sargent, A., & Carlstrom, J., 1998, Astrophys. J. , 116, 854

Baraffe, I., Chabrier, G., Allard, F. & Hauschildt, P. H., 2002, A&A, 382, 563

Baraffe, I., Chabrier, G., Barman, T. S., Allard, F. & Hauschildt, P. H., 2003, A&A, 402, 701

Beaulieu, J.-P., et al., 2006, Nature, 439, 437

Biller, B. A., et al., 2007, ApJS, 173, 143

Blum, J. & Wurm, G., 2008, ARA&A, 46, 21

Bond, I. A., et al., 2004, Astrophys. J. , 606, L155

Boss, A. P., 1997, Science, 276, 1836

Boss, A. P., 2001, Astrophys. J. , 563, 367

Boss, A. P., 2006, Astrophys. J. , 643, 501

Briceño, C., Vivas, A. K., Calvet, N., Hartmann, L., Pacheco, R., Herrera, D., Romero, L., Berlind, P., Sánchez, G., Snyder, J. A., & Andrews, P., 2001, Science, 291, 93

Burrows, A., Marley, M., Hubbard, W. B., Lunine, J. L., Guillot, T., Saumon, D., Freedman, R., Sudarsky, D. & Sharp, C., 1997, Astrophys. J. , 491, 856

Burrows, A., Hubbard, W. B., Lunine, J. I., & Liebert, J., 2001, Rev. of Mod. Phys., 73, 2001

Burrows, A., Hubeny, I., Budaj, J., et al., 2008, ApJ, 668, L171

Cameron, A. G. W., 1979, Moon and the Planets, 18, 5

Chabrier, Baraffe, I., G., Allard, F. & Hauschildt, P. H., 2000, Astrophys. J. , 542, 464

Charbonneau, D., Brown, T. M., Noyes, R. W., & Gilliland, R. L., 2002, Astrophys. J. , 568, 377

Charbonneau, D., Knutson, H. A., Barman, T., Allen, L. E., Mayor, M., Megeath, S. T., Queloz, D., & Udry, S., 2008, Astrophys. J. , 686, 1341

Chauvin, G., Lagrange, A.-M., Dumas, C., Zuckerman, B., Mouillet, D., Song, I., Beuzit, J.-L., & Lowrance, P., 2004, A&A, 425, L29

Chauvin, G., Lagrange, A.-M., Dumas, C., Zuckerman, B., Mouillet, D., Song, I., Beuzit, J.-L., & Lowrance, P., 2005a, A&A, 438, L25

Chauvin, G., Lagrange, A.-M., Zuckerman, B., Dumas, C., Mouillet, D., Song, I., Beuzit, J.-L., Lowrance, P. & Bessell, M. S., 2005b, A&A, 438, L29

Dessenne, C., Madec, P.-Y., & Rousset, G., 1998, Appl. Opt., 37, 4623

Deming, D., 2008, Proc. IAU Symp., 253

Dupuy, T. J., Liu, M. L., & Ireland, M. J., 2009, accepted for publication in Astrophys. J.

Durisen, R. H., Boss, A. P., Mayer, L., Nelson, A. F., Quinn, T., & Rice, W. K. M. 2007, Protostars and Planets V, 607

Ellerbroek, B. L., & Rhoadarmer, T. A., 1997, JOSA A, 14, 1975

Ellerbroek, B. L., & Rhoadarmer, T. A., 2001, Math. Comput. Model., 2001, 33, 145

Freischlad, K., & Koliopoulos, C. L., 1985, Proc. SPIE, 551, 74

Fried, D. L., 1978, JOSA, 68, 1651

Gaudi, B. S., et al., 2008, Science, 319, 927

Gendron, E., & Léna, P., 1994a, A&A, 291, 337

Gendron, E., & Léna, P., 1994b, A&A, 111, 153

Guyon, O., 2003, A&A, 404, 379

Haisch, K. E., Lada, E. A., & Lada, C. J., 2001, Astrophys. J. , 553, L153

Herriot, G. Morris, S., Roberts, S., Fletcher J. M., Saddlemyer, L. K., Singh, G., Véran, J.-P., & Richardson, E. H., 1998, Proc. SPIE, 3353, 488

Inaba, S., Wetherill, G. W., & Ikoma, M., 2003, Icarus, 166, 46

Jones, H.R.A., 2004, The Search for Other Worlds : Fourteenth Astrophysics Conference, AIP conference, 713, 17

Kalas, P., Graham, J. R., Chiang, E., Fitzgerald, M. P., Clampin, M., Kite, E. S., Stapelfeldt, K., Marois, C., & Krist, J., 2008, Science, 322, 5906, 1345.

Kasdin, N. J., Vanderbei, R. J., Spergel, D. N., & Littman, M. G., 2003, Astrophys. J. , 582, 1147

Knutson, H. A., Charbonneau, D., Allen, L. E., et al., 2008, Astrophys. J. , 673, 526

Lafrenière, D. et al., 2007a, Astrophys. J. , 670, 1367

Lafrenière, D., Marois, C., Doyon, R., Nadeau, D., & Artigau, É., 2007b, Astrophys. J. , 660, 770

Lafrenière, D., Jayawardhana, R., & van Kerkwijk, M. H., 2008, ApJ, 689, L153

Lagrange, A.-M., Gratadour, D., Chauvin, G., Fusco, T., Ehrenreich, D., Mouillet, D., Rousset, G., Rouan, D., Allard, F., Gendron, É., Charton, J., Mugnier, L., Rabou, P., Montri, J., & Lacombe, F., 2009, AA, 493, 21L.

Laughlin, G., Bodenheimer, P., & Adams, F. C., 2004, Astrophys. J. , 612, L73

Lissauer, J. J., 2001, Nature, 409, 23L

Lissauer, J. J., 2006, The Spitzer Space Telescope : New Views on the Cosmos, ASP Conference Series, 257

Lyot, M. B., 1939, MNRAS, 99, 580

Macintosh, B., et al., 2006, Proc. SPIE, 6272, 62720L

Marcy, G. W., & Butler, R. P., 1998, ARA&A, 36, 57

Marcy, G., Butler, R. P., Fischer, D., Vogt, S., Wright, J. T., Tinney, C. G., & Jones, H. R. A. 2005, Prog. Theor. Phys. Suppl., 158, 24.

Marley, M. S., Fortney, J. J., Hubickyj, O., Bodenheimer, P., & Lissauer, J. J., 2007, Astrophys. J. , 655, 541

Marois, C., Doyon, R., Nadeau, D., Racine, R., Riopel, M., Vallée, P., & Lafrenière, D. 2005, PASP, 117, 745

Marois, C., Lafrenière, D., Doyon, R., Macintosh, B., & Nadeau, D. 2006, Astrophys. J. , 641, 556

Marois, C., Macintosh, B., & Barman, T., 2007, Astrophys. J. , 654, L151

Marois, C., Lafrenière, D., Macintosh, B. & Doyon, R., 2008, Astrophys. J. , 673, 647

Mayer, L., Quinn, T., Wadsley, J. & Stadel, J., 2002, Science, 298, 1756

Mayor, M. & Queloz,D., 1995, Nature, 378, 355

Mayor, M., Pepe, F., Queloz, D., Bouchy, F., Rupprecht, G., et al., (2003), The Messenger, 114, 20

McCullough, P. R., Stys, J. E., Valenti, Fleming, S. W., J. A., Janes, K. A., & Heasley, J. N., 2005, PASP, 117, 783

McElwain, M. W., Metchev, S. A., Larkin, J. E., Barczys, M., Iserlohe, C., Krabbe, A., Quirrenbach, A., Weiss, J., & Wright, S. A., 2007, Astrophys. J. , 656, 505

Mizuno, H., 1980, Prog. Theor. Phys., 64, 544

Mohanty, S., Jayawardhana, R., Huélamo, N., & Mamajek, E., 2007, Astrophys. J. , 657, 1064

Morzinski, K., Macintosh, B., Gavel, D., & Dillon, D., 2009, Opt. Express , 17, 7, 5829

Neuhäuser, R., Guenther, E. W., Wuchterl, G., Mugrauer, M., Bedalov, A., & Hauschildt, P. H., 2005, A&A, 435, L13

Nielsen, E. L., Close, L. M., Biller, B. A., Masciadri, E., & Lenzen, R., 2008, Astrophys. J. , 674, 466

Noll, R. J., 1976, JOSA, 66, 3

Perri, F., & Cameron, A. G. W., 1974, Icarus, 22, 416

Pollacco, D. L. et al., 2006, PASP, 118, 1407

Poyneer, L. A., Gavel, D. T., & Brase, J. M., 2002, JOSA A, 19, 2100

Racine, R., Walker, G. A. H., Nadeau, D., Doyon, R., & Marois, C. 1999, PASP, 111, 587

Rigaut, F., Salmon, D., Arsenault, R., et al., 1998, PASP, 110, 152

Roddier, F., Prog. Optics, 1981, 19, 281.

Seifahrt, A., Neuhäuser, R. & Hauschildt, P.H., 2007, A&A, 463, 309

Sivaramakrishnan, A., Koresko, C. D., Makidon, R. B., Berkefeld, T., & Kuchner, M. J., 2001, Astrophys. J. , 552, 397

Soummer, R., 2005, ApJ, 618, L161

Sozzetti, A., 2004, MNRAS, 354, 1194

Sparks, W. B., & Ford, H. C., 2002, Astrophys. J. , 578, 543

Stassun, K. G., Mathieu, R. D., & Valenti, J.A., 2006, Nature, 440, 311

Stassun, K. G., Mathieu, R. D., & Valenti, J.A., 2007, Astrophys. J. , 664, 1154

Udry, S., Mayor, M., Naef, D., Pepe, F., Queloz, D., et al., 2000, A&A, 356, 590

Udry, S., & Santos, N. C., 2007, ARA&A, 45, 397

CHAPITRE 2

OBSERVATIONS DANS LE PROCHE INFRAROUGE DE GQ LUP B EN UTILISANT LE SPECTROGRAPHE À CHAMP INTÉGRAL DE GEMINI NIFS

NEAR INFRARED OBSERVATIONS OF GQ LUP B USING THE GEMINI INTEGRAL FIELD SPECTROGRAPH NIFS[a]

JEAN-FRANÇOIS LAVIGNE[bcd], RENÉ DOYON[b], DAVID LAFRENIÈRE[e], CHRISTIAN MAROIS[f] AND TRAVIS BARMAN[g]

Published in: *the Astrophysical Journal*, V.704, p.1098 (2009)

Abstract

We present new JHK spectroscopy ($R \sim 5000$) of GQ Lup b, acquired with the near-infrared integral field spectrograph NIFS and the adaptive optics system ALTAIR at the Gemini North telescope. Angular differential imaging was used in the J and H bands to suppress the speckle noise from GQ Lup A; we show that this approach can provide improvements in signal-to-noise ratio (S/N) by a factor of $2-6$ for companions located at subarcsecond separations. Based on high-quality observations and GAIA synthetic spectra, we estimate the companion effective temperature to $T_{\rm eff} = 2400 \pm 100$ K, its gravity to $\log g = 4.0 \pm 0.5$, and its luminosity to $\log(L/L_{\odot}) = -2.47 \pm 0.28$. Comparisons with the predictions of the DUSTY evolutionary tracks allow us to constrain the

[a]Reproduced by permission of the AAS

[b]Département de physique, Université de Montréal, C.P. 6128, succ. Centre-Ville, Montréal, QC, Canada

[c]Herzberg Institute of Astrophysics, 5071 West Saanich Road, Victoria, BC, Canada

[d]Institut national d'optique, Parc technologique du Québec métropolitain, 2740 rue Einstein, Québec, QC, Canada

[e]Department of Astronomy and Astrophysics, University of Toronto, 50 St. George Street, Toronto, ON, M5S 3H4, Canada

[f]NRC Herzberg Institute of Astrophysics, 5071 West Saanich Rd, Victoria, BC, V9E 2E7, Canada

[g]Lowell Observatory, 1400 West Mars Hill Road, Flagstaff, AZ 86001, USA

mass of GQ Lup b to $8-60\ M_{\rm Jup}$, most likely in the brown dwarf regime. Compared with the spectra published by Seifahrt and collaborators, our spectra of GQ Lup b are significantly redder (by $15-50\%$) and do not show important $Pa\beta$ emission. Our spectra are in excellent agreement with the lower S/N spectra previously published by McElwain and collaborators.

2.1 Introduction

An important goal of exoplanet imaging is understanding how planetary systems form and this requires observing planets when they are very young, i.e. at ages less than a few million years. Ten years after the first discovery of an extra-solar giant planet (EGP), the imaging era of exoplanet science has finally started. The year 2008 has been particularly prolific in that matter with the discovery of the first planetary system around the ~ 60 Myr old HR 8799 (Marois et al., 2008), of the exoplanet candidates in orbit around the $100-300$ Myr old Fomalhaut (Kalas et al., 2008), in orbit around the ~ 12 Myr old β Pictoris (Lagrange et al., 2008), the potential companion to the ~ 5 Myr old 1RXS J160929-210524 (Lafrenière et al., 2008) and the planetary mass object (PMO) candidate evolving round the 0.9 to 3 Myr old T-Tauri star CT CHA (Schmidt et al., 2008). These new discoveries add to a few previous detections of planet candidates such as the PMO in orbit around the young (~ 10 Myrs) 25 $M_{\rm Jup}$ brown dwarf (BD) 2M1207 (Chauvin et al., 2004) and the companion in orbit around the $\sim 1-10$ Myr old T Tauri star GQ Lup (Neuhäuser et al., 2005).

GQ Lup b is particularly interesting; the co-moving companion is relatively bright (K=13) and lies at 0.7 arcsec (100 ± 50 AU) from the 7th magnitude K7eV primary. Despite several studies, the mass of GQ Lup b is still poorly constrained. Neuhäuser et al. (2005) identified prominent CO and H_2O bands typical of cool M9$-$L4 dwarfs but could not constrain accurately the mass of the companion ($1-42\ M_{\rm Jup}$) because the effective temperature ($T_{\rm eff}$; $1600-2500$ K), the gravity and the distance of the object were not well

Table 2.1. GQ Lup b previously published results

	Neuhäuser et al. (2005)	Marois et al. (2007)	McElwain et al. (2007)	Seifahrt et al. (2007)	This work
Age (Myr):	1 ± 1	1 ± 1	$1 - 10$	1 ± 1	$1 - 10$
Distance (pc):	140 ± 50	140 ± 50	150 ± 20	140 ± 50	139 ± 45
$T_{\rm eff}$ (K):	2050 ± 450	2335 ± 100	2600 ± 300	2650 ± 100	2400 ± 100
log g:	2.52 ± 0.77	3 (assumed)	-	3.7 ± 0.5	4.0 ± 0.5
Spectral type:	M9 - L4	-	M6 - L0	-	L1$\pm$1
Radius ($R_{\rm Jup}$):	~ 2	3.7 ± 0.5	-	$3.50^{+1.50}_{-1.03}$	-
$\log(L/L_{\odot})$:	-2.37 ± 0.41	-2.42 ± 0.07	-2.46 ± 0.14	-2.25 ± 0.24	-2.47 ± 0.28
Mass ($M_{\rm Jup}$):	$1 - 42$	$10 - 20$	$10 - 40$	$4 - 36$	$8 - 60$

determined. Marois et al. (2007) have analyzed archived HST WFPC2 and NICMOS data and Subaru CH_4, H, K_s and L' band images of GQ Lup b and provided estimates of its bolometric luminosity ($\log(L/L_{\odot}) = -2.42 \pm 0.07$ at 140 pc), its radius (0.38 ± 0.05 $R_{\odot}$) and its effective temperature (2335 ± 100 K). Assuming a $\log\ g = 3$ and based on the evolutionary models of Baraffe et al. (2003), they inferred a mass ranging from 10 to 20 $M_{\rm Jup}$. McElwain et al. (2007) secured J- and H-band spectra and found the companion to be somewhat hotter than previously reported with a spectral type between M6 and L0 corresponding to effective temperatures between 2400 and 2900 K assuming the effective temperature - spectral type relationship from Golimowski et al. (2004). Using the evolutionary models from Burrows et al. (1997) and Chabrier et al. (2000) and their derived bolometric luminosity of $\log(L/L_{\odot}) = -2.46 \pm 0.14$ they inferred a mass of $10 - 40$ $M_{\rm Jup}$. A mass estimate has also been reported by Seifahrt et al. (2007) who acquired J-, H- and K-band spectra and compared them to the predictions of the GAIA model from Brott & Hauschildt (2005). The best fit resulted in $T_{\rm eff} = 2550 - 2750$ K and $\log\ g = 3.7 \pm 0.5$ dex. From these values, their estimated $\log(L/L_{\odot}) = -2.25 \pm 0.24$ and by comparison with 2M0535 (Stassun et al., 2006) which has a dynamically determined mass of 36 ± 3 $M_{\rm Jup}$ and a similar age as GQ Lup, they derived a mass between 4 and 36 $M_{\rm Jup}$. A summary of previously reported physical parameters of GQ Lup b is given in Table 2.1.

In light of the International Astronomical Union (IAU) working definition which

states that a planet must have a mass below the deuterium burning limit of $\sim 13\ M_{\rm Jup}$, the nature of GQ Lup b thus remains uncertain. Further progress will be made through a better distance estimation of the system and better spectroscopic characterization of the companion.

In this paper, we present new $R \sim 5000$ JHK spectroscopic observations of the GQ Lup system taken with the integral field spectrograph NIFS in combination with the adaptive optics system ALTAIR at the Gemini North telescope using angular differential imaging (ADI) to improve the signal-to-noise ratio (S/N) of the companion. The resulting spectrum is analyzed and compared with synthetic atmospheric spectra and evolutionary tracks to infer the physical parameters of the companion.

2.2 Observations

The GQ Lup system was observed in the J-, H- and K-band respectively on the nights of 2007 May 30, June 1 and June 27 at the Gemini North Telescope (program GN-2007A-Q-46) using NIFS combined with the ALTAIR adaptive optics system (Herriot et al., 1998). NIFS is a near-infrared integral field spectrograph (IFS) based on the image slicer concept (McGregor et al., 2002). It has a spectral resolving power of 5000 in each band, a total field of view of $3.0'' \times 3.0''$ and rectangular spatial resolution elements of $0.04'' \times 0.1''$.

All observations were obtained with the Cassegrain rotator turned off to allow rotation of the field around the host star. The J- and H-band sequences consisted of 18×400s and 27×300s exposures, respectively, without any dithering. This allowed enough field rotation to use angular differential imaging (ADI; Marois et al., 2006; Lafrenière et al., 2007) to suppress the speckle noise. As the PSF is better sampled and AO achieves better performance in the K band, observations were obtained with a 9-position square dithering pattern with each position offsetted by $0.4''$; in total 72 exposures of 50s were obtained. The median seeing was measured to be $0.44''$, $0.61''$ and $0.67''$ in J, H and

Table 2.2. Observation log

Band	Date	Number of exposures	Exposure time (s)	Median seeing ($''$)	Median airmass	Total field rotation ($^\circ$)	Dither ($''$)
J-band:	2007 May 30	18	400	0.44	1.79	34.3	No
H-band:	2007 Jun 1	27	300	0.61	1.79	38.8	No
K-band:	2007 Jun 27	72	50	0.67	1.83	33.1	$\pm$0.7

K respectively and the observations were conducted under a median air mass of 1.79 in both J and H and of 1.83 in K. A spectroscopic standard for telluric correction was observed at five random dither positions having a maximal excursion of $\pm 0.7''$ after the J-band sequence and both before and after the H- and K-band observations. The spectroscopic standards for telluric correction were HIP 82714 in J and HIP 69021 in both H and K. Sky and arc lamp frames were taken at the end of each sequence. Darks and flats as well as Ronchi flats allowing the calibration of the spatial distortion of the camera were taken during daytime calibration. No astrometric calibration data (plate scale and orientation) were obtained. An observation log is shown in Table 2.2.

2.3 Data Reduction

2.3.1 Primary data reduction and data cube reconstruction

The data cube reconstruction was done with the IRAF Gemini data reduction package version 1.9.1a. The calibration data were first processed to construct a flat field, a bad pixel map, a wavelength solution and a map of the curved spectral traces.

The telluric data cubes were then reconstructed. The images were rectified to correct for the trace curvature and re-sampled to yield a common constant wavelength step for all spatial elements. A sky cube was built from the median of the dithered spectroscopic standard data and subtracted from each telluric cube. The latter were then corrected for atmospheric dispersion by fitting a Gaussian kernel to the PSF to find its center in each spectral slice and by translating the PSFs to the center of the field-of-view. The median

telluric spectrum was computed and divided by the spectrum of a blackbody at 10 000 K, the approximate A0V spectroscopic standard temperature.

The final step consisted in reducing the science data and building their associated data cubes. The sky frame obtained after the science observations was first subtracted from each image of the time-lapsed sequence. The science data cubes were extracted following the same procedure used for the telluric data. Telluric correction was then applied. Atmospheric dispersion was then corrected as before. Interstellar extinction was considered to be negligible as most of the extinction associated with GQ Lup A is believed to be circumstellar (McElwain et al., 2007). The rectangular IFS spatial resolution elements were interpolated to yield a spaxel size of $0.043'' \times 0.043''$ in the final reconstructed cube. The term spaxel will be used to refer to a single (x, y, λ) element in the final data cube. This is applied to all IFS images to get a final dataset composed of time-lapsed data cubes.

An example of a collapsed data cube, i.e. integrated over the full wavelength range of the photometric band, obtained for each observed band is shown in the top panels of Figure 2.1. A bright vertical stripe aligned with NIFS slitlets is present in all our data. NIFS is known to have some scattered light in each independent channel which can result in an enhanced sky proportional to the star brightness in each slitlet and could explain such a bright stripe.

In preparation for the extraction of the signal of GQ Lup b, the bright signal from the primary PSF was subtracted to first order by applying an unsharp mask with a Gaussian kernel of six pixels FWHM, followed by the subtraction of a median radial intensity profile about the center of the PSF. The images were then convolved by a 1 pixel FWHM Gaussian kernel to attenuate the pixel-to-pixel noise resulting from the interpolation of the rectangular IFS spatial resolution elements to the square data cube spaxels. The resulting residual broadband images obtained after collapsing the data cubes are shown in the lower panels of Figure 2.1. Note that the residual vertical stripe is subtracted by the ADI speckle suppression algorithm (see next section) and does not impact the final

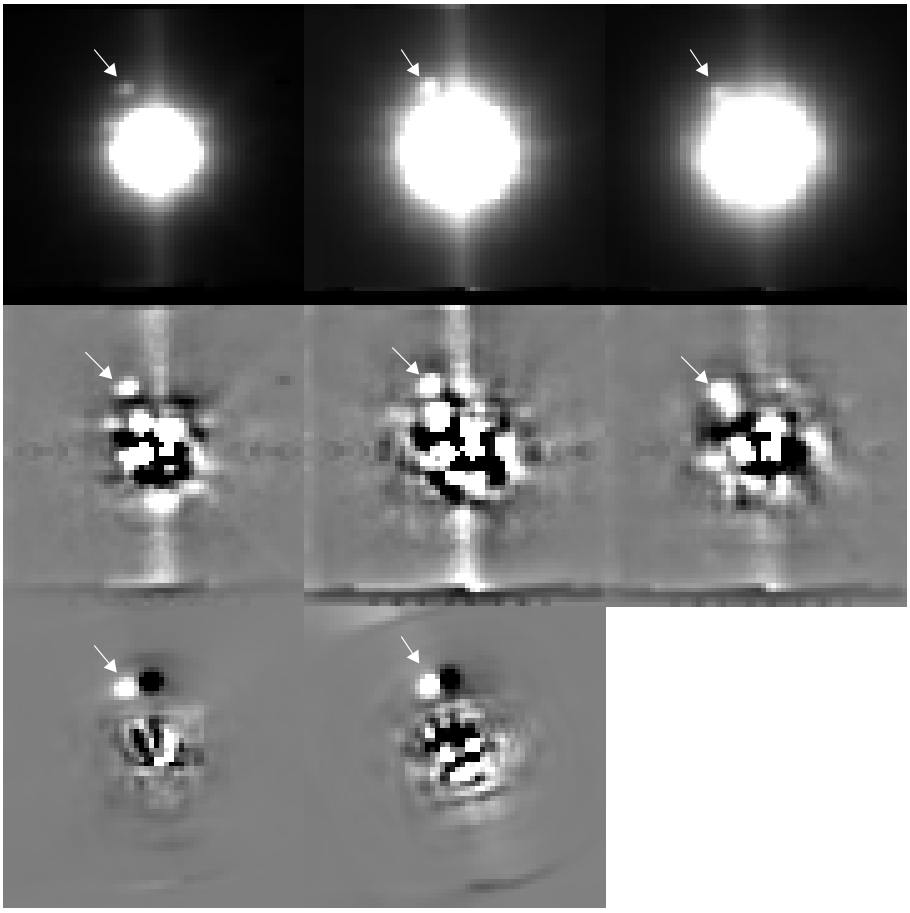

Figure 2.1 Detection of the companion to GQ Lup in J, H and K from left to right. Each image has a field of view of $3.0'' \times 3.0''$. The top, center and bottom panels respectively show examples of collapsed data cubes before and after the subtraction of a radial profile and after the application of the ADI algorithm. Arrows indicate the companion position. Each image was divided by the host star flux integrated in a two pixels diameter circular aperture and the same dynamic range is used to display all bands. Images after the subtraction of the radial profile and after the application of the ADI algorithm are also shown on the same dynamic range.

J and H spectra. In the K band, however, no such algorithm is used. We therefore only considered the first 45 data cubes obtained, in which the companion does not overlap with the vertical stripe. The K-band spectrum was extracted from these residual images by summing the flux in a 2 spaxel diameter circular aperture.

2.3.2 Angular Differential Imaging

As can be seen in Figure 2.1, the residual speckle noise is significant at the separation of the companion and this severely limits the accuracy by which the spectrum can be extracted. In principle, this speckle noise could be attenuated using spectral deconvolution techniques (Sparks & Ford, 2002; McElwain et al., 2007; Thatte et al., 2007; Janson et al., 2008; Lavigne et al., 2009, in preparation) but, in practice, the companion radial displacement is only $2-3$ NIFS spaxels in a data cube rescaled such that the speckles at different wavelengths overlap. This, combined with the companion brightness, makes an accurate fit of the speckle pattern contaminating the companion spectrum very hard to obtain.

The approach chosen instead was to use the ADI technique developed by Marois et al. (2006). This technique consists in acquiring a series of images with the Cassegrain rotator of an alt-az telescope turned off. This allows field rotation between each observation of the sequence. The companion is then rotating around its host star in the time-lapsed sequence while the quasi-static speckles, introduced by the defects of the telescope optical elements, stay fixed. For each data cube of the time series, a reference data cube can be built from the other data cubes, and used to subtract the speckle pattern and attenuate the speckle noise.

Examples of images obtained after the subtraction of their median radial profile taken at intervals of 65 minutes in the *H* band are shown in Figure 2.2. This corresponds to an image at the beginning, the middle and the end of the whole sequence. The long speckle life time is clearly seen in that sequence while the companion revolves around its host star due to field rotation.

The reference data cube was built using the "locally optimized combination of images" (LOCI) algorithm developed by Lafrenière et al. (2007). This algorithm builds a reference PSF having the highest speckle correlation with respect to the analyzed frame from the dataset composed of the time sequence of images. This is done by first dividing

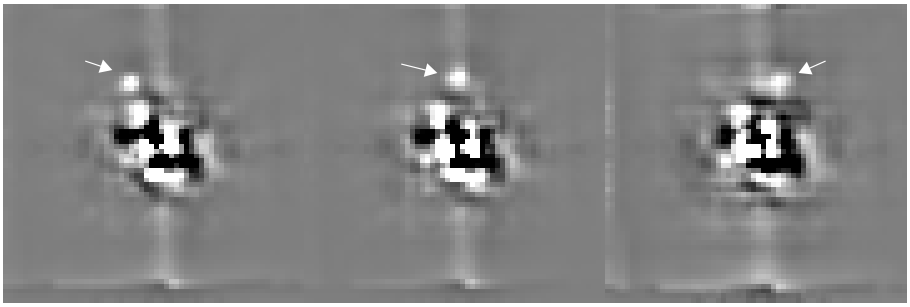

Figure 2.2 *H*-band time sequence of images with the Cass-rotator turned off. Images are separated by 65 minutes each. The speckles long life time is clearly seen from this sequence. Arrows indicate the companion position. The field has rotated by 21.0° in the second image and by 37.7° in the third.

the frame in optimization subsections. The reference PSF is then built for each zone by computing the linear combination of images that guarantees the lowest possible residual noise after subtraction. Only the images of the time sequence in which the companion had a sufficient displacement compared to the analyzed frame are used to build the reference PSF to avoid a significant companion flux loss. The resulting minimal time separation between two frames is the one yielding the best companion S/N when two frames are differentiated. This was found to be 2400s in the *J* and 2700s in the *H* band which respectively corresponds to 6 and 9 images in the time sequence and to a minimal companion displacement of 2.7 and 2.9 pixels.

Since the companion position is already known, a single horseshoe shaped optimization zone centered on the host star and having a mean radius corresponding to that of the companion was used. The radial width is taken to be 4 pixels. The missing azimuthal zone is the one in which the companion is moving through the time sequence. This algorithm is applied to each spectral slice of each data cube. The resulting data cubes are then rotated to align the field of view and summed to build the final ADI data cube. The companion spectrum was extracted from this final cube by summing the flux in a 2 spaxel diameter circular aperture.

Applying this ADI process to each data cube has the advantage of increasing the S/N

of the companion spectrum by significantly attenuating the speckle noise. However, a fraction of the companion signal is lost through the application of the LOCI algorithm (Lafrenière et al., 2007). Moreover, the fact that each spectral slice is treated independently from the others can have an impact on the resulting spectral shape. Hence, we have developed an algorithm to determine the influence of ADI on the companion spectrum.

For simplicity, let us consider only a single slice of a given data cube in the sequence, keeping in mind that the procedure described below is repeated for each slice and each cube. Following the execution of the above LOCI subtraction algorithm, the residual integrated flux at the companion position in the cube considered can be written as

$$F = I - \sum_i c_i I_i, \tag{2.1}$$

where I is the integrated flux in the slice considered before LOCI subtraction, I_i is the same but for cube i, and $\{c_i\}$ is the set of coefficients found by the LOCI algorithm. The integrated flux I can be expressed as the sum of a signal C coming from the companion and a signal S coming from quasi-static speckles, yielding

$$F = (S+C) - \sum_i c_i (S_i + C_i) = S_{\text{res}} + C - \sum_i c_i C_i, \tag{2.2}$$

where $S_{\text{res}} = S - \sum_i c_i S_i$ is the residual speckle signal, which on average will be close to zero. Our goal is to find the true companion signal C, and so we must estimate the quantity $\sum_i c_i C_i$, i.e. the fraction of the companion signal that was subtracted by the algorithm. This was done by introducing a fake companion of known flux and flat spectrum into the images, at the same separation as GQ Lup b but 180° from it. The fake companion was taken to be a shifted and intensity scaled-down version of the primary star; its PSF should thus be very similar to that of GQ Lup b. The LOCI algorithm was applied to the sequence of data with the fake companion by using the exact same coefficients as for the data without the fake companion. Then the fake companion residual flux F'

was retrieved. Since the true fake companion signal C' and the residual speckle signal $S'_{\rm res}$ at the location of the fake companion are known (the latter from the execution of the algorithm without the fake companion), the fraction of the fake companion flux that was subtracted by the algorithm in a given spectral slice can be readily computed as

$$f_\lambda \equiv \frac{\sum_i c_i C'_i}{C'} = \frac{S'_{\rm res} + C' - F'}{C'}. \tag{2.3}$$

This fraction should be the same for GQ Lup b as for the fake companion since the same coefficients were used for both and they have the same PSF. Note also that f_λ is independent of the fake companion azimuthal position as $\sum_i c_i C'_i$ only depends on the relative angular position of the companion PSF between the analyzed frame and the cube i. So, the true signal of GQ Lup b can be calculated as

$$C = \frac{F - S_{\rm res}}{1 - f_\lambda}, \tag{2.4}$$

where in practice $S_{\rm res}$ is neglected; the resulting error on C is computed by measuring the residual speckle noise at the companion radius. The correction factors f_λ computed for the J and H ADI spectra by the above procedure are shown in Figure 2.3.

Finally, to make sure that the above procedure did not introduce any artificial feature in the spectra, mainly in their continuum shape, we have performed a simple spectrum extraction directly from the reduced data cubes without any ADI processing. The resulting spectra were compared with the spectra obtained with ADI processing and no significant difference was found, save for a lower S/N. More precisely, a similar procedure as for the K-band data was used to extract a non-ADI spectrum from the data cubes in which the companion is the least affected by the vertical stripe in the J and H bands. The resulting ADI spectrum was then divided by the non-ADI one to characterize the continuum dispersion. The median non-ADI J-band spectrum of the first six data cubes had only a 5% continuum difference with the ADI spectrum. Similarly, the first eight and last four data cubes in the H band were used to compute the median non-ADI spectrum

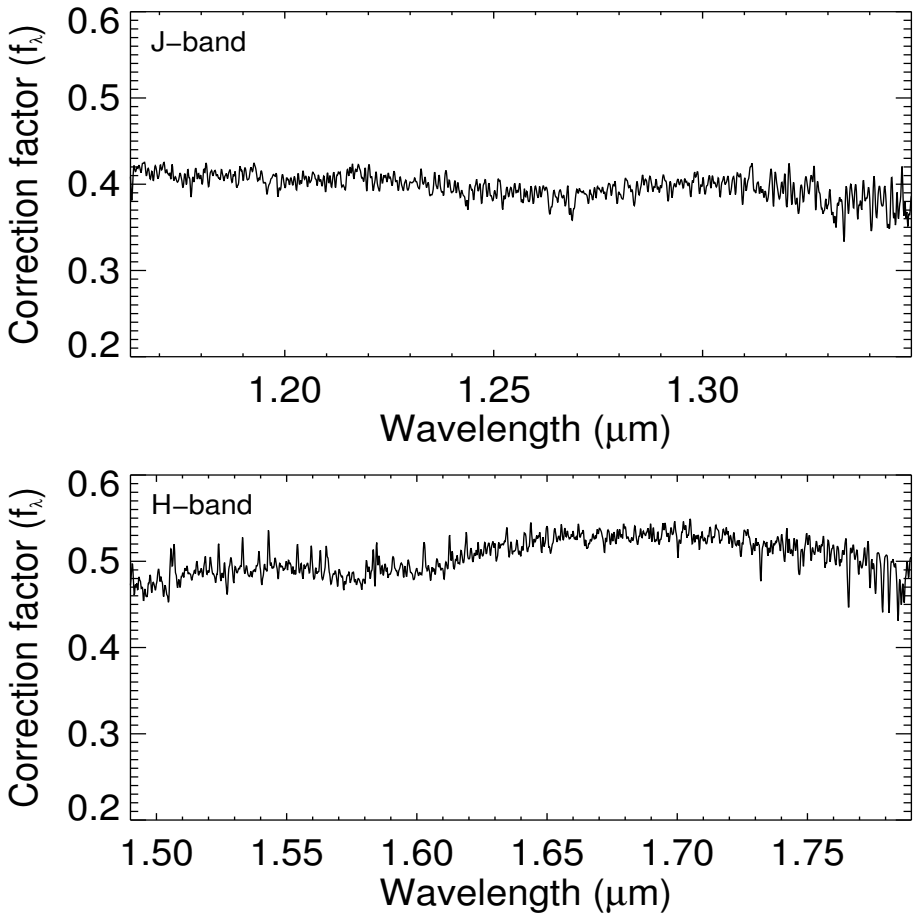

Figure 2.3 Correction factors applied to the extracted J- and H-band spectra at a spectral resolution of $R \approx 5000$ to compensate for the flux loss during spatial filtering and the ADI process. The fake companions used to compute this factor had a flat spectrum (see section 2.3.2 for more details).

and the resulting continuum had only a 6% slope difference with the ADI spectrum.

2.4 Results

2.4.1 Speckle noise attenuation performance

The ability of the algorithms described in the previous section to attenuate the speckle noise in NIFS data is evaluated in this section. The speckle noise attenuation factor is defined as the ratio of the noise in the initial image over the noise in an ADI image. The

noise in ADI images was corrected for the companion flux loss during the ADI process using fake companion implants. Each spectral slice was evaluated independently. We report the median value of speckle noise attenuation in all the spectral slices as a function of angular separation from GQ Lup. The noise was evaluated by computing the standard deviation of spaxels within an annulus of one spaxel width at each radius. GQ Lup b was masked out from the images.

The results are plotted at the top of Figure 2.4 for the J and H bands while the contrast curves achieved are plotted at the bottom of the figure. For a single data cube, the ADI subtraction provided a noise attenuation by a factor of 1.5 to 2 in both J and H, while the combination of all ADI data cubes after alignment of their field of view provided an additional noise attenuation by a factor of 2 to 3. Overall, the speckle noise is attenuated by a factor of $3-6$ in J and a factor $2-5$ in H.

2.4.2 Photometry

The relative photometry of the companion compared with its host star is first evaluated. Unfortunately, the peak of GQ Lup A is saturated or in the detector non-linear regime over most of the J band and the entire H band, preventing us from calculating differential photometry over those bands. In J, over the narrow spectral range in which GQ Lup A is in the detector linear regime ($1.31-1.35$ μm), we calculated a contrast of 6.53 ± 0.06 mag for the companion.

The uncertainty was measured by computing the standard deviation of the flux in 20 apertures identical to the one used to integrate the companion flux at the same radius as the companion. The peak of GQ Lup A is below non-linearity in the entire K band; we measured a differential photometry of $\Delta K_s = 6.35 \pm 0.11$ mag.

GQ Lup A is a known variable classical T Tauri star (e.g. Batalha et al., 2001). Broeg et al. (2007) reported it to vary by ± 0.44 mag and ± 0.22 mag in J- and K_s-band respectively over a period of 8.38 ± 0.2 days while Neuhäuser et al. (2008) found it to vary by a maximal amplitude of ± 0.20 mag in the K_s band between May 2005

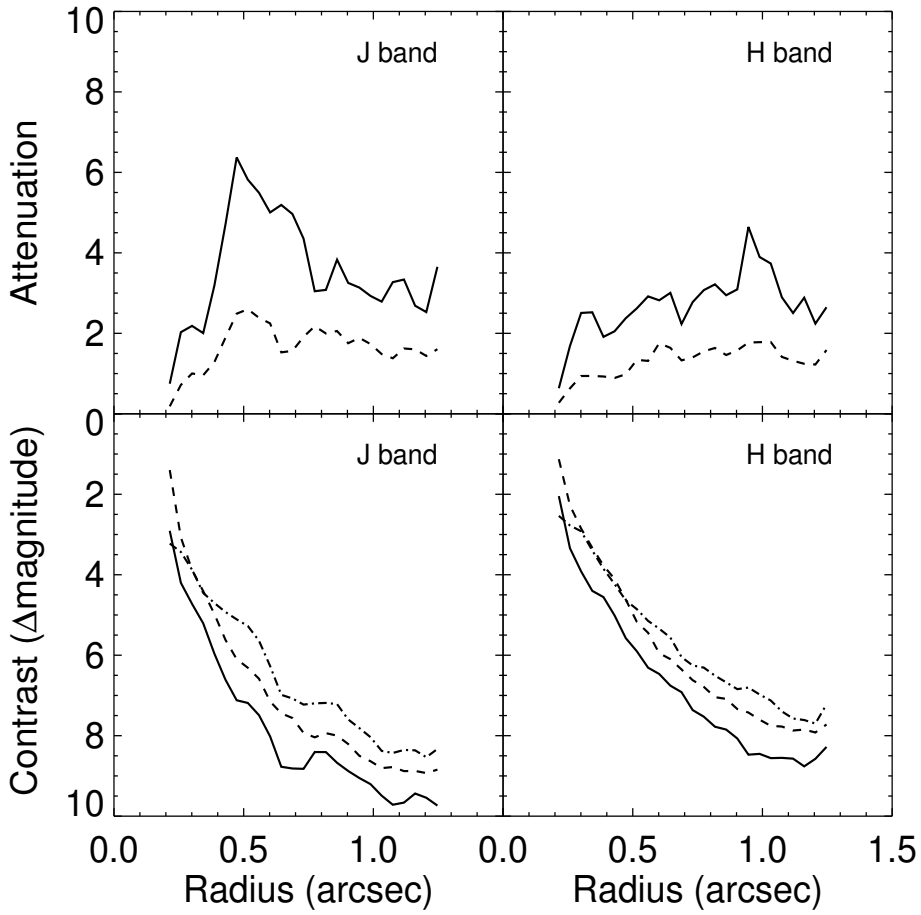

Figure 2.4 The speckle noise attenuation performance is plotted in the upper panels for collapsed data cubes in J- and H-band. The dashed line represents the improvement between a single image of the time sequence and its associated ADI image. The solid line is the attenuation obtained between a single image and the final ADI image constructed by aligning the field of view and adding all the single ADI images. The bottom panels show the median detection limit in the non-ADI images (dot-dashed line), the median detection limit in single ADI images (dashed line) and after field of view alignment and addition of all the single ADI images (solid line). The contrast or detection limit is defined as the 5σ speckle noise level in an image. The ADI curves were corrected for the companion flux loss resulting from the reference image subtraction. Note that the reference image was constructed with a singular LOCI optimization zone situated at the companion radius and, hence, the reported curves are the lowest achievable performance with NIFS at other radii.

and Feb 2007. Using the GQ Lup A photometry reported by Neuhäuser et al. (2008) of $K_s = 7.18 \pm 0.20$ mag and the J-band photometry from 2MASS $J = 8.605 \pm 0.44$ with the updated error bar from Broeg et al. (2007), we find a GQ Lup b photometry of $K_s = 13.45 \pm 0.25$ and $J = 15.13 \pm 0.44$. The K_s value is consistent with $K_s = 13.39 \pm 0.08$ from Neuhäuser et al. (2008) and the J-band value is consistent with 14.90 ± 0.11 reported by McElwain et al. (2007).

2.4.3 Spectroscopy

Our spectra of GQ Lup b are shown in Figure 2.5. The S/N are 145, 76 and 15 at $R \approx 5000$ in JHK respectively where the noise was computed from the dispersion of the flux measured in 20 apertures situated at the same radius as the companion. The integrated flux in each aperture were corrected by f_λ (see section 2.3.2).

In the same figure, our JHK spectrum of GQ Lup b is compared with the previously published results obtained by Seifahrt et al. (2007) and McElwain et al. (2007)[1]. The first noted feature is that our spectra are redder than the ones reported by Seifahrt et al. (2007) in all three bands while they have a similar continuum slope as the ones reported by McElwain et al. (2007). Dividing our spectra by the ones reported by Seifahrt et al. (2007) reveals differences in the overall spectral slopes of 22%, 48% and 15% respectively in J, H and K. This difference is of 8% in J and of 17% in H when compared to McElwain et al. (2007) where most of the H-band difference lies in the bluer spectral range with a 14% continuum difference below 1.63 μm. The difference between the two spectra at the redder end is then of only $\sim 3\%$.

A second difference is seen for the $Pa\beta$ emission line, which is weaker by about an order of magnitude in our spectrum compared to that of Seifahrt et al. (2007). While it is detected with an equivalent width of EW($Pa\beta$) = -3.83 ± 0.15 by these authors, it is detected with an EW($Pa\beta$) = -0.46 ± 0.08 in ours. Emission-lines of PMS accreting

[1]Note that the McElwain et al. (2007) spectra were taken during the OSIRIS commissioning run. The lower S/N is not representative of the camera performance as several adjustments were made to the camera after these observations were taken.

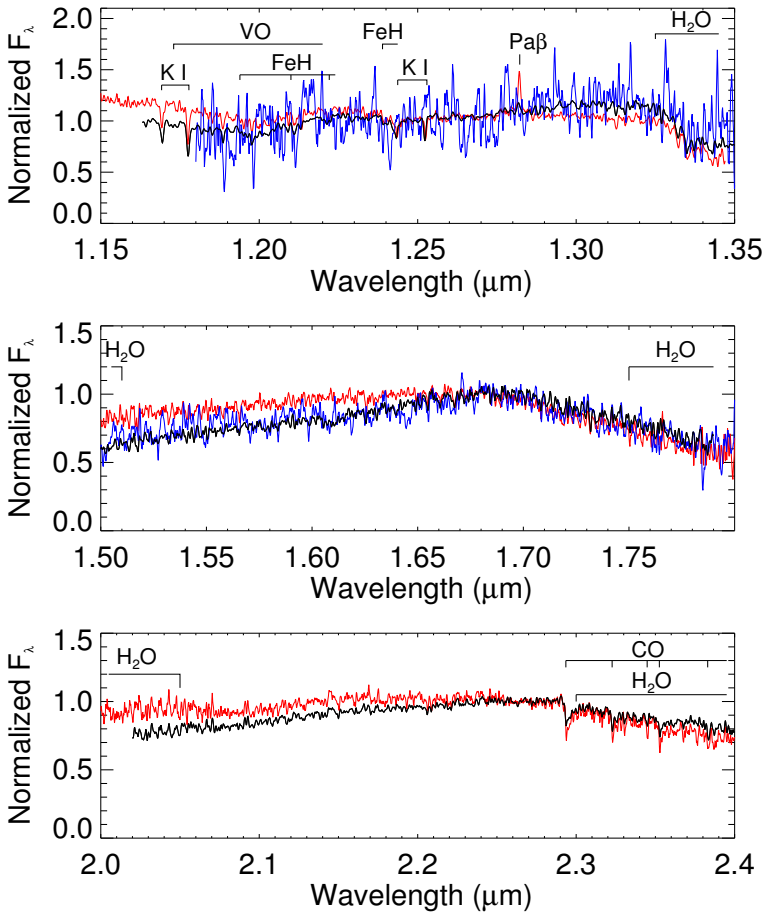

Figure 2.5 Comparison of GQ Lup b *JHK* spectra obtained in this work (black lines) with the ones previously published by Seifahrt et al. (2007) (red lines) and by McElwain et al. (2007) (blue lines). The NIFS spectra were convolved by a Gaussian kernel to get similar spectral resolution as in Seifahrt et al. (2007), namely 2500, 4000 and 4000 in *JHK* respectively. The McElwain et al. (2007) spectra are displayed at their full resolution of $\approx$ 2000 in *J* and *H*. The main absorption/emission features are shown for each band. The spectra are normalized at 1.245, 1.68 and 2.29 μm respectively in *JHK*.

objects are known to vary either due to accretion variability, to projection effects on the accreting column rotating around the object or to hot spots that are not always visible to the observer due to the object rotation (see Scholz & Jayawardhana, 2006 and reference therein for more details). The strongest $Pa\beta$ variations found in the literature were reported by Natta et al. (2006) who analyzed a sample of 14 BDs also observed by Gatti

Table 2.3. Emission/absorption line equivalent width comparison

Source	$EW[Pa\beta]$ [Å]	EW[KI(1.169 μm)] [Å]	EW[KI(1.178 μm)] [Å]	EW[KI(1.244 μm)] [Å]	EW[KI(1.253 μm)] [Å]
This work:	-0.46 ± 0.08	2.12 ± 0.32	2.97 ± 0.44	2.30 ± 0.26	1.40 ± 0.17
Seifahrt et al. (2007):	-3.83 ± 0.12	2.22 ± 0.19	2.51 ± 0.40	1.72 ± 0.15	1.61 ± 0.17

et al. (2006) one to two years later. They found a variation of a factor of two at most for all the objects in their sample except for one that varied by a factor of three. This makes GQ Lup b significantly more variable than any other BD previously observed.

This fact along with the continuum differences raise the possibility that GQ Lup b spectra from Seifahrt et al. (2007) are contaminated by some host star flux. Indeed, such a contamination could explain both the bluer continuum and the significantly stronger $Pa\beta$ emission line measured by Seifahrt et al. (2007) since the spectrum of A is bluer than B and exhibits strong $Pa\beta$ emission. However, the similarities between the KI doublets EW reported in Table 2.3 for both spectra argues against this.

The use of PSF subtraction algorithms could potentially introduce artefacts in the companion spectrum. The fact that different algorithms were used in the three compared papers could then explain the discrepancy between their spectra. As discussed before, we do not believe that artefacts were introduced by our ADI subtraction procedure given the small difference (respectively, 5 and 6% for J- and H-band) between the median non-ADI and ADI spectra. This assertion is reinforced by the presence of the same discrepancy between our results and the ones from Seifahrt et al. (2007) in the K band where no ADI processing was done. At this point, we do not have any satisfactory explanation for the discrepancy between the results of the different papers.

2.5 Discussion

In Figure 2.6, our spectra are compared with the ~ 5 Myr late-M to early-L dwarfs USco J160830-233511, USco J161302-212428 and USco J163919-253409 from Lodieu

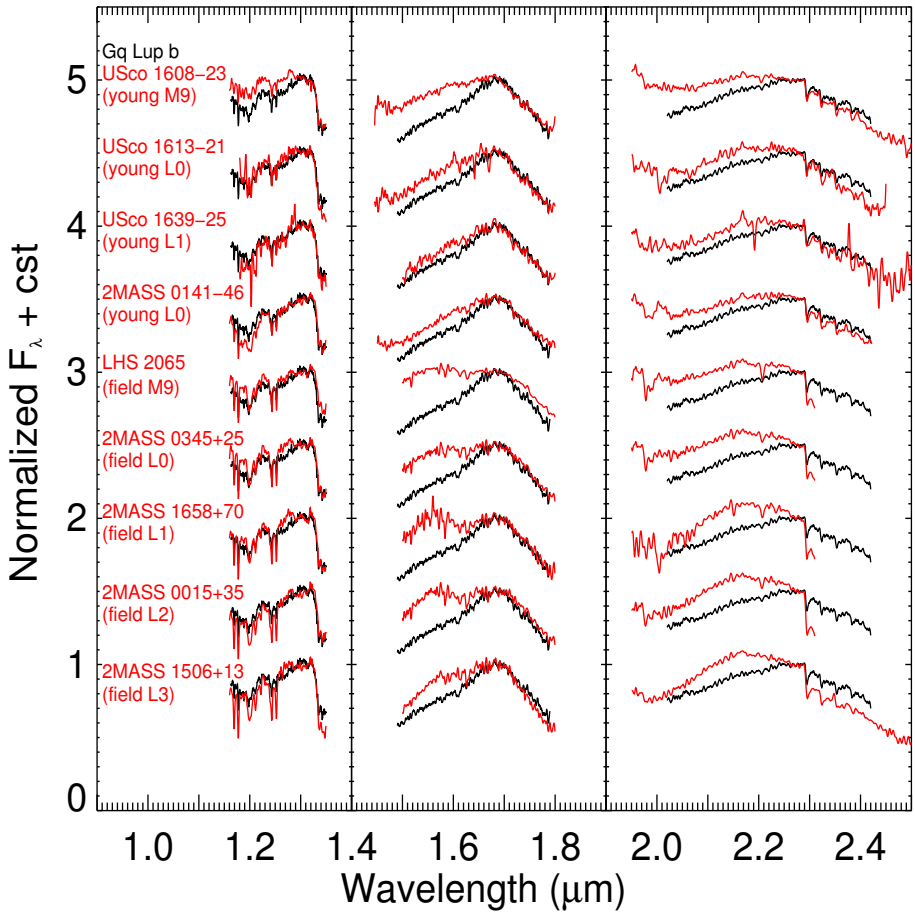

Figure 2.6 Comparison of GQ Lup b spectra with other known young and field brown dwarfs. The J-, H- and K-band spectra were respectively normalized with respect to their flux at 1.29, 1.68 and 2.29 μm. The spectra were convolved with a Gaussian kernel to produce spectra at $R \approx 850$. A constant was added to the different spectra for clarity.

et al. (2008)[2], the $1-50$ Myr 2MASS J014158-463357 (Kirkpatrick et al., 2006) and some older field dwarfs taken from the NIRSPEC Brown Dwarf Spectroscopic Survey (BDSS; McLean et al., 2003)[3] and from Cushing et al. (2005)[4]. Comparison with the field dwarfs shows some absorption from H_2O at 1.34 μm, known as being mostly temperature dependent in low-mass objects (e.g. Gorlova et al., 2003), a feature typical of

[2]The spectra can be found at http:/www.iac.es/galeria/nlodieu/
[3]The spectra can be found at http:/www.astro.ucla.edu/∼mclean/BDSSarchive/
[4]The spectra can be found at http://irtfweb.ifa.hawaii.edu/∼spex/spexlibrary/IRTFlibrary.html

early L (L0-L2) dwarfs. This is also supported by the comparison of the continuum slope shortward of ~ 1.55 μm and longward of ~ 1.68 μm, while the region in between has been reported as being particularly affected by the reduced H_2 collisionally-induced absorption (CIA) in young, low gravity objects such as GQ Lup b (Borysow et al., 1997; Kirkpatrick et al., 2006). This also explains the better agreement in that zone with the younger objects. H_2 CIA has its strongest effect in the K band where GQ Lup b does not exhibit the decrease in flux seen between 2.15 and 2.30 μm in field objects and has significantly shallower CO absorption. The K-band spectrum is better reproduced by the young objects, with the L1 spectra being the most similar.

Hence, we find a spectral type of L1$\pm$1 for this object. This is at the cooler end of the M6-L0 spectral type reported by McElwain et al. (2007) and is consistent with the M9-L4 spectral type inferred by Neuhäuser et al. (2005). This is verified by computing the H_2O index at 1.5 μm defined by Allers et al. (2007), which is believed to be independent of surface gravity. We find a spectral type of L0 $\pm$1 also consistent with our spectral type estimate. The $T_{\rm eff}$ - spectral type relationship of Golimowski et al. (2004) implies $T_{\rm eff} = 2250 \pm 134$ K. However, this relation was only calibrated for evolved field objects and thus tis calibration should be used with caution with young objects. Kirkpatrick et al. (2008) also demonstrate that objects of a similar optically determined spectral type exhibit a significant dispersion in their near-IR relative color. This illustrates the challenge of using such a relation to infer $T_{\rm eff}$, especially from near-IR data.

One can also estimate the effective temperature of GQ Lup b and its gravity by comparing our JHK spectra with synthetic ones generated by the GAIA model v.2.6.1 (Brott & Hauschildt, 2005). The grid explored includes R=5000 spectra ranging from $T_{\rm eff}$ = 2000 to 2900 K and from log g = 1.5 to 5.5 dex with increments of 100 K and 0.5 dex respectively. A χ^2 minimization algorithm was used to find the best fitting parameters. As reported by Kirkpatrick et al. (2006), current atmosphere models poorly reproduce the strong H_2O absorptions between 1.32 and 1.60 μm and between 1.75 and 2.20 μm. Hence, the H band was not used in the fit and those zones were masked

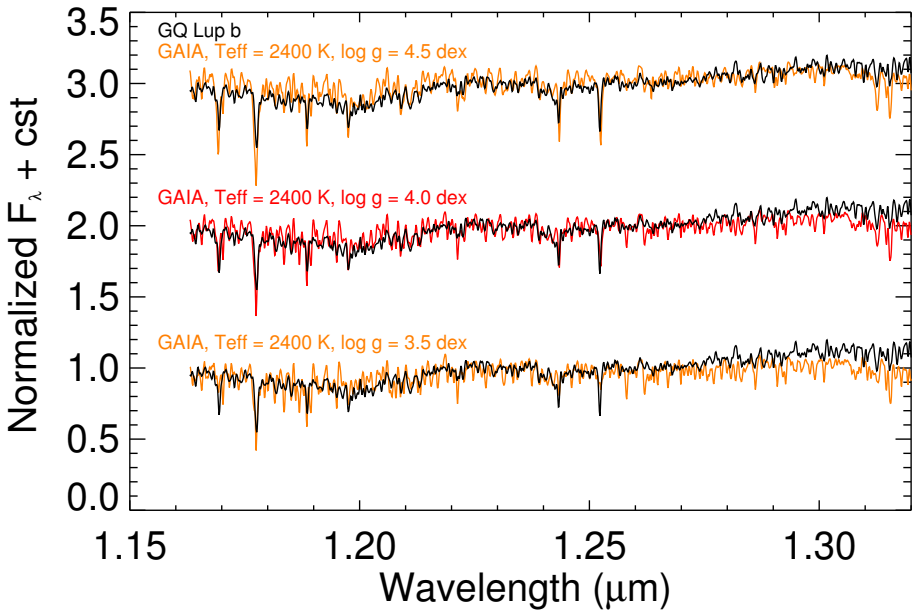

Figure 2.7 Comparison of the GQ Lup b J-band spectra with spectra generated with the GAIA model at $R \approx 5000$. Good fits found by a χ^2 minimisation algorithm were obtained for $T_{\rm eff}$ = 2300 - 2500 K and log g = 3.5 - 4.5 dex with a best fit for $T_{\rm eff}$ = 2400 K and log g = 4.0 dex. The model spectra corresponding to the three gravity grid points at 2400 K are displayed as orange lines with the best fit value as the red line. The observed spectrum is depicted as the black lines.

out of the J- and K-band spectra. The $Pa\beta$ emission line in J-band was also masked out of the fit. The K-band fit is poor and leads to an optimal $T_{\rm eff} > 2900$ K which is largely inconsistent with any previous $T_{\rm eff}$ estimates for this object. However, our K-band spectrum is very similar to other young brown dwarfs of similar spectral types in the zone fitted as seen in Figure 2.6. This indicates that there is still some discrepancy between models and young low-gravity objects in that band. Hence, only the J-band spectrum was used to estimate $T_{\rm eff}$ and log g. Good fits were obtained for $T_{\rm eff}$ = 2300 – 2500 K and log g = 3.5 – 4.5 with a best fit value of $T_{\rm eff}$ = 2400 K and log $g = 4.0$. The model and observed spectra are compared in Figure 2.7 for the J band. The observed H- and K-band spectra as well as the synthetic ones obtained for those best fitting values are shown in Figure 2.8. Hence, we adopt $T_{\rm eff}$ = 2400 ± 100 K and log $g = 4.0 \pm 0.5$ dex.

The same exercise was repeated with grids of AMES-dusty and AMES-cond synthetic spectra and all converged to the same solution.

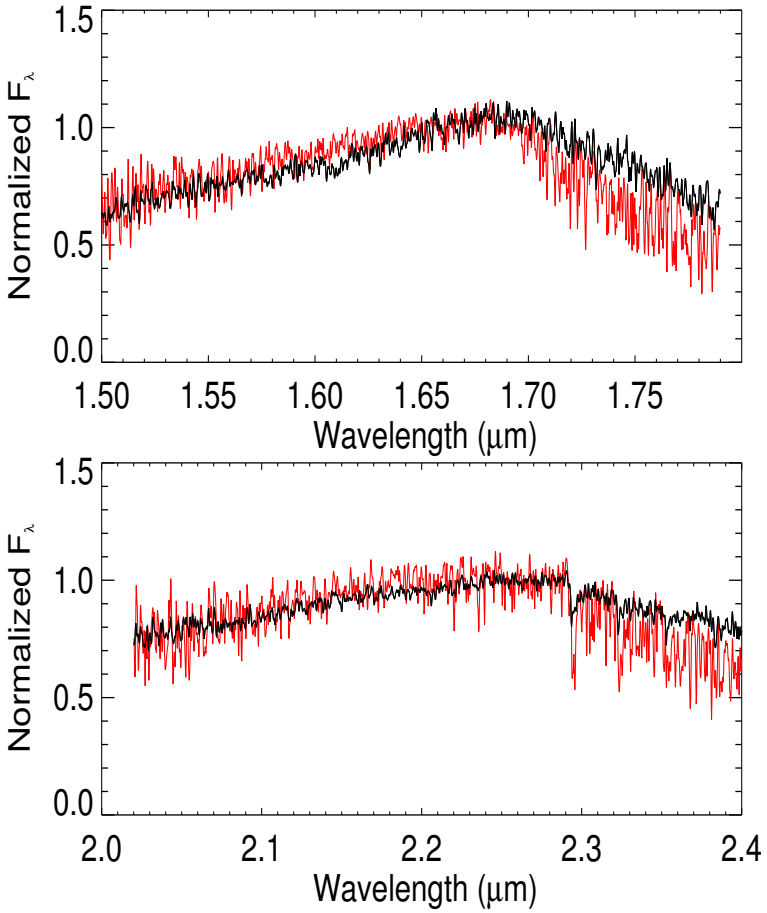

Figure 2.8 Comparison of the GAIA synthetic spectra (red lines) at $T_{\rm eff}$ = 2400 K and log $g = 4.0$ dex with GQ Lup b (black line) spectra in the H- and K-band at $R \approx 5000$. The spectra were normalized at 1.68 and 2.29 μm.

From these results, the mass of GQ Lup b is evaluated following the procedure used in Marois et al. (2008). The model spectra flux is first adjusted to best fit the photometric data points reported in this work and in the literature through a χ^2 minimization algorithm. The resulting spectra along with the photometric measurements used for the fit are plotted in Figure 2.9. The luminosity is then evaluated to be equal to $\log(L/L_\odot) = -2.47 \pm 0.28$ dex by integrating the model flux over the whole wavelength

range and by using the companion distance estimate from Neuhäuser et al. (2008) of 139 ± 45 pc. Adopting the McElwain et al. (2007) age estimate of $1-10$ Myr for the companion and plotting the new luminosity on the DUSTY evolutionary tracks from Chabrier et al. (2000)[5] yields a mass estimate between 11 and 60 $M_{\rm Jup}$ (see Figure 2.10) putting GQ Lup b most likely in the brown dwarf regime.

Even though evolutionary models are uncertain at the young age of GQ Lup (Baraffe et al., 2002), Stassun et al. (2006, 2007) provide a first anchor point with the 1^{+2}_{-1} Myr eclipsing binary 2M0535-05. The lower mass object of this system (36 ± 3 $M_{\rm Jup}$) is particularly interesting as it has a mass comparable to the one estimated for GQ Lup b. The comparison of its dynamically-measured mass with the prediction of the evolutionary model gives an estimate of the model systematic error. Chabrier et al. (2000) evolutionary tracks predict, for an object of such a mass, a luminosity of $\log(L/L_{\odot}) = -2.00$ which underestimates the observed value of 2M0535-05 by a factor of ~ 1.5. Even though this lies only at $\sim 1.5\sigma$ of its measured luminosity and, hence, does not constitute a convincing evidence of a model systematic error, it is still interesting to include this error in our analysis to take into account the model uncertainty. Updating our mass estimate with this systematic error leads to a revised lower mass value of ~ 8 $M_{\rm Jup}$ which is below the boundary between a planetary mass object and a brown dwarf. Our final mass estimate is then of $8-60$ $M_{\rm Jup}$ for GQ Lup b.

2.6 Conclusions

In this paper, we first derived a method to characterize and compensate for the effect of the ADI speckle suppression algorithm applied to IFS data. We found that the ADI process provided a speckle noise attenuation by a factor greater than 3 in J-band and greater than 2 in H-band. We extracted spectra in J-, H- and K-band for the low-mass companion GQ Lup b. The companion $Pa\beta$ emission line was marginally detected. The

[5]The tracks were retrieved from http://perso.ens-lyon.fr/isabelle.baraffe/

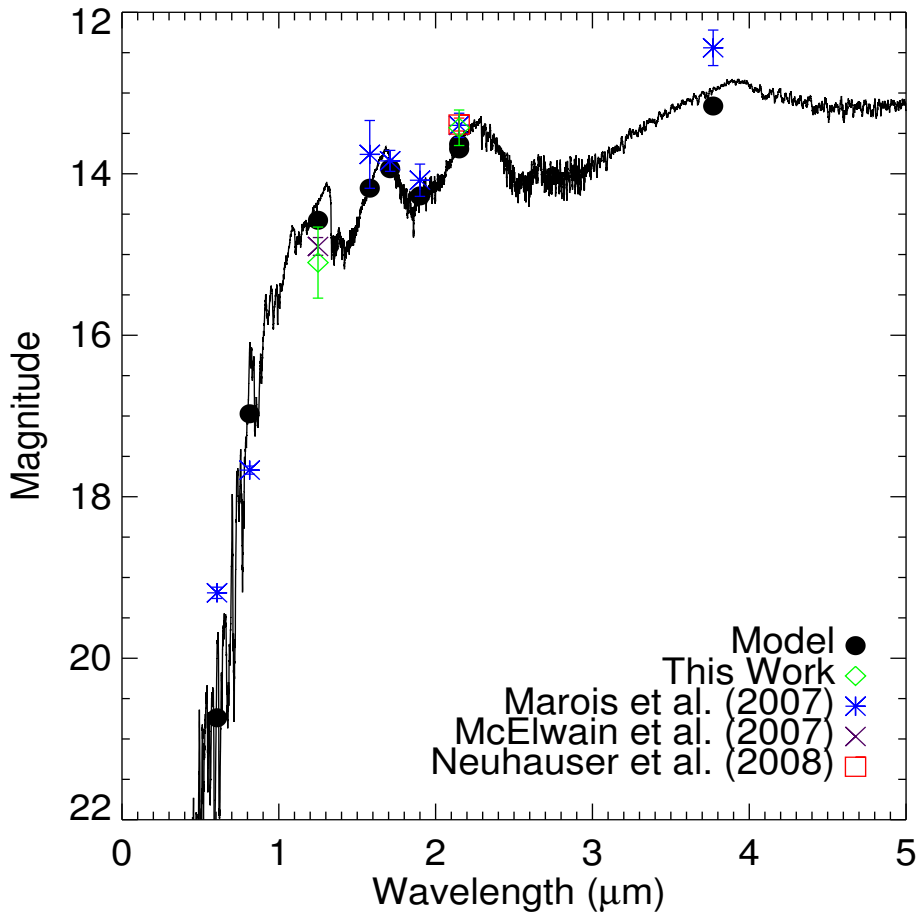

Figure 2.9 Wide band GAIA synthetic spectra compared to photometric measurements taken in this work, in Marois et al. (2007), in McElwain et al. (2007) and in Neuhäuser et al. (2008). The model spectrum integrated flux in a given band is plotted as a black dot. As the measurements from this work and the CH_4 and the L' values from Marois et al. (2007) were made by differential photometry with the host star, the error bars were set to include the variability of GQ Lup A reported by Broeg et al. (2007). These error bars only reflect short term variations while long term fluctuations can also contribute to the discrepancy between predicted and measured values due to host star activity change.

extracted spectra allowed us to constrain its spectral type to $L1 \pm 1$ and to re-evaluate its $T_{\rm eff}$ to 2400 ± 100 K and log g to $3.5 - 4.5$. This leads to the re-evaluation of the bolometric luminosity to $\log(L_{bol}/L_{\odot}) = -2.47 \pm 0.28$ and to a mass estimate of $8 - 60$ $M_{\rm Jup}$ by comparison with predictions from evolutionary models. This defines GQ

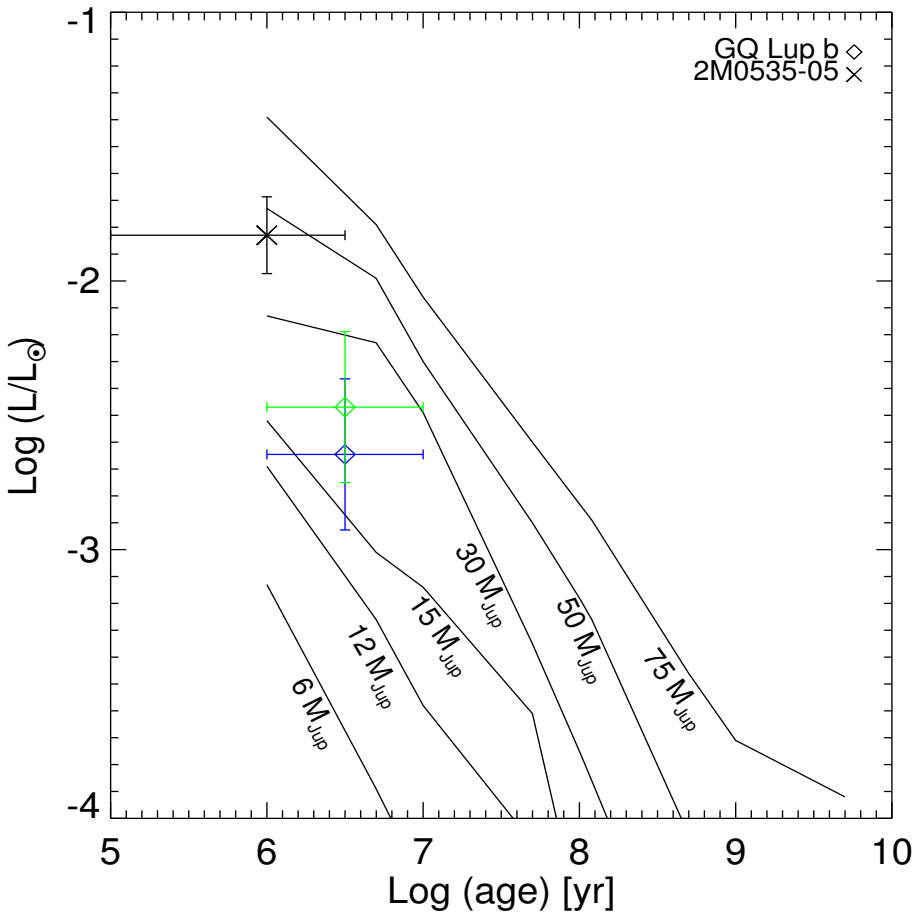

Figure 2.10 GQ Lup b position (diamond symbol) on the evolutionary tracks from Chabrier et al. (2000) that begins at 10^6 years. The luminosity uncertainty is introduced by the lack of precision in the system distance measurement. The lower mass object of the eclipsing binary brown dwarf 2M0535-05 that has a dynamically determined mass of $36 \pm 3\ M_{\rm Jup}$ is also plotted as a reference point. The evolutionary model underestimate the luminosity of this object by a factor of ~ 1.5. Taking this systematic error into account leads to the blue error bars.

Lup b as being most likely a brown dwarf.

Acknowledgments

Based on observations obtained at the Gemini Observatory, which is operated by the Association of Universities for Research in Astronomy, Inc, under a cooperative agree-

ment with the NSF on behalf of the Gemini partnership: the National Science Foundation (United States), the Science and Technology Facilities Council (United Kingdom), the National Research Council (Canada), CONICYT (Chile), the Australian Research Council (Australia), Ministério da Ciência e Tecnologia (Brazil) and SECYT (Argentina).

We would like to thank Andreas Seifahrt, Ralph Neuhäuser, Michael McElwain, James Larkin and J. Davy Kirkpatrick for sharing their spectra with us. We would also like to acknowledge Eric Steinbring at the Canadian Gemini Office for his support during the time proposal redaction and during our data reduction process.

References

Allers, K. N., Jaffe, D. T., Luhman, K. L., Liu, M. C., Smith, J. D., & Cushing, M. C., 2007, Astrophys. J. , 657, 511

Batalha, C., Lopes, D. F., & Batalha, N. M., 2001, Astrophys. J. , 548, 377

Baraffe, I., Chabrier, G., Allard, F. & Hauschildt, & P. H., 2002, A&A, 382, 563

Baraffe, I., Chabrier, G., Barman, T. S., Allard, F. & Hauschildt, P. H., 2003, A&A, 402, 701

Borysow, A., Jorgensen, U. G., & Zheng, C., 1997, A&A, 324, 185

Broeg, C., Schmidt, T. O. B., Guenther, E., Gaedke, A., Bedalov, A., Neuhäuser, R. & Walter, F. M., 2007, A&A, 468, 1039

Brott, I, & Hauschildt, P. H., 2005, ESA SP-576: The Three-Dimensional Universe with GAIA, 565

Burrows, A., Marley, M., Hubbard, W. B., Lunine, J. L., Guillot, T., Saumon, D., Freedman, R., Sudarsky, D. & Sharp, C., 1997, Astrophys. J. , 491, 856

Chabrier, Baraffe, I., G., Allard, F. & Hauschildt, P. H., 2000, Astrophys. J. , 542, 464

Chauvin, G., Lagrange, A.-M., Dumas, C., Zuckerman, B., Mouillet, D. & Song, I., Beuzit, J.-L., & Lowrance, P., 2004, A&A, 425, L29

Cushing, M. C., Rayner, J. T., & Vacca, W. D., 2005, Astrophys. J. , 623, 1115

Gatti, T., Testi, L., Natta, A., Randish, S., & Muzerolle, J., 2006, A&A, 460, 2, 547

Golimowski, D. A., Leggett, S. K., Marley, M. S., Fan, X., Geballe, T. R., Knapp, G. R., Vrba, F. J., Henden, A. A., Luginbuhl, C. B., Guetter, H. H., Munn, J. A., Canzian, B., Zheng, W., Tsvetanov, Z. I., Chiu, K., Glazebrook, K., Hoversten, E. A., Schneider, D. P., & Brinkmann, J., 2004, AJ, 127, 6, 3516

Gorlova, N. I., Meyer, M. R., Rieke, G. H., & Liebert, J., 2003, Astrophys. J. , 593, 2, 1074

Herriot, G. Morris, S., Roberts, S., Fletcher J. M., Saddlemyer, L. K., Singh, G., Véran, J.-P., & Richardson, E. H., 1998, Proc. SPIE, 3353, 488

Janson, M., Brandner, W. & Henning, T., 2008, A&A, 478, 597

Kalas, P., Graham, J. R., Chiang, E., Fitzgerald, M. P., Clampin, M., Kite, E. S., Stapelfeldt, K., Marois, C., & Krist, J., 2008, Science, 322, 5906, 1345.

Kirkpatrick, J. D., Barman, T. S., Burgasser, A. J., McGovern, M. R., McLean, I. S., Tinney, C. GG., & Lowrance, P. J., 2006, Astrophys. J. , 639, 1128

Kirkpatrick, J. D., Cruz, K. L., Barman, T. S., Burgasser, A. J., Looper, D. L., Tinney, C. GG., Gelino, C. R., Lowrance, P. J., Liebert, J., Carpenter, J. M., Hillenbrand, L. A., & Stauffer, J. R., Astrophys. J. , 2008, 689, 1295

Lafrenière, D., Doyon, R., Nadeau, D., Artigau, É., Marois, C., & Beaulieu, M., Astrophys. J. , 2007, 661, 1208

Lafrenière, D., Jayawardhana, R., & van Kerkwijk, M. H., 2008, ApJ, 689, L153

Lagrange, A.-M., Gratadour, D., Chauvin, G., Fusco, T., Ehrenreich, D., Mouillet, D., Rousset, G., Rouan, D., Allard, F., Gendron, É., Charton, J., Mugnier, L., Rabou, P., Montri, J., & Lacombe, F., 2008, A&A Letters, 2009, AA, 493, 21L.

Lodieu, N., Hambly, N. C., Jameson, R. F., & Hodgkin, S. T., 2008, MNRAS, 383, 1385

Marois, C., Lafrenière, D., Doyon, R., Macintosh, B., & Nadeau, D. 2006, Astrophys. J. , 641, 556

Marois, C., Macintosh, B., & Barman, T., 2007, Astrophys. J. , 654, L151

Marois, C., Macintosh, B., Barman, T., Zuckerman, B., Song, I., Patience, J., Lafrenière, D., & Doyon, R., 2008, Science, 322, 5906, 1348.

McElwain, M. W., Metchev, S. A., Larkin, J. E., Barczys, M., Iserlohe, C., Krabbe, A., Quirrenbach, A., Weiss, J., & Wright, S. A., 2007, Astrophys. J. , 656, 505

McGregor, P., Hart, J., Conroy, P., Pfitzner, L., Bloxham, G., Jones, D., Downing, M., Dawson, M., Young, P., Jarnyk, M., & van Harmelen, J., 2002, Proc. SPIE, 4841, 178

McLean, I. S., McGovern, M. R., Burgasser, A. J., Kirkpatrick, J. D., Prato, L., & Kim, S. S., 2003, Astrophys. J. , 596, 561.

Natta, A., Testi, L., & Randich, S., 2006, A&A, 452, 245

Neuhäuser, R., Guenther, E. W., Wuchterl, G., Mugrauer, M., Bedalov, A., & Hauschildt, P. H., 2005, A&A, 435, L13

Neuhäuser, R., Mugrauer, M., Seifahrt, A., Schmidt, T. O. B., & Vogt, N., 2008, A&A, 484, 281

Schmidt, T. O. B., Neuhäuser, R., Seifahrt, A., Vogt, N., Bedalov, A., Helling, Ch., Witte, S., & Hauschildt, P. H., 2008, A&A, 491, 311

Scholz, A., & Jayawardhana, R., 2006, Astrophys. J. , 638, 1056

Seifahrt, A., Neuhäuser, R. & Hauschildt, P.H., 2007, A&A, 463, 309

Sparks, W. B., & Ford, H. C., 2002, Astrophys. J. , 578, 543

Stassun, K. G., Mathieu, R. D., & Valenti, J.A., 2006, Nature, 440, 311

Stassun, K. G., Mathieu, R. D., & Valenti, J.A., 2007, Astrophys. J. , 664, 1154

Thatte, N., Abuter, R., Tecza, M., Nielsen, E. L., Clarke, F. J. & Close, L. M., 2007, MNRAS, 378, 1229

CHAPITRE 3

RÉSULTATS DE TESTS EN LABORATOIRE D'UN SPECTROGRAPHE À CHAMP INTÉGRAL OPTIMISÉ POUR L'IMAGERIE À HAUT-CONTRASTE

LABORATORY RESULTS OF AN INTEGRAL FIELD SPECTROGRAPH OPTIMIZED FOR HIGH-CONTRAST IMAGING

JEAN-FRANÇOIS LAVIGNE[abc], RENÉ DOYON[a] AND DAVID LAFRENIÈRE[d]

Submitted to: *the Publications of the Astronomical Society of the Pacific*

Abstract

The detection of faint companions to stars is limited by the speckle noise introduced by optical defects in the optical path. Integral field spectrographs (IFS) have been proposed to attenuate this noise through spectral differential imaging. While IFS are planned to be used for this task on the next generation of planet imaging cameras, little is known about their actual performance as none of the current on-line IFS are optimized for high-contrast imaging. In this paper, we present laboratory tests made with a lenslet-based IFS optimized for high-contrast imaging. Data cubes were obtained in the H band with a spectral resolution of $R \sim 40$ over a field-of-view of 45 λ/D. Artificial methanated and non-methanated companions were inserted in the data to test four speckle suppression algorithms, namely the simple difference, the double difference, the spectral deconvolution and a new algorithm developed in this paper, dubbed the spectral

[a]Département de physique, Université de Montréal, C.P. 6128, succ. Centre-Ville, Montréal, QC, Canada

[b]Herzberg Institute of Astrophysics, 5071 West Saanich Road, Victoria, BC, Canada

[c]Institut national d'optique, Parc technologique du Québec métropolitain, 2740 rue Einstein, Québec, QC, Canada

[d]Department of Astronomy and Astrophysics, University of Toronto, 50 St. George Street, Toronto, ON, M5S 3H4, Canada

twin algorithm. It is found that the spectral twin algorithm is the most efficient method for improving the signal-to-noise ratio (S/N) of the companion. The methanated companion S/N is improved by a factor up to 14 while the non-methanated one is increased by a factor of 2. An iterative algorithm improving the accuracy of the retrieved companion spectrum once its position is known is also presented.

3.1 Introduction

The advent of adaptive optics systems (AO) on ground-based 8-10 m class telescopes along with the development of speckle suppression techniques both on the ground and in space have led to the first imaging detection of a planetary mass companion around the young brown dwarf (BD) 2M1207 (Chauvin et al., 2004, 2005) and several other companions straddling the BD boundary (Neuhäuser et al., 2005; Biller et al., 2006; Béjar et al., 2008). This was followed by deep imaging surveys (Lafrenière et al., 2007; Biller et al., 2007; Nielsen et al., 2008) whose null results have put the first constraints on the gas giant planet frequency beyond $\sim$ 10 AU for host stars less massive than the Sun. More recently, direct imaging has yielded the first unambiguous detections of exoplanets around main sequence stars: three around the young A5V star HR8799 (Marois et al., 2008), one around Fomalhaut (Kalas et al., 2008) and two other candidates (1RXS J160929.1, Lafrenière et al., 2008; β Pic, Lagrange et al., 2008) both awaiting a second epoch measurement to assess their companionship.

The direct detection of such bodies is particularly challenging given the large brightness ratio and small separation between the host star and the faint companion. In particular, the quasi-static speckles induced by optical aberrations in the telescope/instrument optical system have the most dramatic impact on faint companion detections (Schneider & Silverstone, 2003; Biller et al., 2004; Marois et al., 2005; Masciadri et al., 2005). One important and promising speckle suppression technique is the spectral differential imaging (SDI) which consists in simultaneously acquiring narrowband images at adja-

cent wavelengths across a spectral feature exhibited by the companion, like the methane absorption near 1.6 μm. Since the star is essentially featureless over this spectral range, a judicious subtraction of the images can suppress the speckles and better reveal the faint companion (Smith, 1987; Rosenthal et al., 1996; Racine et al., 1999; Marois et al., 2000). The first implementations of the SDI technique was the multi-channel camera (MCC) TRIDENT (Marois et al., 2005) on the Canada-France-Hawaii Telescope and the SDI module of NACO on the VLT (Lenzen et al., 2004). Laboratory tests on the former showed that its performance is in practice severely limited by the differential aberrations between the different imaging channels (Marois et al., 2005). The performance can be quantified by defining a speckle noise attenuation factor as the ratio of the speckle noise present in the initial image over the one measured after speckle suppression processing. This factor was found to be about 2-3 for a TRIDENT-like camera. Lafrenière et al. (2007) showed that this performance can be greatly improved (roughly by a factor of five) by inserting a holographic diffuser at the entrance focal plane to break the light coherence before separating the imaging beam into the different channels. More specifically, the attenuation factor reached with the holographic diffuser was $\sim$ 15 at 5 λ/D and $\sim$ 10 at 20 λ/D. The holographic diffuser experiment clearly demonstrates the detrimental effect of differential aberrations on speckle suppression performance with a standard MCC *à la* TRIDENT or VLT-SDI.

This suggests that an alternative implementation of SDI using an integral field spectrograph (IFS) (Sparks & Ford, 2002) can be an interesting avenue. This is particularly true for future instruments as the spectral information necessary for the companion characterization is also available. Since such IFS are planned as part of the next generation of "planet finder" instruments on both Gemini (Macintosh et al., 2006) and the VLT (Dohlen et al., 2006), a proper characterization of the IFS speckle suppression performance is highly desirable, especially as little is currently known on the subject.

The performance of an IFS camera was first evaluated theoretically by Sparks & Ford (2002) based on simulated data cubes that ignore some noise sources such as spectral

cross-talk inherent to the data cube reconstruction or any additional instrumental errors. Berton et al. (2006) simulated IFS detector images from which a data cube was reconstructed to assess those error sources. They found that the IFS can achieve a speckle noise attenuation factor of $\sim 10^3$ at radii varying between $0.3''$ and $1.0''$. However, those simulations only take into account error sources already known to the programmer; real data are missing to confirm theoretical predictions. The high-contrast imaging performance of existing IFSs such as SINFONI (Thatte et al., 2007; Janson et al., 2008; Seifhart et al., 2007), OSIRIS (McElwain et al., 2007) and NIFS (Lavigne et al., 2009) linked to AO systems have been tested over the past few years. Janson et al. (2008) compared the speckle attenuation performance obtained with the MCC camera SDI at the VLT used in combination with the NACO AO system with SINFONI data to conclude that NACO-SDI was better for companion detection while it is preferable to use SINFONI for follow-up observations. However, they noted that SINFONI is not an IFS optimized for high-contrast imaging limiting its performance for this purpose. This is also true for all other existing IFSs. To be optimized for high-contrast imaging, an IFS should ideally be based on the lenslet concept to spatially sample the PSF before its spectral separation to limit spectral differential aberrations that are introduced in the different spectral optical paths. Marois et al. (2005) have identified such aberrations as limiting the performance of MCC by slightly modifying the speckle pattern from a wavelength to another. If the PSF is spatially sampled by lenslet before the spectral separation, these aberrations only slightly affect the lenslet PSF shape on the detector and has a negligible impact on the integrated flux. Of the three IFS mentioned above, only OSIRIS uses this concept but its implementation (densely packed spectra leading to high cross-talk) makes it difficult to assess its inherent speckle suppression capability. The telescope PSF should also be at least Nyquist sampled to avoid additional noise during the image manipulation caused by undersampled features. None of the cameras above allow such a fine spatial sampling. Overall, it is difficult to provide an objective assessment of the inherent speckle suppression performance of an IFS based on the existing instrumenta-

tion.

To shed some light upon that matter, an IFS prototype optimized for high-contrast imaging was built and tested in the laboratory. The IFS design and the laboratory setup used to test its performance are presented in section 2. It is followed in section 3 by a description of the data acquired and of the data pipeline used to reconstruct the data cube from the raw detector image. Section 4 describes the four speckle suppression algorithms investigated in this paper. Three are taken from the literature and one is an innovative speckle suppression algorithm specifically designed for IFS data. Their performance is compared with other algorithms in section 5. In section 6, an iterative algorithm used to extract a companion spectrum once its position is known is proposed and its performance is evaluated from our laboratory data.

3.2 Testbed Description

The ability of an IFS to suppress speckle noise was evaluated from a testbed operating in the H band. The testbed is composed of an optical relay generating a polychromatic PSF followed by a lenslet-based IFS and a cryostat housing a cold H-band filter and a 1024×1024 Hawaii-1 infrared (IR) detector cooled to 77 K.

The IFS principle is illustrated in Figure 3.1. A lenslet array spatially samples the PSF in the focal plane. The light is then collimated, dispersed through a "direct vision" prism (hereafter referred to as the prism) and reimaged on the detector. The prism is made of two air-spaced glasses and it is designed to provide the desired dispersion with no deviation at 1.65 μm. The prism axis of dispersion, which is aligned with the detector pixels, is inclined compared with the lenslet array. The angle is set to allow enough detector pixels on which to disperse the spectrum while maximizing the number of spectra on the detector. It is also chosen so that adjacent spectra fall on the same row of pixels. An example of the spectrum layout on the detector is shown in Figure 3.2. A lenslet-based IFS was chosen to spatially sample the PSF before the wavelength dispersion.

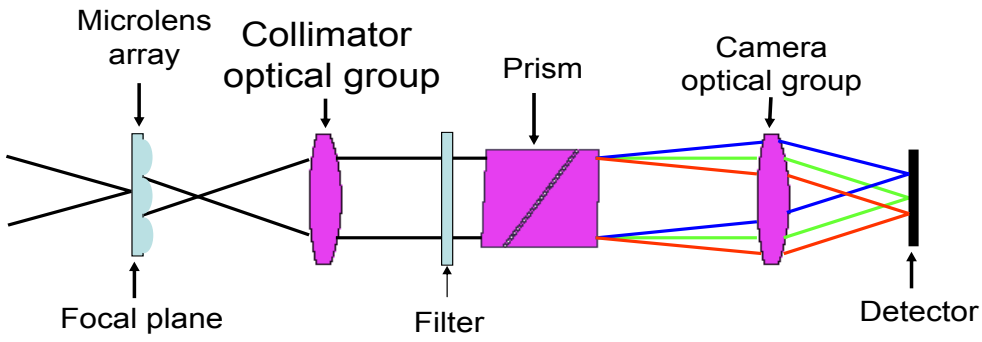

Figure 3.1 Principle of operation of the IFS. A microlens array samples the star PSF in the focal plane. The beam is then collimated and goes through a direct vision prism with an axis of dispersion tilted compared to the lenslet array. The resulting beam is then imaged on the detector to obtain a spectrum of each spatial sample, as shown in Figure 3.2.

Differential aberrations in the optical paths taken by the wavelenghts after their dispersion by the prism then only affect the lenslet PSF shape instead of the whole speckle pattern as in the MCC case. As these aberrations between different wavelengths were identified as being the limiting source of noise in MCCs (Marois et al., 2005; Lafrenière et al., 2007), they can be mitigated in a lenslet based IFS.

The design of the IFS has been optimized for faint companion detection. The focal ratio of the optical relay was set so that the spatial sampling of the PSF by the lenslet array in the focal plane was slightly better than Nyquist at the shortest wavelength. A proper spatial sampling is especially critical when using PSF rescaling algorithms for

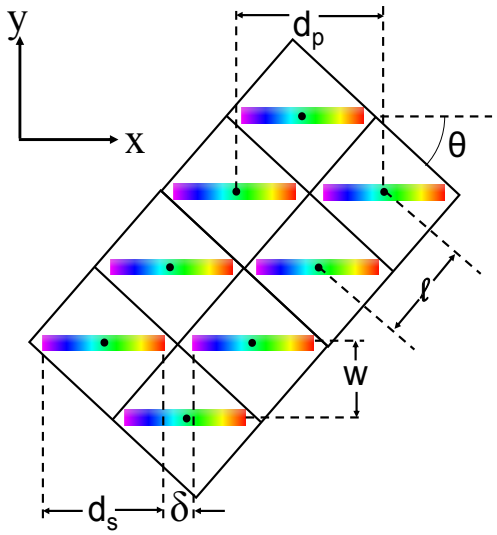

Figure 3.2 Schematic layout of the spectra on the detector. The lenslet array is tilted with respect to the dispersion axis to have more pixels available for dispersion. The x and y axes represent the detector orientation and the solid lines, the lenslet grid projected onto the detector. The parameters are defined in Table 3.1.

speckle noise attenuation. Simulations have shown that the performance of such algorithms are severely affected for undersampled images.

The cross-talk between spectra in the direction perpendicular to the dispersion axis has been identified as a critical parameter in the design of a lenslet-based IFS (Bacon et al., 1995). Antichi et al. (2009) proposed a new IFS implementation they named BIGRE that can reduce this cross-talk. Our approach was instead to minimize it by separating the spectra by 4 pixels and by choosing the reimaging optics focal ratio (f/8.3) to yield a diffraction limited PSF FWHM approximately equal to the pixel width. The spectral resolution ($R \sim 40$) was chosen to be similar to the one planned for the Gemini Planet Imager (GPI; Macintosh et al., 2006). The IFS magnification was set to yield the correct lenslet separation on the detector. A summary of the parameters used for the camera optical design can be found in Table 3.1.

The IFS optical system is illustrated in Figure 3.3 and the optical prescriptions are found in Table 3.2. The collimator group and reimaging camera glasses are made of

Table 3.1. IFS design parameters

Parameter	Value	Parameter	Value
Detector pitch (in μm)[a]	18.5	Lenslet f-number	5
Detector size (in pixels)	1024	Camera optics f-number	8.28
Minimum wavelength (in μm)	1.50	IFS pupil diameter (in mm)	20
Maximal wavelength (in μm)	1.80	Length of spectra (d_s in pixels)[a]	18.4
Spectral bandpass	0.18	Dispersion distance (d_p in pixels)[a]	20
Spectral spacing (w in pixels)[a]	4	Spectral spacing (δ in pixels)[a]	2.0
Spectral resolution	40	Lenslet tilt ($tan\ \theta$)[a]	2
Lenslet pitch (l in μm)	100	Optical magnification	1.65
Lenslets spatial sampling	2.5	FOV (in λ/D)	45
Focal ratio at lenslet	166.67	Number of lenslets in a FOV	114
Lenslet array diameter (mm)	15.36		

[a]See Figure 3.2 for an illustration of the different parameters

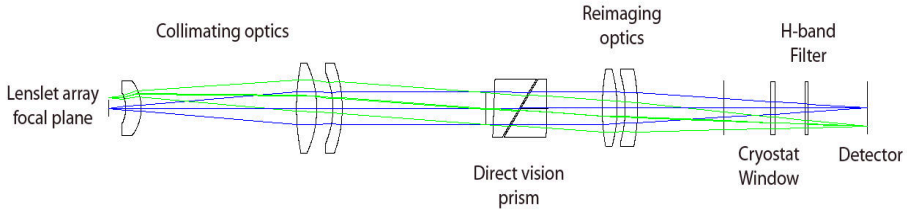

Figure 3.3 IFS optical system. The ray tracing starts at the lenslet focal plane. Three lenses are used to collimate the beam and form a pupil plane in front of the prism. This is followed by a direct vision prism and the reimaging optics composed of two lenses. The beam goes through the cryostat window and through an H-band filter before reaching the detector.

ZnSe, BaF_2 and SF6. The prism, made of BaF_2 and Fused Silica, represents a good glass combination for a single waveband. A detailed description on how to optimize the glass selection for multiple wavebands and more details on the optical design and performance can be found in Lavigne et al. (2006a,b).

The IFS is preceded by an optical relay generating a PSF on the lenslet array. This relay is fed by a white light source located just behind a 25 μm diameter pinhole. It is then reimaged on the IFS lenslet array using a single meniscus lens from Thorlabs

Table 3.2. IFS Optical Prescriptions

Lens Element	Radius 1 (mm)	Radius 2 (mm)	Thickness (mm)[a]	Glass
Lens 1:	−17.26	−22.89	10.00	ZnSe
Lens 2:	112.72	−53.58	13.15	BaF_2
Lens 3:	−43.95	−66.07	6.00	SF6
Lens 4:	108.52	−73.28	9.63	BaF_2
Lens 5:	−60.89	−96.39	8.00	SF6
Prism Element	Tilt 1 (°)	Tilt 2 (°)	Thickness (mm)[a]	Glass
Prism 1:	2.67	34.03	16.60	BaF_2
Prism 2:	34.03	0.79	16.60	Fused Silica
Element Separation			Thickness (mm) [a]	
Lens 1 - Lens 2			100.647	
Lens 2 - Lens 3			10.479	
Lens 3 - Prism 1			98.315	
Prism 1 - Prism 2			1.000	
Prism2 - Lens 4			36.098	
Lens 4 - Lens 5			5.282	
Lens 5 - Detector			147.209	

[a]The thickness is measured on the optical axis

(LE1261). A 6 mm diameter stop was placed in front of the lens to obtain the required focal ratio ($f/167$) incident on the lenslet array. The resulting PSF has a very high Strehl ratio ($\gtrsim 95\%$) due to the small number of optical elements used in the relay and the slow f-number of the incident beam ($f/167$), hence speckles are barely visible. In order to test the performance of the camera for speckle noise attenuation, some speckles had to be generated. This was done by adding three H-band filters at the stop position during PSF observations. This had the effect of adding speckles while keeping the Strehl ratio over 0.9. Narrowband filters were also added at this location for wavelength calibration purposes.

3.3 Data Acquisition and Reduction

This section describes the observations taken on the laboratory testbed and the data reduction pipeline used to build the final data cube. First, a sequence of 12 images was taken by alternating between a light source turned on and off resulting in 6 PSF and 6 dark images. Each of the 12 images was composed of 60 co-additions of 60s yielding

an hour long total exposure time. The center of the PSF was saturated to yield deeper images at larger radii.

Spectral calibration images were acquired by observing the uniformly illuminated lenslet array through three warm 1% narrowband filters centered at 1.584 μm, 1.639 μm, 1.695 μm. A wideband flat field was acquired with the lenslet array in place, as well as one without the lenslet array in place for bad pixel mapping. Corresponding darks were acquired for each of these images.

Calibration data were dark subtracted and bad pixels were corrected by interpolation from their closest neighbors. The spectral dispersion law at different field positions was computed from the narrowband images. Since the measured dispersion was in excellent agreement with the predictions from the Zemax optical model, the theoretical dispersion law was adopted to infer the wavelength calibration of each spectrum. The next step was to integrate the flux of the three brightest pixels perpendicular to the dispersion axis for each spectrum. The same integration box was applied to the corresponding pixels of the wideband flat field. Each flat field spectrum was corrected for low order intensity variations and was normalized to unity to build the flat field image. Each spectrum was divided by its corresponding flat field spectrum. Finally, the data cube was built by interpolating the values of each spectrum to a common wavelength vector. Hereafter, the term spaxel will be used to refer to a single (x, y, λ) element in the resulting reconstructed data cube.

A narrowband flat field image (see Figure 3.4) was used to evaluate the IFS image quality; a PSF FWHM is typically $\sim$ 1.4 pixels. Using simulated data and assuming a uniform illumination of the lenslet array, 89% of the total flux is estimated to be comprised within the three pixel integration box. The flux fraction from nearby spectra contaminating the integration box was evaluated to be $\sim 4\%$.

The logarithmic display of a broadband PSF image on the IFS detector is shown in Figure 3.5. This illustrates the spectra disposition on the detector and shows that they are well separated one from another. An example of a reconstructed data cube slice is also

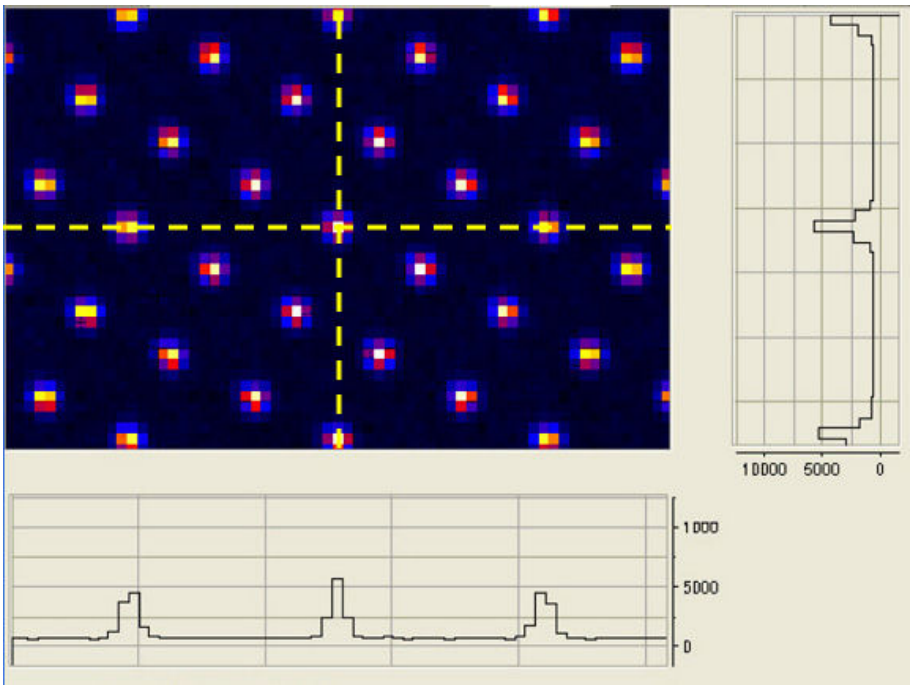

Figure 3.4 Zoomed in narrowband flat field taken with a filter centered at 1.685 μm. The microlens PSF intensity plots along the dashed lines are shown on the right side and at the bottom of the image.

shown on the right panel of that figure. The Airy rings along with speckles are clearly visible.

In preparation for the application of the speckle suppression algorithms, the median radial intensity profile about the PSF center of each data cube slice was subtracted and an unsharp mask with a Gaussian kernel of 7.5 pixel FWHM ($\sim$ 3 times the PSF FWHM) was applied. The images were then convolved by a circular aperture having a 2.5 pixel diameter to build an image representative of the integrated flux over a FWHM.

3.4 Speckle Suppression Algorithms

This section presents four different speckle suppression algorithms used to evaluate the high-contrast imaging performance of our testbed: the simple and double difference (SD and DD) introduced by Marois et al. (2000), the spectral deconvolution algorithm

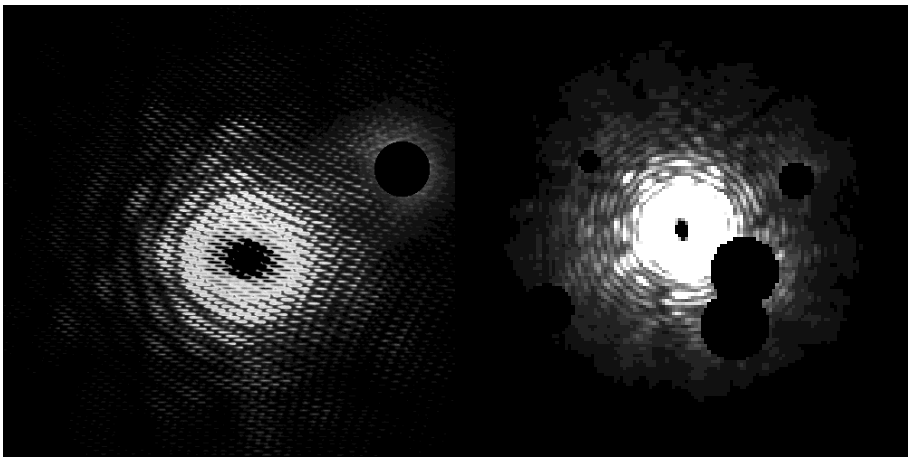

Figure 3.5 The left panel shows a display of a zoomed in detector image. This illustrates the spectra disposition on the detector. It can be seen that the spectra are well separated. The right panel shows a display of a reconstructed data cube slice. Ghost images were masked out by dark circles while the PSF peak was saturated to obtain deeper images. Some broken Airy rings typical of high Strehl PSFs are seen.

presented by Sparks & Ford (2002) and finally a novel"spectral twin" algorithm whose motivations will be clear below. In one slice of a data cube, the speckle noise of the PSF at a given radius is calculated by first subtracting its radial profile and then by computing the standard deviation (STD) of the residuals at that radius. The speckle noise attenuation factor is defined as the ratio of the speckle noise present in the initial image over that measured after speckle suppression processing. This speckle noise attenuation factor is a useful metric to assess speckle suppression performance.

All these algorithms take advantage of the different spectral behavior between speckles and a potential companion. In an ideal case where all wave-front aberrations are generated only by phase errors at the pupil plane, the resulting PSF speckle pattern is, to first order, the same at all wavelengths except for an overall change of scale. More precisely, as one scans through longer wavelengths, speckles move radially outward, while a real companion would remain fixed. Of course, real systems have out-of-pupil aberrations as well as amplitude aberrations, but a significant part of the speckle pattern would

nevertheless exhibit the same behavior, which can be exploited to enhance sensitivity to planets.

In the following, we are considering a data cube that has been rescaled to bring the speckle patterns at different wavelengths to a common scale. This operation results in the companion moving inward with wavelength throughout the data cube, its total displacement depending on its angular distance from the host star.

3.4.1 Simple and Double Difference

These two algorithms consist in differentiating images at different wavelengths to remove the stellar PSF while keeping the flux of the companion. They rely on differences in spectral features between the star and companion, such as the methane absorption at 1.6 μm which is present in the atmosphere of a cool planet but absent from that of the star.

The SD and DD can further be used to seek companions with no significant spectral features. In this case, the wavelengths are selected to yield a sufficient companion radial displacement in the rescaled images, preventing flux loss in the differentiation process. A larger wavelength difference is then needed as companions are sought at smaller radii.

The simple difference is a difference between two images at different wavelengths, I_{λ_i} and I_{λ_j}, in the rescaled data cube. The slices are first normalized to the same integrated intensity and differentiated:

$$SD_{\lambda_j,\lambda_i} = I_{\lambda_j} - I_{\lambda_i}$$

The main limitation of the simple difference is the PSF chromatic evolution (Marois et al., 2000). The phase error introduced by a given aberration is wavelength dependent, resulting in speckles which scale also in intensity with wavelength. Thus, the difference of two PSFs of different wavelengths necessarily leaves some residuals. This PSF chromaticity limits the theoretical speckle noise attenuation factor to $\lambda/\Delta\lambda$ (Marois et al., 2005), where λ is the wavelength of the first image and $\Delta\lambda$ is the wavelength difference

between the two images. Hence, the theoretical limit for two wavelengths separated by one spectral resolution element in our testbed is an attenuation factor of ~ 40.

The SD performance can be improved through a double difference consisting in differentiating two simple differences (Marois et al., 2005):

$$DD = k_2 \left(k_1 SD_{\lambda_k,\lambda_i} - SD_{\lambda_j,\lambda_i} \right), \tag{3.1}$$

where k_1 and k_2 are normalizing constants. The former insures that both SDs have the same amplitude of residuals while the latter insures that the initial companion flux is conserved in the final image. The normalized simple differences have the same chromatic evolution which is subtracted to the first order in the DD, considerably improving the speckle noise attenuation. The wavelengths chosen to analyze our laboratory reconstructed data cube were 1.576 μm, 1.615 μm and 1.656 μm, appropriate for the methane spectral feature. The slices are separated by one spectral resolution element to maximize the speckle correlation between images. Marois et al. (2000) demonstrated that the theoretical noise attenuation ($\Delta I/I$) limit of this algorithm is given by:

$$\frac{\Delta I}{I} \simeq (3 - 2\sigma_\phi^2)\sigma_\phi^2 \frac{\Delta\lambda_{ij}\Delta\lambda_{ik}}{\lambda^2}, \tag{3.2}$$

where σ_ϕ^2 is the wavefront phase error variance and this was verified with simulated data. In the present case, this would correspond to $\Delta I/I \sim 7000$ assuming a Strehl ratio of 0.9 and, hence, a phase error of $\sigma_\phi^2 \sim 0.1$ from the Maréchal approximation. However, as mentioned earlier, laboratory tests on the TRIDENT camera showed that its performance is in practice severely limited by the presence of differential aberrations within the different imaging channels of the camera.

3.4.2 Spectral Deconvolution

The goal of this algorithm proposed by Sparks & Ford (2002) is simply to fit the monotonic behavior of the speckle pattern intensity with wavelength in the rescaled data cube. Given a host star with a spectrum varying monotonically with wavelength, a speckle spectrum can be fitted by a low order polynomial in the rescaled data cube and subtracted. A companion moving inward in the rescaled cube would appear as a high frequency in the spectrum and would not be fitted by the polynomial fit. However, the companion radial displacement is shorter at smaller radii resulting in a lower frequency in the spectrum and a significant amount of companion flux may be subtracted by the polynomial fit for such companions.

This algorithm works remarkably well for a perfect data cube for which the speckle evolution with wavelength is ideal, but this is not the case for real data. Indeed, Janson et al. (2008) discussed the non-ideal spectral behavior of AO PSFs that have a varying FWHM with wavelength. Also, the data cube reconstruction errors as well as instrumental errors both contribute to the non-ideal shape of a speckle spectrum in the reconstructed and rescaled data cube. The non-monotonic behavior of the rescaled speckle spectrum led us to develop a new algorithm that does not make any assumption about a speckle spectral behavior. This algorithm is described below.

3.4.3 Spectral Twin Algorithm

Like spectral deconvolution, this algorithm attempts to fit the speckle spectrum. To do so, it takes advantage of the fact that many speckles should be present at a given radius, hence their spectrum should be recurrent while the companion is unique. The presence of a companion will contaminate part of a spaxel spectrum but the uncontaminated part should be reproduced by the spectrum of another spaxel at the same radius. These characteristics can be used to fit the speckle spectrum very efficiently. The principle is very similar to the spectral deconvolution algorithm except that it makes no assump-

tion on the speckle spectral behavior. Instead, it relies on the probability of finding two spaxels with a similar spectrum.

Let us consider the ith spaxel spectrum $S_i(\lambda)$ at a radius r for which a similar spectrum is sought. An annulus of width Δr centered at r is defined as the search zone. An azimuthal zone ϕ_i around the ith spaxel is taken out of the search zone to exclude spaxels that would otherwise be contaminated by a companion centered on the ith spaxel. Each spaxel spectrum, $S_j(\lambda)$, in the search zone is then normalized to the same median value as $S_i(\lambda)$. The next step is to identify the spaxel in the search zone with the spectrum being the most similar to the one of $S_i(\lambda)$. This is done by computing the median of the absolute value of the difference $S_j(\lambda) - S_i(\lambda)$ (hereafter, ε_j). Such a criterion yields a fit less dependent on large excursions introduced by the presence of a companion compared to a criterion based on a χ^2 minimization for example. The spectrum $S_j(\lambda)$ with the minimal ε_j is simply subtracted from $S_i(\lambda)$ to form the final image.

3.5 Companion Detection Results

All the algorithms presented in the previous section can be used to unveil companions in a data cube. The spectral deconvolution and the spectral twin algorithms can be used to extract their spectrum as well. In this section we investigate quantitatively the performance of the different algorithms at accomplishing the first of these tasks and the second will be explored in the next section.

The performance of the different algorithms at finding companions is expected to depend on the companion nature. For example, a companion having a spectrum similar to that of its host star can only be detected through the difference between its spectral behavior and that of a speckle. In the case where the companion has some spectral features different from the host star, these can be exploited to isolate the companion and improve the detection performance. For this reason, we will test the different algorithms for the detection of two types of companions, some having significant methane absorption

(methanated companions) and some without that feature (non-methanated companions). When needed, fake companions will be added to the data cube with a T8 or L1 spectral type as representatives of methanated and non-methanated companions. More precisely the spectral energy distribution (SED) of 2MASS J0415195-093506 was used for the T8 and the SED of 2MASS J03454316+2540233 for the L1[1]. In the particular case of SD and DD, only methanated companions are used to test their performance as these algorithms were primarily developed for MCCs which are optimized for methanated companion detection.

To benefit from a higher signal-to-noise ratio (S/N), the companion detection is usually done using a collapsed version of the data cube (i.e. an image) rather than the data cube itself. We have defined different strategies depending on the nature of the companion sought. The image optimized for the detection of methanated companions is constructed by summing the spectral slices between 1.54 μm and 1.60 μm. This corresponds to the slices in which the companion is at least half as bright as its peak intensity and results in a higher S/N than the collapse of the whole cube for this type of companions. The non-methanated companion does not have a significant absorption band and is then bright in every data cube slices. In this case, there is no reason to favor particular data cube slices for the search of a companion, hence all slices are summed together.

Once the images are built, the capability of the different algorithms to find faint companions is evaluated. One simple performance metric is to use the speckle suppression factor defined earlier. The companion flux loss during differentiation between images in and out of the methane absorption line being low, the speckle noise attenuation factor is, in the case of the SD and DD applied to methanated companions, a good indicator of the algorithm performance. Spectral deconvolution and spectral twin algorithms being both expected to subtract a non-negligible fraction of the companion flux at small radii, a more appropriate metric to measure their relative performance is either an effective noise attenuation factor compensated for the flux loss or the S/N. The uncompensated

[1]The spectra can be found at http://www.jach.hawaii.edu/ skl/LTdata.html

noise attenuation factor and the S/N are discussed below.

3.5.1 Speckle Noise Attenuation Performance

The speckle noise attenuation achieved for each algorithm and for both types of companions is shown in Figure 3.6. Both the SD and DD yield similar speckle noise attenuations implying that the SD is not limited by the PSF spectral evolution. Instead, other instrumental effects in the image formation on the detector and/or data cube reconstruction errors limit the performance. The SD algorithm attenuates the speckle noise by a factor of $8-10$ at $6\ \lambda/D$, slowly decreasing to $2-3$ between 15 and 20 λ/D. This is an improvement of a factor $3-5$ compared to MCCs at small radii, but is not as efficient as an MCC used with a holographic diffuser and is below the theoretical limit of a factor 40. This shows that spatially sampling the PSF before the light dispersion, using a lenslet array, does indeed improve the speckle noise attenuation, but also that other instrumental errors (currently unknown) associated with the IFS as well as data cube reconstruction errors also affect the attenuation performance.

The spectral deconvolution algorithm is extremely efficient at suppressing the speckle noise at small radii when searching for non-methanated companions. It reaches an attenuation factor of 400 at $5\ \lambda/D$ to decrease rapidly to ~ 8 at $15\ \lambda/D$. This very good performance is also well illustrated in Figure 3.7 by the very small residues left at small radii in the image. The very good performance of this algorithm at short radii shows that speckles follow their theoretically predicted behavior in that zone; they have a smooth monotic behavior well fitted a polynomial fit. The spectral twin algorithm cannot reach the same performance due to the limited number of spectra available for searching a twin in that zone. As the speckle intensity becomes smaller at larger radii, the other errors discussed in the previous paragraph become more significant and the monotonic spectral behavior of the speckle pattern is farther from the theory resulting in a reduced noise attenuation.

The noise attenuation is not as efficient for the methanated companion, the attenua-

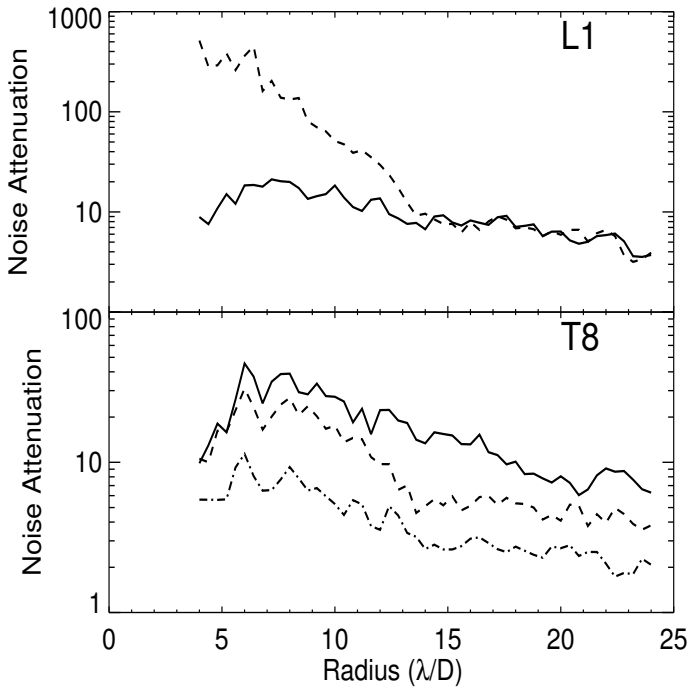

Figure 3.6 Speckle noise attenuation obtained at different radii of the laboratory reconstructed data cube. Results are plotted for the spectral twin algorithm (solid line), the spectral deconvolution (dashed line) and for the simple difference (dot-dash line). The double difference has similar performance as the simple difference; the former is not shown for clarity. The case in which all the data cube slices are collapsed for the search of an L1 companion is shown in the top panel. The collapse of the slices situated between 1.54 and 1.60 μm for the search of a T8 companion is shown in the bottom panel. Note that these curves do not take into account the companion flux that may be subtracted by the algorithms.

tion factor varying from 30 to 5. The performance difference between the two images is likely explained by a more efficient noise averaging at small radii obtained by the collapse of the whole data cube instead of only a few slices after the application of this algorithm. There is no such effect for the case of the spectral twin algorithm for which the attenuation factor is very similar for both types of companions varying between 20 and 8 for a non-methanated companion and between 40 and 8 for a methanated one.

These results would seem to indicate that the spectral deconvolution algorithm is more optimal for searching non-methanated companions while the spectral twin al-

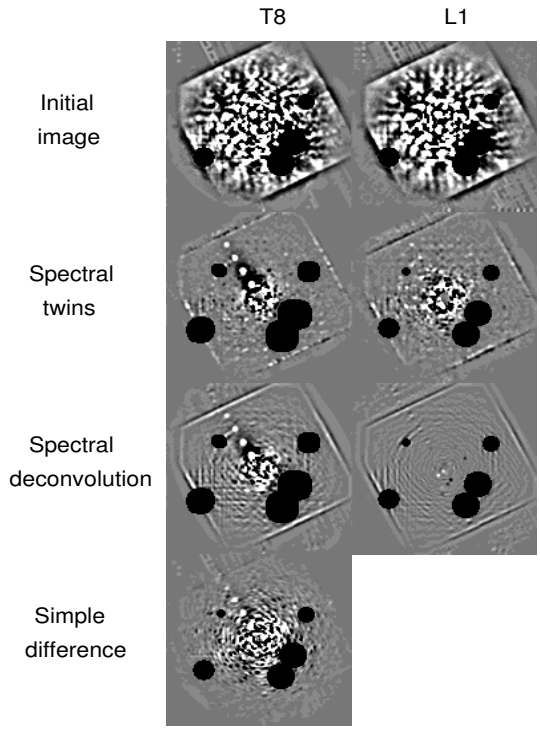

Figure 3.7 Examples of final images constructed for the companion identification for the initial data cube and after the application of the different algorithms. The T8 companions are well seen at the four radii ($5\lambda/D$, 10 λ/D, 15 λ/D and 20 λ/D) at which they were introduced for the three speckle suppression algorithms shown. As stated in the text, a high-pass filter was applied to the images and their radial profile was subtracted. The dark halos around the companions are caused by this high-pass filtering of the image. All images are displayed with the same dynamic range. Ghost images are masked by dark circles.

gorithm, closely followed by the spectral deconvolution, is better suited for detecting methanated ones. However, this conclusion is premature since the impact of these algorithms on the companion signal has yet to be considered.

3.5.2 Signal-to-noise Ratio Performance

The next step is to evaluate the fraction of companion flux subtracted by each algorithm in order to estimate the detection S/N. To do so, fake companions were inserted in the initial data cube. A host star having a monotonic spectrum is mimicked by forcing

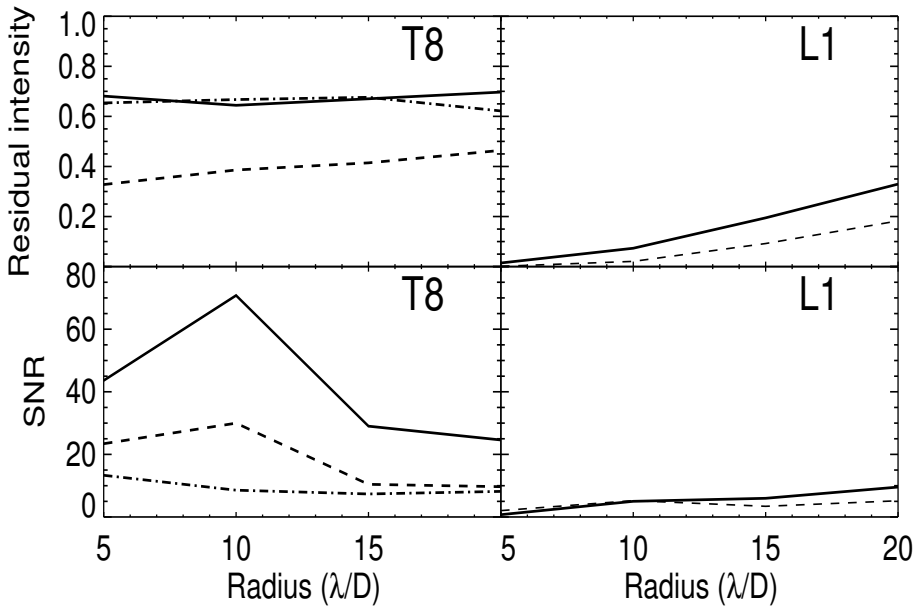

Figure 3.8 Mean companion residual intensity left after the application of various speckle suppression algorithms as a function of radii (top panels) and mean signal-to-noise ratio of the companion vs radii for the laboratory reconstructed data cube (bottom panels). The results obtained for a methanated T8 companion and non-methanated L1 companions are respectively shown in the left and right panels. Results are plotted for the spectral twin algorithm (solid line), the spectral deconvolution (dashed line) and for the simple difference (dot-dash line). The initial S/N of the companion was 5.

the same flux at all wavelengths. The companion PSF is taken to be a non saturated laboratory data cube PSF modulated by the required companion SED which is implanted in the original data cube at radii of 5, 10, 15 and 20 λ/D. The companions brightnesses were set to be at the 5σ level of the speckle noise present at the radius they were introduced. Each speckle suppression algorithm is applied on the cube and the S/N at which the companion is detected is computed. The exercise was repeated 25 times with a different random azimuthal position. Examples of a resulting image for each algorithm are shown in Figure 3.7 and the computed mean residual intensity of the extracted companions along with their mean S/N after the application of a given speckle suppression algorithm are plotted in Figure 3.8.

These figures show that the spectral twin algorithm is as efficient as the SD at re-

covering the signal of a methanated companion, recovering $\sim 70\%$ of its initial flux and they both achieve a better performance than spectral deconvolution. Combined with the speckle noise attenuation factor shown in Figure 3.6, this results in the the best S/N being reached with the use of the spectral twin algorithm. Overall, the S/N was improved by a factor 14 for the spectral twin algorithm i.e. twice the performance of the spectral deconvolution and four times the performance of the SD.

The signal from the methanated companions was also significantly better recovered than the one from the non-methanated companions. This is expected since the contamination of a speckle spectrum by a T8 companion only affects a few slices of the whole spectrum making it a high spectral frequency at any radius. The spectral deconvolution and the spectral twin algorithm are particularly efficient at fitting the speckles spectrum and, hence, at extracting the companion initial intensity. In the case of the non-methanated companions, more signal is recovered as the companion is further away from the PSF center and as it becomes a higher frequency in a speckle spectrum. The best performance at recovering the non-methanated companion signal is still obtained using the spectral twin algorithm. At the largest radius investigated (20 λ/D), 35% of the fake companion flux is recovered. This leads to an improvement of the companion S/N by a factor of 2 which is twice as good as that obtained with the spectral deconvolution. A gain in S/N was only achieved for radii greater than $\sim$ 10 λ/D since the companion flux loss at shorter radii is too important to lead to any S/N gain.

In summary, the spectral twin algorithm leads to the best improvement of the companion S/N for both types of companions. Even though the spectral deconvolution offers better speckle noise attenuation at small radii for the non-methanated companions, it also subtracts significantly more companion flux in that zone making the spectral twin algorithm more efficient.

3.6 Companion Spectrum Recovery

The algorithms described in section 3.4 are useful for the identification of a potential companion. Yet, they have a non-negligible impact on the companion spectrum. To illustrate this point, the extracted spectrum obtained after the application of either the spectral twin or the spectral deconvolution algorithm are depicted in Figure 3.9. The T8 spectrum peak is retrieved with a reasonable accuracy, with the expected reduction in intensity as explained in the previous section. However, the L1 spectrum mean intensity is severely underestimated and, moreover, has a very different shape from the original one. This section presents an iterative algorithm that extracts as accurately as possible both the companion signal and its spectral shape given a known position for the detected companion.

3.6.1 Iterative Algorithm for Spectral Extraction

Consider the ith spaxel spectrum of a rescaled data cube contaminated by the companion signal, $S_i(\lambda)$, as being the sum of a speckle spectrum associated with the host star, $A_i(\lambda)$, and a companion spectrum, $C_i(\lambda)$. The estimated contribution from the star is the spectrum fit, $\tilde{A}_i(\lambda)$, obtained by the use of either the spectral twin or the spectral deconvolution algorithm. We take advantage of the companion position knowledge by masking it out of the fit. Hence, the estimate of the companion flux at a given wavelength, $\tilde{C}_i(\lambda)$, contaminating a spaxel spectrum is simply:

$$\tilde{C}_i(\lambda) = S_i(\lambda) - \tilde{A}_i(\lambda). \tag{3.3}$$

This is done for all spaxels situated in a predefined area affected by the companion flux. An estimate of the companion spectrum can then be obtained by summing the residual flux over this area:

$$\tilde{C}(\lambda) = \sum_i \tilde{C}_i(\lambda). \tag{3.4}$$

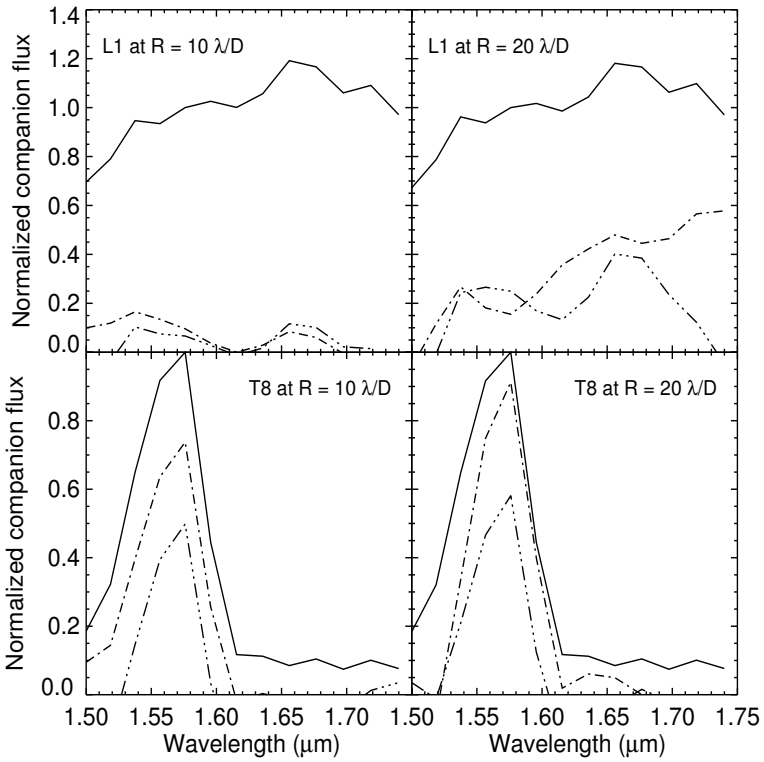

Figure 3.9 Comparison of the extracted spectrum after the use of the spectral twin algorithm (dot-dashed line) and of the spectral deconvolution (triple-dot dashed line) with the spectrum introduced (solid line). This is done for L1 (top two panels) and T8 companions (bottom two panels) at radii of 10 and 20 λ/D.

This first estimate is then subtracted from the data cube. Here, it is assumed that the companion has the same PSF as the star, which is a good approximation given the proximity of the two objects. A data cube of the star PSF is first spectrally normalized to unity. The resulting PSF is shifted to the companion position. The cube is finally rescaled about the star center, as was done for the data cube containing the companion. The result gives the relative contribution of the companion PSF to each spaxel spectrum, $c_i(\lambda)$. The companion contribution to be subtracted from the initial PSF at each wavelength and at each spaxel position is then:

$$\tilde{C}_i(\lambda) = \tilde{C}(\lambda)c_i(\lambda). \tag{3.5}$$

Hence the new spaxel spectrum is:

$$S'_i(\lambda) = S_i(\lambda) - \tilde{C}_i(\lambda). \tag{3.6}$$

This spectrum is then fitted again by the speckle suppression algorithm to find a new value of $\tilde{A}_i(\lambda)$. The process is repeated and the new residual companion flux is added to the previous estimation.

The developed algorithm is similar to the one presented by Thatte et al. (2007) with two main differences. First, no initial estimation on the companion flux is made before the application of the iterative algorithm as the companion brightness is close to the noise level. Second, an unsaturated host star PSF is taken as the reference companion PSF to be subtracted instead of making any assumption on the companion FWHM.

3.6.2 Predicted Performance

We first tested this algorithm on simulated data. Simulations were made to mimic our laboratory data with the same spectral and spatial resolution and the same FOV. The same procedure described earlier is followed to insert fake companions in the image with an L1 spectral type. This type of companion is chosen since its spectrum displayed the largest discrepancy after extraction. The spectral twin algorithm is used to suppress speckle noise. Note, however, that the same iterative process can be used to extract the initial companion spectrum with the spectral deconvolution.

The spectra depicted in Figure 3.10 show that the iterative algorithm is particularly efficient at recovering the initial companion spectra in our simulations. Note also that the use of this iterative algorithm becomes less necessary as the companion is further away from the star as the spectrum is more accurately retrieved by the speckle suppression algorithm alone.

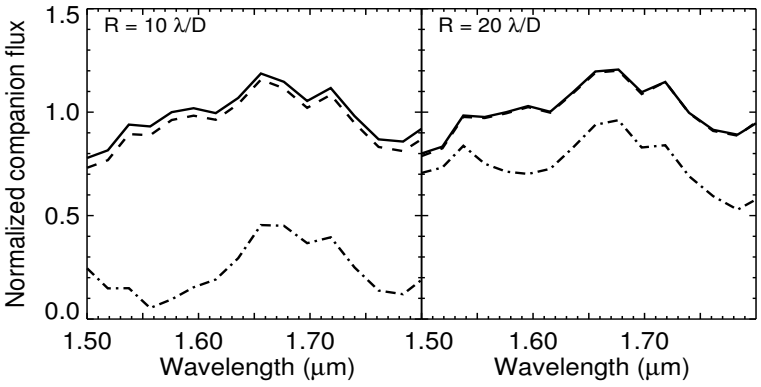

Figure 3.10 Recovered spectra after the application of the iterative extraction algorithm on simulated data for L1 companions at radii of 10 λ/D (left panel) and 20 λ/D (right panel). The solid line is the input companion spectrum added to the data cube, the dot-dashed line is the companion spectrum retrieved after the application of the spectral twin algorithm without the use of the iterative extraction algorithm presented in this section, the dashed line is the spectrum recovered after 2 iterations of the proposed extraction algorithm.

3.6.3 Application to Laboratory Data

The next step was to apply this algorithm to the fake companions inserted in our laboratory data. Results are shown in Figure 3.11. The initial companion flux was retrieved with an accuracy of $\sim 20\%$ on average. The overall spectral shape error was computed by normalizing to unity both the original companion spectrum and the one extracted. The spectral shape was retrieved with a mean precision of $\sim 5\%$.

It was found that the differences between simulations and laboratory data came from the larger spectral diversity available in real data due to data cube reconstruction errors. This leads to the possible use of more spectral shapes to fit the underlying speckle structure making the selection of the right one difficult and, hence, resulting in a less accurate spectrum extraction.

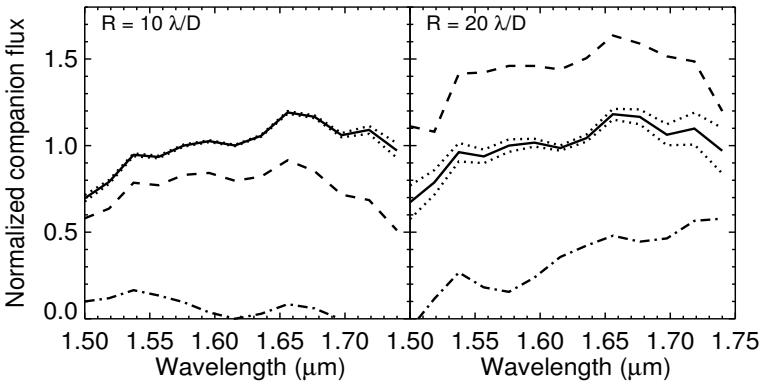

Figure 3.11 Same as Figure 3.11 but for our laboratory data. The dotted line represents the 1σ noise level in the image obtained after the application of the spectral twin algorithm. The iterative algorithm converged to this solution after 10 iterations.

3.7 Conclusions

An IFS optimized for high-contrast imaging has been designed, built and tested in the laboratory. Its capability to image faint companions was evaluated by applying different algorithms to the reconstructed data cube. The SD applied to IFS data was found to be at least as good as with an MCC camera with a speckle noise varying from 10 to 2 depending on the companion separation but is still not reaching its theoretical limit due to errors intrinsic to the IFS and to the data cube reconstruction.

Fake companions were added in the data cube to test the capacity of the different speckle noise attenuation algorithms to identify faint methanated and non-methanated companions. All algorithms are more efficient at detecting methanated companions due to their sharp spectral feature. The spectral twin algorithm was found to be the most efficient at detecting both types of companions by increasing the S/N of a methanated companion by a factor ~ 14 and by a factor ~ 2 for a non-methanated companion at their best. This efficiency comes from its relatively large noise attenuation performance combined with its capacity to fit more accurately the speckle underlying structure.

Iterative companion extraction algorithm allowing the extraction of the original companion flux with a mean error of 20% while te relative spectral shape is retrieved with a

mean error of 5% was finally presented.

References

Antichi, J., Dohlen, K., Gratton, R. G., Meda, D., Claudi, R. U., Giro, E., Boccaletti, A., Mouillet, D., Puget, P., & Beuzit, J.-L., 2009, Astrophys. J. , 695, 1042

Bacon, R., et al., 1995, A&AS, 113, 347

Béjar, V. J. S., Zapatero Osorio, MR., Pérez-Garrido, A., Álvarez, C., Martín, E. L., Rebolo, R., Villó-Pérez, I. & Díaz-Sánchez, A., 2008, ApJ, 673, L185

Berton, A., Gratton, R. G., Feldt, M., Henning, T., Desidera, S., Turatto, M., Schmid, H. M. & Waters, R., 2006, PASP, 118, 1144

Biller, B. A., Close, L., Lenzen, R., Brandner, W., McCarthy, D. W., Nielsen,E., & Hartung, M. 2004, Proc. SPIE, 5490, 389

Biller, B. A., Kasper, M., Close, L.M., Brandner, W. & Kellner S., 2006, ApJ, 641, L141

Biller, B. A., et al., 2007, Astrophys. J. , 173, 143

Chauvin, G., Lagrange, A.-M., Dumas, C., Zuckerman, B., Mouillet, D. & Song, I., Beuzit, J.-L., & Lowrance, P., 2004, A&A, 425, L29

Chauvin, G., Lagrange, A.-M., Zuckerman, B., Dumas, C., Mouiller, D., Song, I., Beuzit, J.-L., Lowrance, P. & Bessell, M. S., 2005, A&A, 438, L29

Dohlen, K. et al., 2006, Proc. SPIE, 6269, 62690Q

Janson, M., Brandner, W. & Henning, T., 2008, A&A, 478, 597

Kalas, P., Graham, J. R., Chiang, E., Fitzgerald, M. P., Clampin, M., Kite, E. S., Stapelfeldt, K., Marois, C., & Krist, J., 2008, Science, 322, 5906, 1345.

Lafrenière, D. et al., 2007, Astrophys. J. , 670, 1367

Lafrenière, D., Jayawardhana, R., & van Kerkwijk, M. H., 2008, ApJ, 689, L153

Lagrange, A.-M., Gratadour, D., Chauvin, G., Fusco, T., Ehrenreich, D., Mouillet, D., Rousset, G., Rouan, D., Allard, F., Gendron, É., Charton, J., Mugnier, L., Rabou, P., Montri, J., & Lacombe, F., 2009, A&A Letters, 493, L21

Lavigne, J.-F., Doyon, R., Thibault, S. & Lafrenière, D., 2006a, Proc. SPIE, 6269, 62693X

Lavigne, J.-F., Doyon, R., Thibault, S. & Wang, M., 2006b, Proc. SPIE, 6342, 63421M

Lavigne, J.-F., Doyon, R., Lafrenière, D., Marois, C., & Barman, T., 2009, Astrophys. J. , submitted

Lenzen, R., Close, L., Brandner, W., Biller, B., & Hartung, M., 2004, Proc. SPIE, 5492, 970

Macintosh, B., et al., 2006, Proc. SPIE, 6272, 62720L

Marcy, G., Butler, R. P., Fischer, D., Vogt, S., Wright, J. T., Tinney, C. G., & Jones, H. R. A. 2005, Prog. Theor. Phys. Suppl., 158, 24.

Marois, C., Doyon, R., Racine, R. & Nadeau, D., 2000, PASP,112, 91

Marois, C., Doyon, R., Nadeau, D., Racine, R., Riopel, M., Vallée, P., & Lafrenière, D. 2005, PASP, 117, 745

Marois, C., Lafrenière, D., Macintosh, B. & Doyon, R., 2008, Astrophys. J. , 673, 647

Masciadri, E., Mundt, R., Henning, T., Alvarez, C., & Barrado y Navascués, D. 2005, Astrophys. J. , 625, 1004

McElwain, M. W., Metchev, S. A., Larkin, J. E., Barczys, M., Iserlohe, C., Krabbe, A., Quirrenbach, A., Weiss, J., & Wright, S. A., 2007, Astrophys. J. , 656, 505

Neuhäuser, R., Guenther, E. W., Wuchterl, G., Mugrauer, M., Bedalov, A., & Hauschildt, P. H., 2005, A&A, 435, L13

Nielsen, E. L., Close, L. M., Biller, B. A., Masciadri, E., & Lenzen, R., 2008, Astrophys. J. , 674, 466

Racine, R., Walker, G. A. H., Nadeau, D., Doyon, R., & Marois, C. 1999, PASP, 111, 587

Rosenthal, E. D., Gurwell, M. A. & Ho, P. T. P., 1996, Nature, 384, 243

Schneider, G., & Silverstone, M. D. 2003, Proc. SPIE, 4860, 1

Seifhart, A., Neuhäuser, R. & Hauschildt, P.H., 2007, A&A, 463, 309

Smith, W. H., 1987, PASP, 99, 1344

Sparks, W. B., & Ford, H. C., 2002, Astrophys. J. , 578, 543

Thatte, N., Abuter, R., Tecza, M., Nielsen, E. L., Clarke, F. J. & Close, L. M., 2007, MNRAS, 378, 1229

CHAPITRE 4

CONTRÔLE D'UN DUO DE MIROIRS DÉFORMABLES DANS UN SYSTÈME D'OPTIQUE ADAPTATIVE UTILISANT UN RECONSTRUCTEUR DE FOURIER

WOOFER - TWEETER CONTROL IN AN ADAPTIVE OPTICS SYSTEM USING A FOURIER RECONSTRUCTOR

JEAN-FRANÇOIS LAVIGNE[abc] AND JEAN-PIERRE VÉRAN[b]

Published in: *Journal of the Optical Society of America A (JOSA A)*, v.25, p.2271 (2008)

Abstract

Future adaptive optics systems seeking a higher degree of correction may need to split the command between two deformable mirrors (DMs), the woofer and the tweeter. We first present a method to specify the order of correction of the woofer DM for a given tweeter stroke requirement using an analytical and Monte-Carlo approach. We then develop a computationally efficient algorithm to split the command between the two DMs in the case where a Fourier reconstructor is used. We find that the computational efficiency can be dramatically improved by splitting the command in the Fourier space and by sending to the woofer only the modes it can reproduce accurately.

[a]Département de physique, Université de Montréal, C.P. 6128, succ. centre-ville, Montréal, QC, Canada

[b]Herzberg Institute of Astrophysics, 5071 West Saanich Road, Victoria, BC, Canada

[c]Institut national d'optique, Parc technologique du Québec métropolitain, 2740 rue Einstein, Québec, QC, Canada

4.1 Introduction

State-of-the-art astronomical adaptive optics (AO) systems currently installed on 8 m class telescopes are equipped with deformable mirrors (DMs) with up to 20 actuators. However, future AO systems—currently in the design phase—will require significantly more actuators, because they try to achieve a higher degree of correction than before, and/or because they are conceived for the next generation of giant telescopes (30-50m). For example, the Gemini Planet Imager (GPI) (Macintosh et al., 2006) requires 45×45 actuators to enable high contrast imaging on the 8 m Gemini telescope, and the narrow field infrared AO System (NFIRAOS)—the facility AO system for the future Thirty Meter Telescope (Herriot et al., 2006)—may require a DM with up to 120×120 actuators. These systems also require a higher actuator stroke (up to 10 μm), and high temporal response (1 kHz or more). Furthermore, they must impose strict limits on the physical size of their pupils, and thus on the DM actuator pitch, so that the optical elements in the AO train and the benches that support them do not become prohibitively large.

Designing a high actuator count, small pitch, high stroke, fast DM at a reasonable cost turns out to be, in many cases, an impossible challenge, and compromises have to be reached. One such compromise is to provide the AO correction with two DMs, installed in series in the optical train, typically one DM with high stroke but low actuator density (called the woofer) and one DM with high actuator density but low stroke (called the tweeter, borrowing terms from the physics of sound reproduction) (Hampton et al., 2006; Hu et al., 2006; Brennan et al., 2006). Such a woofer-tweeter architecture is expected to be particularly efficient in correcting for atmospheric turbulence, where most of the power is at low spatial frequencies and thus can be corrected by the high-stroke woofer DM. For example in GPI, the baseline architecture is to use a compact (0.4 mm pitch), 45×45-actuator, microelectromechanical system (MEMS) continuous phase sheet DM (Cornelissen et al., 2006) as the tweeter. Because this device is unable to achieve the ~ 10 μm stroke required for full correction (Evans et al., 2005; Morzinski et al., 2006),

it is complemented by a conventional high stroke 9×9 piezostack DM (5 mm pitch) woofer.

To enable such a woofer-tweeter architecture, two problems need to be solved: First, the woofer needs to be suitably specified in terms of actuator number and stroke so that these numbers can be minimized—and the cost in turn—while maintaining a suitable saturation margin (for both the woofer and the tweeter). Second, the algorithm for splitting the correction between the woofer and the tweeter needs to be optimized so that the risk of saturation is minimized while maintaining a reasonable computational complexity.

This paper addresses these two problems in detail. The derivations apply specifically to the case of GPI, but many insights they provide could be applied to other systems. In section 2, we find the relationship between the woofer actuator count and the stroke required on the tweeter to achieve a given saturation margin. The problem is analyzed in terms of actuator stroke and in terms of inter-actuator stroke, which are both critical. We use two different methods: The first is analytical and enables a quick exploration of a large number of different parameters; the second is based on Monte Carlo simulation, and allows us to include more details such as a realistic influence function for the woofer, and attain higher-fidelity results. In section 3, we present an algorithm to split the correction that is much more efficient than the brute force projection method because it takes advantage of the efficient wavefront reconstructor used in GPI, the Fourier Transform Reconstructor (FTR). Section 4 concludes this work.

4.2 Determination of the woofer parameters

In this section, we study the relationship between the woofer actuator count, the actuator stroke (AS) and the interactuator stroke (IAS) required at the tweeter to insure a given saturation margin (SM). The SM is defined as the ratio between the half AS (respectively, the IAS) and the root-mean-square (rms) wavefront on the tweeter at that

actuator (respectively, the rms phase difference between that actuator and its nearest neighbors). Hence if an actuator has a stroke of 10 μm, that is ± 5 μm, and the rms wavefront at that actuator is 1 μm, we say that the SM is 5σ. We consider that all the actuators have the same stroke, and always consider the SM at the actuator where the wavefront rms is the highest (worst case). In GPI, we require an SM of 5σ for both the AS and the IAS. This conservative value is justified by the fact that saturation is very detrimental to high-contrast imaging, since saturated actuators will produce a lot of scattered light. Clearly, the higher the actuator count on the woofer, the more turbulence it can accept, and, for a given SM, the lower the demand on AS and IAS. However, making the woofer excessively high order is both expensive and impractical, so the relationship between woofer actuator count and tweeter stroke must be carefully studied.

4.2.1 Analytical approach

We first make the simplistic assumption that the woofer acts as an ideal low-pass spatial filter, able to perfectly correct the turbulence up to a cut-off spatial frequency set by the actuator density, and has no effect on spatial frequencies beyond the cut-off, which have to be corrected by the tweeter. The atmospheric turbulence is assumed to follow the classical von Karman model, with parameters r_0 (coherence length) and L_0 (outer scale). This model states that the turbulent phase is spatially stationary, and that its Power Spectrum Density (PSD) is the same at all positions in space. However, once it is corrected for tip, tilt and piston over the telescope pupil, the phase is no longer stationary, and its statistics vary across the telescope pupil. The two-sided piston and tip/tilt removed PSD at coordinates $\vec{r} = [r_1, r_2]$ normalized to the pupil radius, is derived in appendix A and is given by:

$$
\begin{aligned}
PSD(\vec{\kappa},\vec{r}) &= 0.023D^2\left(\frac{D}{r_0}\right)^{5/3}\left[\kappa^2+\left(\frac{D}{L_0}\right)^2\right]^{-11/6} \\
&\times\left|1-\left[\frac{2J_1(\pi\kappa)}{\pi\kappa}+4i\left(r_1\cos\theta+r_2\sin\theta\right)\frac{2J_2(\pi\kappa)}{\pi\kappa}\right]\right. \\
&\left.\times\exp\left(-\pi i\vec{\kappa}\cdot\vec{r}\right)\right|^2 \qquad (4.1)
\end{aligned}
$$

where $\vec{\kappa}=[\kappa_1,\kappa_2]=|\vec{\kappa}|\,[\cos\theta,\sin\theta]$ is the spatial frequency normalized with respect to the pupil diameter; D is the telescope diameter; $i=(-1)^{1/2}$; and J is the Bessel function of the first kind.

Since we are using spatial frequencies normalized to the pupil diameter, the woofer cut-off frequency is: $\kappa_c = D/2p$ where p is the inter-actuator spacing, or pitch. The phase variance at a point on the woofer (woofer phase) can be obtained by integrating Eq. 4.1 over the domain defined by $|\kappa_1|<\kappa_c$ and $|\kappa_2|<\kappa_c$. The variance of the residual phase to be corrected by the tweeter (tweeter phase) is found by integrating over the complementary domain. The AS can be derived as explained previously by searching for the location where the phase variance is the highest. This is found to be at the edge of the pupil, for both the woofer and the tweeter.

The same analytical approach can be used to derive the IAS. The PSD of the phase difference between two points separated by a distance d in the pupil is also derived in appendix A and is given by:

$$
\begin{aligned}
PSD(\vec{\kappa},\vec{r}) &= 0.023D^2\left(\frac{D}{r_0}\right)^{5/3}\left[\kappa^2+\left(\frac{D}{L_0}\right)^2\right]^{-11/6} \\
&\times\left|2i\pi\frac{d}{D}\kappa_1\,\mathrm{sinc}\left(\pi\frac{d}{D}\kappa_1\right)\mathrm{sinc}\left(\pi\frac{d}{D}\kappa_2\right)\right. \\
&\left.-4id\cos\theta\,\frac{2J_2(\pi\kappa)}{\pi\kappa}\exp(-i\pi\vec{\kappa}\cdot\vec{r})\right|^2. \qquad (4.2)
\end{aligned}
$$

For simplicity, without any loss of generality, the two points are assumed to form a vector

parallel to the x axis. The same steps as with the stroke computation are used to get the interactuator variance for the woofer and tweeter, leading to the IAS. However, note that both DMs have a different PSD in this case due to their different actuator pitch d in Eq. 4.2.

4.2.2 Monte Carlo simulations

We use a Monte Carlo approach to implement a higher fidelity model of the woofer, one that takes into account the actual influence functions of the woofer (i.e. the actual DM surface deformation when one actuator is poked), as opposed to the simplistic ideal low pass filter used in the analytical approach above. Several realizations of the atmospheric turbulence are simulated with a set of phase screens with the proper von Karman statistics on a square grid with N points. For each generated phase screen, the piston, tip and tilt are first evaluated on the pupil and removed from the whole phase screen. A tapering function is used to weight the phase outside the pupil with a linear decrease ranging from unity on the pupil edge to a null value farther out to avoid any unrealistic edge effects. The resulting phase screen Φ is then projected onto the set of n_{woof} woofer influence functions, using the following equation:

$$\vec{c}_{woof} = W^{-1}\Phi. \tag{4.3}$$

where W is an $N \times n_{woof}$ matrix that has in its columns the influence functions of the woofer actuators. The resulting coefficients $\vec{c}_{woof}$ are the commands to the woofer actuators that best fit Φ, in the least-square sense. The actual phase created on the woofer is given by

$$\Phi_{woof} = W\vec{c}_{woof}, \tag{4.4}$$

The residual phase to be corrected by the tweeter is:

$$\Phi_{tw} = \Phi - \Phi_{woof}. \tag{4.5}$$

As in the analytical approach, we find the woofer AS (respectively, the tweeter AS) by searching for the point of maximum phase variance on Φ_{woof} (respectively, Φ_{tw}), across all the different realizations of the turbulent phase.

For the woofer, the search for the point of maximum variance is restricted to the location of actuators that would be actively controlled. In our case, we assume that the woofer is associated with a wavefront sensor (WFS) in the Fried geometry, which means that the actuators are registered to the corners of the WFS square subapertures. We consider that an actuator is actively controlled if it lies at the corner of at least one subaperture that is at least 50% illuminated by the telescope pupil. These actively controlled actuators cannot be any farther than one actuator pitch from the edge of the telescope pupil. The precise definition of which actuator is actively controlled, and which actuator is not is important because the highest actuator excursions always occur at the edge of the pupil.

For the tweeter, the search for the point of maximum variance is restricted to the location of actuators inside the telescope pupil after Φ_{tw} is resampled to a nominal grid. This resampling is required because when we try to compare woofers with different numbers of actuators, we find that it is critical to maintain a constant resolution for the influence function, that is there always has to be the same number of pixels in the simulation grid in each woofer actuator pitch. Therefore the size of the simulation grid must be set based on the woofer, and thus must be resampled to match the tweeter actuator geometry.

A similar analysis is done to find the woofer and tweeter IAS.

4.2.3 Results

In this subsection, we report on the results obtained with both the analytical and the Monte Carlo approaches using for the atmospheric parameters a Fried parameter r_0 of 0.15 m and an outer scale L_0 of 100 m. For the woofer influence function, we use an analytical fit to the influence function of the piezostack DM used in Altair (Herriot et al., 1998), which exhibits a mechanical coupling between neighboring actuators of $\sim 10\%$.

For our statistical analysis in the Monte Carlo case, we use 1000 randomly generated phase screens. The ASs and IASs are computed for different woofer actuator counts, and are shown in Figures 4.1 and 4.2, respectively. Only the values of woofer actuator count considered in the context of GPI were investigated in the Monte Carlo simulations.

As the woofer actuator count increases, the woofer can take on more and more spatial frequencies: The tweeter stroke decreases and the woofer stroke increases, as expected. The exponential behavior is essentially related to the exponential nature of the atmospheric spatial PSD. For the woofer stroke, the analytical and Monte Carlo results match very well: Because of the exponential nature of the atmospheric turbulence PSD, the woofer stroke is dominated by the low spatial frequencies, e.g. defocus. For the tweeter stroke, the Monte Carlo results are higher than the analytical results. This is explained by the fact that the realistic influence function does not quite act as an ideal filter, as assumed by the analytical model: The transition at the cut-off frequency $\kappa_c = D/2p$ is not sharp, and thus some spatial frequencies below κ_c make it to the tweeter. These "leaked" low spatial frequencies significantly increase the tweeter stroke, again because of the exponential nature of the atmospheric turbulence PSD.

As the woofer actuator count increases, there is less to correct on the tweeter. Therefore, the tweeter interactuator stroke also decreases, as expected. However, in contrast to the woofer stroke, the woofer interactuator stroke decreases. This can be surprising at first, since there is more on the woofer to correct. However, increasing the woofer actuator counts means reducing the woofer actuator pitch. Since the woofer correction is dominated by the lowest spatial frequencies, it is natural to find that the difference between two adjacent actuators decreases as they get closer.

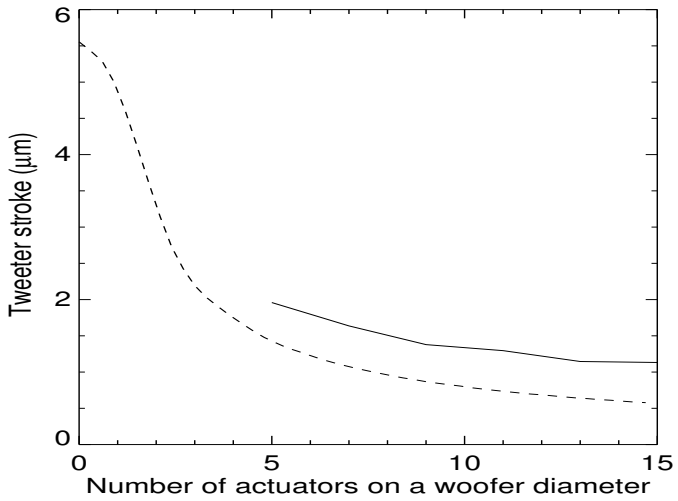

(a)

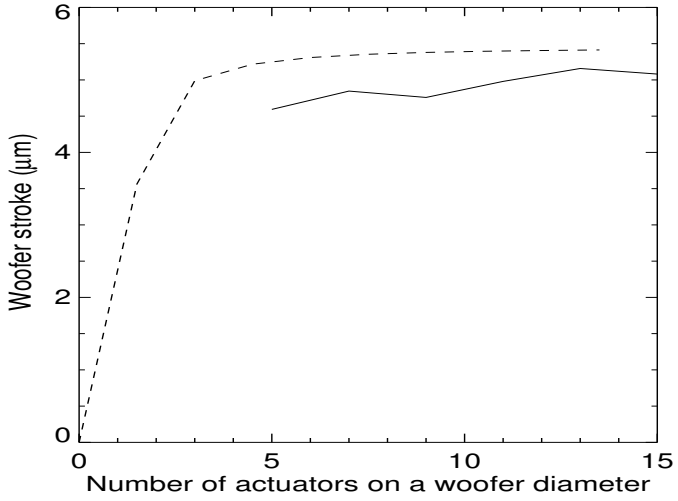

(b)

Figure 4.1 Stroke for different number of actuators on a woofer diameter. The Monte Carlo simulations results are plotted as a solid curve. The analytical results for an actuator on the pupil edge are plotted as a dashed curve. The DM strokes are plotted in (a) for the tweeter and in (b) for the woofer.

4.3 DMs Control with a Fourier reconstructor

4.3.1 Proposed algorithm

The traditional way to control an AO system is to run the WFS measurements through a wavefront reconstructor to get an estimate of the residual wavefront error in DM ac-

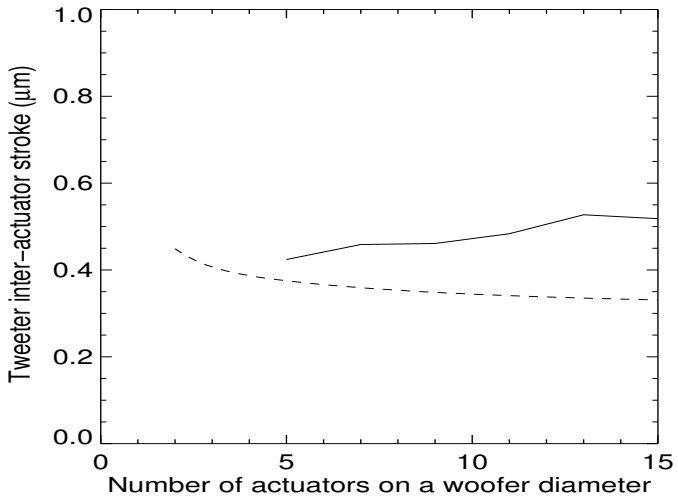

(a)

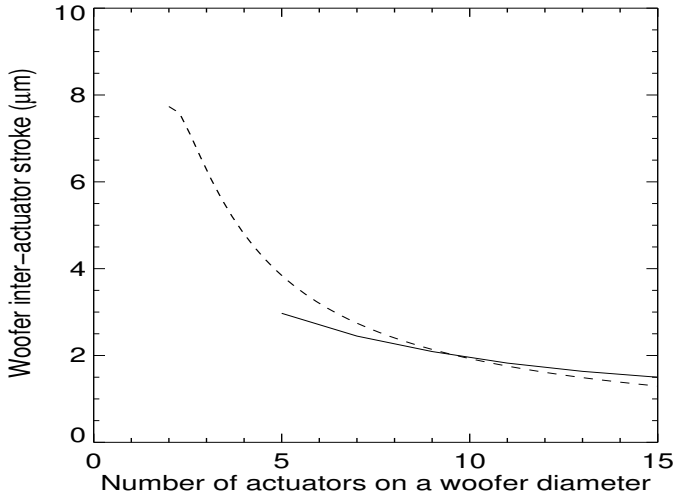

(b)

Figure 4.2 Interactuator stroke for different number of actuators on a woofer diameter. The Monte Carlo simulations results are plotted as a solid curve and the analytical results are plotted as a dashed curve. The DM interactuator strokes are plotted in (a) for the tweeter and in (b) for the woofer.

tuator space, which is in turn run through a temporal controller (usually an integrator), to find the commands to be sent to the DM. In the case where the DM consists of a woofer and a tweeter, the full correction is first reconstructed on the tweeter actuator

space, and then split between the n_{woof} woofer actuators and the n_{tw} tweeter actuators. The most basic way to do such a split is what we call the "brute force projection". It entails two matrix-vector multiplies (VMMs), one that projects from the tweeter actuator basis onto the woofer actuator basis ($n_{tw} \times n_{woof}$ matrix by a n_{tw} vector) and one that projects from the woofer actuator basis back onto the tweeter actuator basis ($n_{woof} \times n_{tw}$ matrix by a n_{woof} vector), as depicted in Figure 4.3. This can be reduced to one VMM if an offload scheme is adopted, as proposed in Brennan et al. (2006). In this case, as opposed to a pure splitting, the full correction is applied to the tweeter, but the low temporal frequencies of the woofer modes are offloaded to the woofer through a VMM and proper temporal filtering. This approach requires the bandwidth of the woofer and of the tweeter to be chosen carefully to avoid stability problems, but can achieve a better rejection of the low temporal frequencies of the woofer modes, because the signal going to the woofer is integrated twice. However, this is done at the cost of an increased tweeter stroke, because the tweeter needs to correct for the high temporal frequencies of the woofer modes. In the remaining of the paper, we only consider splitting, where all the woofer modes are applied to the woofer, so that the tweeter stroke is minimized.

When n_{tw} is large, such as in the case of GPI ($n_{tw} \sim 1600$), the VMMs can be a very large computational burden, even when n_{woof} is moderate (for GPI, $n_{woof} = 69$). In a traditional AO system, the largest computational burden is usually carried by the wavefront reconstructors, and for large actuator count systems, a lot of efforts have been invested toward making these wavefront reconstructors much more efficient than the traditional approach of having a VMM involving a $n_{tw} \times n_{wfs}$ matrix and a n_{wfs} vector, where n_{wfs} is the number of WFS measurements, typically $2 \times n_{tw}$. GPI, for example, implements the so-called Fourier Transform Reconstructor (FTR) (Poyneer et al., 2002; Poyneer & Véran, 2005), where the VMM is basically replaced by a pair of Fourier transforms; this dramatically reduces the computational load. It follows that for such a system, the brute force projection method would in fact dominate the computational budget, and is therefore not really acceptable.

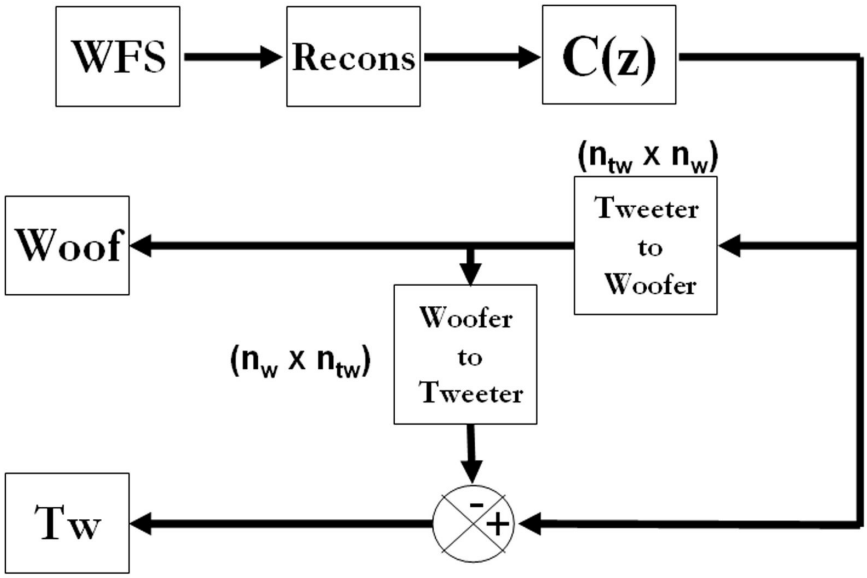

Figure 4.3 Command split in the tweeter command space. Two matrix multiplications are needed to project the tweeter commands in the woofer space and to subtract to woofer correction from the tweeter commands. C(z) represents the controller transfer function.

The GPI FTR scheme involves the following operations: The WFS measurements are processed and run through a Fast Fourier Transform (FFT) and the wavefront error coefficients are reconstructed in Fourier space. Then the temporal controller is applied to obtain the Fourier coefficients of the new DM correction required. Finally, an inverse Fourier transform is applied to obtain the commands to be applied to the tweeter for full correction. The woofer-tweeter split could be implemented at this point using the VMM projection method described above. However, since the woofer principally reproduces the low spatial frequencies of the wavefront, and since the Fourier coefficients of the required DM correction are available as part of the FTR process, our intuition is that the split would be more efficiently performed in Fourier space. Our proposed algorithm is outlined in Figure 4.4.

We start from the output of the temporal controller that contains the Fourier coefficient of the new required DM correction $\vec{m}$. We decide on the number of Fourier modes l that we want to offload to the woofer and extract the l first elements of vector $\vec{m}$ to form

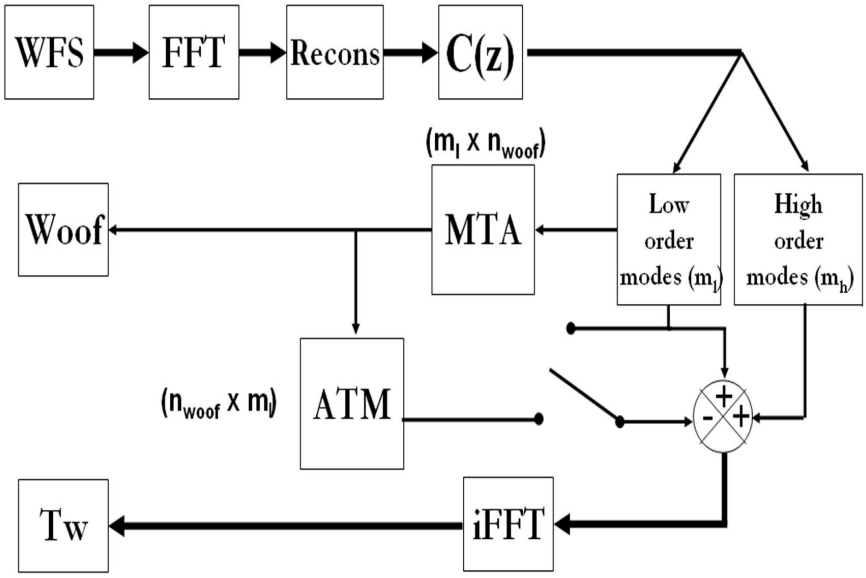

Figure 4.4 Command split in the Fourier domain. The modal coefficient vector is split between a vector of low-order modes $\vec{m}_l$ and a vector of high-order modes, $\vec{m}_h$. If the woofer fits accurately the low-order modes sent to it, those modes coefficients are nulled in the vector sent to the tweeter by using the high switch position. In the other case, the woofer correction cannot be considered as perfect and an ATM matrix has to be used to subtract its correction from the modal coefficients sent to the tweeter. This corresponds to the low switch position. C(z) represents the controller transfer function.

vector $\vec{m}_l$. We then zero the l first elements of vector $\vec{m}$ to obtain vector $\vec{m}_h$. The idea is to send $\vec{m}_l$ to the woofer and $\vec{m}_h$ to the tweeter. We compute the woofer commands $\vec{c}_{woof}$ by a simple VMM:

$$\vec{c}_{woof} = \text{MTA} \cdot \vec{m}_l. \tag{4.6}$$

Here the MTA is the Fourier modes to woofer actuators matrix, which is obtained by projecting each of the l first Fourier modes onto the woofer influence functions. It is an $n_{woof} \times l$ matrix, and since typically n_{woof} is small and $l < n_{woof}$, this VMM is not very computationally intensive.

Assuming that the woofer can indeed reproduce those modes, the command to the

tweeter is obtained by taking the inverse Fourier transform of $\vec{m}_h$:

$$\vec{c}_{tw} = \mathscr{F}^{-1}\left(\vec{m}_h\right). \tag{4.7}$$

This computation corresponds to the switch high position in Figure 4.4. It does not involve any more operations than with no woofer splitting, since in that case, Eq. 4.7 is simply applied to $\vec{m}$. A real DM, however, will not be able to produce perfectly the first l Fourier modes. When this fitting error is too large, it can be sent to the tweeter by implementing the following equation to compute the tweeter commands:

$$\vec{c}_{tw} = \mathscr{F}^{-1}\left(\vec{m} - \mathrm{ATM}\cdot\vec{c}_{woof}\right). \tag{4.8}$$

This computation corresponds to the switch low position in Figure 4.4. ATM is the woofer actuators to Fourier modes matrix, which is obtained by projecting each woofer influence function onto the set of Fourier modes. ATM has only n_{woof} columns, but it has potentially as many rows as the total number of Fourier modes n, which is roughly the number of tweeter actuators. Therefore, the VMM by ATM in Eq. 4.8 is potentially computationally expensive. In a real system, the use of the ATM matrix is also problematic, because unaccounted registration errors between the woofer and the tweeter, and between the tweeter and the WFS, could lead to large residual errors. In the following, we will only focus on cases where the fitting error is small and the use of ATM is not required.

4.3.2 Simulations

In this subsection, we assess our proposed algorithm in the case of GPI, which has a 69-actuator (9×9) woofer and a 1600-actuator (45×45) tweeter, the actuator count being based on the number of actuators provided on the DMs, which is roughly the number of actuators situated on the circular pupil. The influence function for the woofer

is the same as used previously in Subsection 4.2.3. We first try to evaluate qualitatively the modes that are well reproduced by the woofer and for which the use of the ATM matrix is unnecessary. To do that, we compute:

$$MTM = MTA * ATM. \tag{4.9}$$

The magnitude of the diagonal of MTM tells us how well a given Fourier mode is reproduced by the woofer, and when the value of the diagonal term is not 1, the non-diagonal terms give us the decomposition of the fitting error onto the Fourier mode basis. The portion of MTM corresponding to Fourier modes of order ≤ 6 is shown in Figure 4.5. We can see that modes 0 to 44, which correspond to modes of order < 4, are fairly well reproduced by the woofer, whereas higher-order modes are associated with a significant fitting error. Therefore we choose to offload only those 45 first Fourier modes ($l = 44$).

Yet, the fit of the 45 first Fourier modes is not perfect, and so we need to assess the effect of the fitting error on those modes. Our intuition is that this effect must be small, because by the closed-loop nature of the AO system, the fitting error at one frame will be seen by the WFS on the next frame, and the system will be able to correct this error, albeit with a delay. In order to verify this we need to use our Monte Carlo simulation in closed loop. We use the same atmospheric parameters as before ($r_0 = 0.15$ m, $L_0 = 100$ m), but now add the constraint that the turbulence is translating above the telescope at a speed of 20 m/s, which is a fairly pessimistic assumption for most observatory sites. We also assume a 1 kHz frame rate for the AO system and perfect sensing of the Fourier modes by the WFS, so that we do not have to implement the WFS-to-Fourier mode reconstruction. Our analysis involves simulating 200 independent phase screens with von Karman statistics and, for each screen, applying the method described by Assémat et al. (2004) to translate them between AO frames at the desired wind speed. For each screen, we let the loop converge for 10 iterations and assess DM actuator statistics and residual error after the tenth iteration before moving on to the next phase screen. This approach

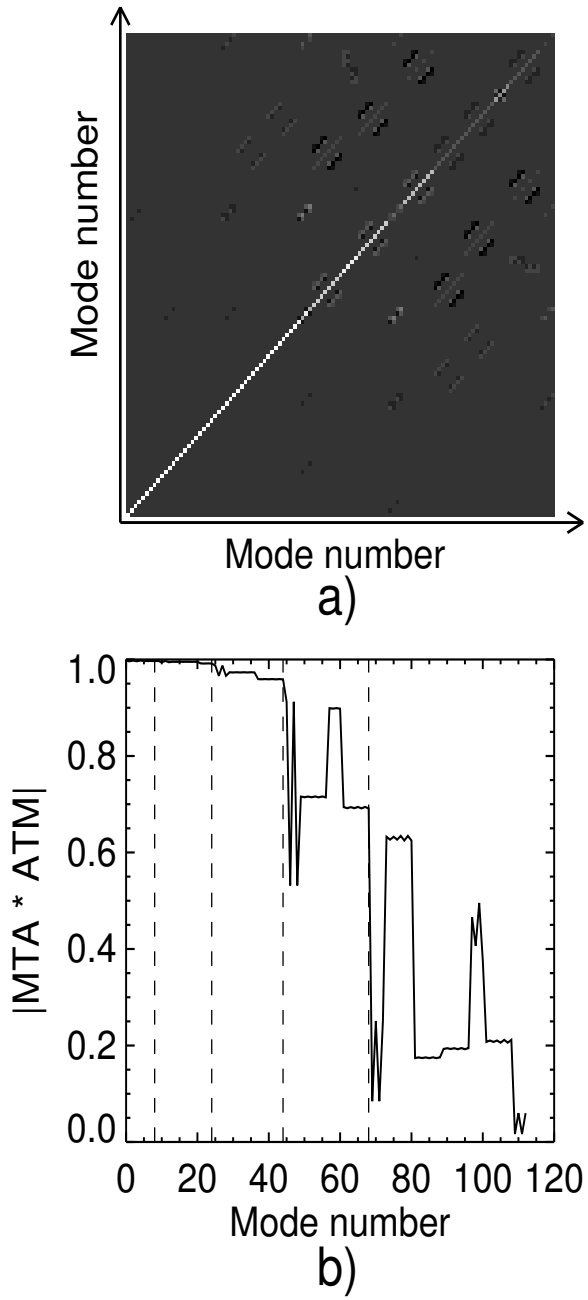

Figure 4.5 (a) Result of the matrix multiplication MTA*ATM. The diagonal represents how accurately the woofer reproduces a mode sent to it. The nondiagonal cells represent the parasite modes being excited by the correction of a given mode. (b) Plot of the matrix diagonal shown in (a). The dashed vertical lines delimit modes of order < 2, < 3, < 4 and < 5.

Table 4.1. Command Split Simulation Results

Split Method	Projection	Fourier	Fourier	Fourier	Fourier
Modes used in MTA	No MTA	All modes	45 modes	45 modes	45 modes
Modes used in ATM	No ATM	All modes	No modes	No modes	No modes
Open/Closed-loop	Open-loop	Open-loop	Open-loop	Closed-loop	Closed-loop
L_0, m	100	100	100	100	30
Woofer Stroke, μm	4.70	4.70	4.58	4.89	4.38
Tweeter Stroke, μm	1.40	1.40	2.03	2.10	1.99
Residual phase rms, nm	$\ll 1$	$\ll 1$	45	1	1
Woofer Interactuator Stroke, μm	2.06	2.06	1.76	1.93	1.81
Tweeter Interactuator Stroke, μm	0.40	0.40	0.60	0.57	0.54

of using many independent phase screens is superior to the traditional method of generating a single long phase screen that is translated at the wind speed, since many more iterations are required in order to beat down the natural correlation of the turbulence and obtain statistically meaningful results. In these tests, our reference to assess the effect of the error due to the imperfect woofer-tweeter split is the ideal case where we assume no woofer and a tweeter with as much stroke as we need.

4.3.3 Results and discussion

Different simulations of the closed loop and of the turbulence outer scale have been conducted to bring out the impact of the Fourier domain command split on the residual errors and DM stroke. The results are shown in Table 4.1. The first column corresponds to the results presented in Section 2. The Fourier domain command split was then implemented. It can be seen that sending all the modes to the woofer and using an ATM matrix for all the tweeter modes is equivalent to the phase projection split used in Section 2. In both cases, the woofer compensates the maximal turbulence it can fit. This control scheme is very computationally expensive due to the dimensions of the MTA and ATM matrices.

The next step was to simulate the impact of sending only the modes well reproduced by the woofer to reduce the size of the MTA matrix. This reduces considerably the

computations required to split the command. The two matrices of 1600×69 elements in Figure 4.3 are replaced by one matrix with 45×69 elements, where the woofer and tweeter are taken to have, respectively, 69 and 1600 actuators. These results are shown in the third column of Table 4.1 for an open-loop simulation and in the fourth column for the closed-loop case. It can be seen that the tweeter stroke significantly increases in this case. This is expected since the tweeter now has to correct the modes that are no longer compensated for by the woofer. Also, closing the loop allows the correction of residual errors present after open-loop correction which results in a slight increase of both DM strokes. The last column is similar to the fourth but for an L_0 of 30 m. This gives an idea of the stroke range DMs will face in a more typical atmosphere.

Closed-loop simulations have been carried out to illustrate the behavior of the woofer stroke, the tweeter stroke, and the residual phase error rms in terms of the highest mode order used in the MTA matrix. Results are shown in Figure 4.6, where the ATM option is also illustrated. It can be seen that residual errors are kept low with no ATM matrix used for modes of order <4 sent to the woofer.

The main result that comes out of this is that one has to do a trade-off between computational efficiency, tweeter stroke requirement and the woofer order of correction. Figures 4.1 and 4.6 can be used iteratively to find a satisfactory solution. For example, two different options are available if the tweeter stroke obtained does not meet its requirement. First, more modes can be sent to the woofer at the cost of using a return matrix ATM to keep the wavefront errors down. This can reduce the tweeter stroke up to a certain limit as shown in Figure 4.6. The other option is to use a woofer with more actuators across a pupil diameter. This increases the number of modes it can fit accurately and hence increases the number of modes that can be corrected without any return matrix. A new Figure 4.6 can then be generated and the same trade-off can be evaluated for the new case.

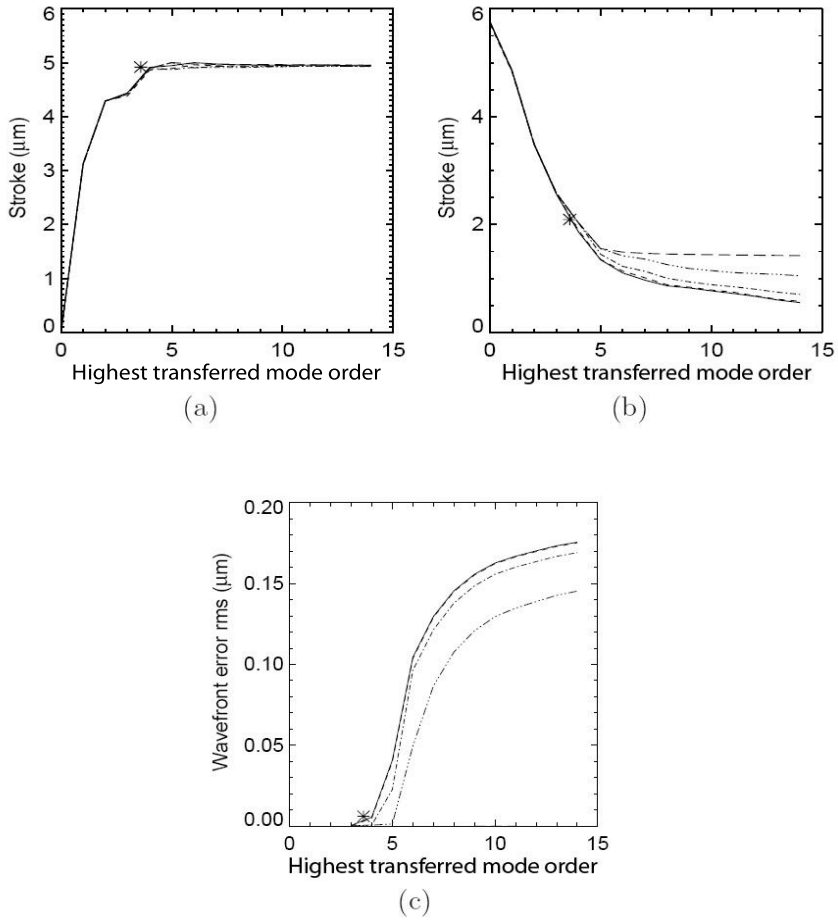

Figure 4.6 Results from closed loop simulations. The (a) woofer stroke, (b) tweeter stroke and (c) wavefront error rms are plotted for different highest mode order sent to the woofer. The impact of using an ATM return matrix on those parameters is also plotted. The solid curve represents no return ATM matrix used; the short-dashed curve, a return on modes of order ≤ 3; the dotted-dashed curve, a return on modes of order ≤ 4; the triple-dotted-dashed curve, a return on modes of order $\leq$; 5 and the long-dashed curve, a return on all the modes. The asterisk represents the option of sending the modes < 4 to the woofer with no return matrix.

4.4 Conclusions

In this paper, we have addressed two critical issues in designing an AO system with two DMs in a woofer-tweeter configuration.

We have first presented a way to determine the woofer order of correction necessary

to keep the tweeter stroke below its requirement using a Monte Carlo and an analytical approach. The dependency of the woofer and tweeter stroke on the woofer order of correction was also determined. These computations are general and can be used in any woofer - tweeter control scheme. The second part of the paper addressed the problem of the command split between the two DMs in the particular case of a Fourier reconstructor. The same approach could be applied to a modally controlled AO system, as long as the modal coefficients are available in real time. It was found that sending only the modes well-reproduced by the woofer reduces significantly the computational power necessary for the correction. The two 1600×69 element matrices needed in a classical approach are replaced by one matrix of 45×69 elements in the specific case of GPI. These two parts give the necessary tools to implement a command split between a woofer and tweeter DM with a Fourier reconstructor and to do the trade-off between computational efficiency and woofer order of correction for a given tweeter stroke requirement.

4.A Appendix A: Analytical PSD computation

4.A.1 Atmospheric Spatial PSD

The goal of this section is to compute an analytical expression of the spatial PSD for an atmosphere without piston, tip and tilt at different positions on the pupil. The integration of the result over the frequencies corrected by each DM will then give the standard deviation of the phase variations to be corrected at the considered position on the pupil. This will then be used to compute the necessary stroke of an actuator situated at this spatial location.

To get to that goal, an expression for the phase without piston, tip and tilt is first

sought. The spatial definition of these three Zerkike polynomials $z(\vec{\rho})$ is

$$z_0 = 1, \tag{A10}$$

$$z_1 = 2\rho\cos\theta, \tag{A11}$$

$$z_2 = 2\rho\sin\theta. \tag{A12}$$

where $\vec{\rho}$ is a spatial position vector normalized so that it is null at the pupil center and that it takes a unit value at its edge. The amplitude of the vectors, $a(\rho)$, in a given atmospheric phase screen $\phi(\vec{\rho})$ is obtained using the following equation (Roddier et al., 1993):

$$a(\vec{\rho}) = \phi(\vec{\rho}) * z(\vec{\rho}). \tag{A13}$$

The atmospheric phase without piston, tip and tilt, $\phi_f(\vec{\rho},\vec{r})$, can be evaluated at the pupil point $\vec{r} = [r_1, r_2]$ normalized to the pupil radius by taking out the contribution of these Zernike polynomials from the initial phase screen:

$$\phi_f(\vec{\rho},\vec{r}) = \phi(\vec{\rho}) - [a_0(\vec{\rho}-\vec{r}) + 2r_1a_1(\vec{\rho}-\vec{r}) + 2r_2a_2(\vec{\rho}-\vec{r})]. \tag{A14}$$

Using Eq. A13, this can be rearranged to give

$$\phi_f(\vec{\rho},\vec{r}) = \phi(\vec{\rho}) * [\delta(\vec{\rho}) - z_0(\vec{\rho}-\vec{r}) - 2r_1z_1(\vec{\rho}-\vec{r}) - 2r_2z_2(\vec{\rho}-\vec{r})]. \tag{A15}$$

$\phi_f(\vec{\rho},\vec{r})$ is then the result of a convolution between the initial phase screen and a spatial filter function taking out the contribution of z_0, z_1 and z_2 from the phase screen. The latter is

$$M_z(\vec{\rho},\vec{r}) = \delta(\vec{\rho}) - z_0(\vec{\rho}-\vec{r}) - 2r_1z_1(\vec{\rho}-\vec{r}) - 2r_2z_2(\vec{\rho}-\vec{r}). \tag{A16}$$

The next step is to derive the analytical expression of the filtered atmospheric PSD

using the following expression found by Roddier et al. (1993) and Conan et al. (1995):

$$PSD(\vec{f},\vec{r}) = W_\phi(\vec{f}) \left| \tilde{M}_z(\vec{f},\vec{r}) \right|^2, \tag{A17}$$

where $\tilde{M}_z(\vec{f},\vec{r})$ is the Fourier transform of the spatial function $M_z(\vec{\rho},\vec{r})$ and $W_\phi(\vec{f})$ is the unfiltered PSD. The vector $\vec{f}$ is the spatial frequency and is the reciproqual of $\vec{\rho}$ in the sense of the Fourier transform.

The Fourier transform of the filter function $M_z(\vec{\rho})$ can be evaluated from Born & Wolf (1975) and the Fourier transform translation property:

$$\tilde{M}_z(\vec{\kappa},\vec{r}) = 1 - \left[\frac{2J_1(\pi\kappa)}{\pi\kappa} + 4i(r_1\cos\theta + r_2\sin\theta)\frac{2J_2(\pi\kappa)}{\pi\kappa} \right] \exp(-\pi i\vec{\kappa}\cdot\vec{r}). \tag{A18}$$

The spatial frequency κ is normalized to unity with respect to the pupil diameter instead of its radius as in the case of f. This implies that $\vec{\kappa} = \frac{1}{2}\vec{f}$. The 2-D vector $\vec{\kappa}$ is defined as $\vec{\kappa} = [\kappa_1, \kappa_2] = |\vec{\kappa}|\,[\cos\theta, \sin\theta]$.

$W_\phi(\vec{f})$ in Eq. A17 is taken to follow a von Karman power spectrum modelised by

$$W_\phi(\eta) = 0.023 r_0^{-5/3} \left(\eta^2 + L_0^{-2}\right)^{-11/6}, \tag{A19}$$

where η is the nonnormalized spatial frequency. Replacing it by κ yields

$$W_\phi(\kappa) = 0.023 D^2 \left(\frac{D}{r_0}\right)^{5/3} \left[\kappa^2 + \left(\frac{D}{L_0}\right)^2\right]^{-11/6}. \tag{A20}$$

The final expression of the spatial PSD is then found by inserting the results from

Eq. A18 and from Eq. A20 in Eq. A17:

$$\begin{aligned} PSD(\vec{\kappa},\vec{r}) &= 0.023D^2\left(\frac{D}{r_0}\right)^{5/3}\left[\kappa^2+\left(\frac{D}{L_0}\right)^2\right]^{-11/6} \\ &\times\left|1-\left[\frac{2J_1(\pi\kappa)}{\pi\kappa}+4i(r_1\cos\theta+r_2\sin\theta)\frac{2J_2(\pi\kappa)}{\pi\kappa}\right]\right. \\ &\left.\times exp\left(-\pi i\vec{\kappa}\cdot\vec{r}\right)\right|^2 \end{aligned} \tag{A21}$$

The variance at the pupil point $\vec{r}=[r_1,r_2]$ of a piston and tip/tilt free atmosphere is obtained by integrating over the whole frequency domain:

$$\sigma^2(\vec{r})=\frac{1}{D^2}\int_{-\infty}^{\infty}\int_{-\infty}^{\infty}PSD(\kappa_1,\kappa_2,\vec{r})d\kappa_1 d\kappa_2 \tag{A22}$$

This result can then be used to evaluate analytically the necessary stroke on a deformable mirror for atmospheric turbulence correction.

4.A.2 Atmospheric Differential Spatial PSD

The interactuator stroke depends on the phase slope between two actuators. Moreover, the best slope correction will be achieved by correcting the mean slope over a subaperture. This can be computed from the differential PSD between those two points. It is found from Eq. A14 that

$$\Delta\phi_f(\vec{\rho})=\Delta\phi(\vec{\rho})-[2(r_{21}-r_{11})a_1(\vec{\rho}-\vec{r})+2(r_{22}-r_{12})a_2(\vec{\rho}-\vec{r})], \tag{A23}$$

where $\vec{r_1}=[r_{11},r_{12}]$ is the inner point, $\vec{r_2}=[r_{21},r_{22}]$ is the outer point and $\vec{r}$ is the center point between $\vec{r_1}$ and $\vec{r_2}$.

The atmospheric phase difference between the two points considered is taken as the mean phase derivative over a subaperture times the actuator pitch d. This translates in

the following definition of $\Delta\phi(\vec{\rho})$:

$$\Delta\phi(\vec{\rho}) = \left[\frac{\partial\phi(\vec{\rho})}{\partial\rho_1} * \Pi(\vec{\rho})\right] d. \tag{A24}$$

where

$$\begin{aligned} \Pi(\vec{\rho}) \quad &= \tfrac{1}{d^2}, \quad -\frac{d}{2D} \leq \rho_1 \leq \frac{d}{2D}, \\ &\qquad -\frac{d}{2D} \leq \rho_2 \leq \frac{d}{2D} \\ &= 0 \quad \textit{elsewhere}. \end{aligned} \tag{A25}$$

Note that the derivative is taken in one direction only for simplicity. This means that the interactuator stroke only of neighbors along that direction is computed. The results are still valid over the whole aperture due to the spatial PSD symmetry. This yields that

$$r_{21} - r_{11} = d, \tag{A26}$$

$$r_{22} - r_{12} = 0. \tag{A27}$$

Eq. A23 becomes

$$\Delta\phi_f(\vec{\rho}) = \left[\frac{\partial\phi(\vec{\rho})}{\partial\rho_1} * \Pi(\vec{\rho})\right] d - 2da_1(\vec{\rho} - \vec{r}). \tag{A28}$$

The expression of $\tilde{M}_z(\vec{\kappa})$ in Eq. A17 for the differential PSD can then be computed as

$$\tilde{M}_z(\vec{\kappa}) = 2i\pi\frac{d}{D}\kappa_1 \mathrm{sinc}\left(\pi\frac{d}{D}\kappa_1\right)\mathrm{sinc}\left(\pi\frac{d}{D}\kappa_2\right) - 4id\cos\theta\frac{2J_2(\pi\kappa)}{\pi\kappa}\exp(-i\pi\vec{\kappa}\cdot\vec{r}). \tag{A29}$$

References

F. Assémat, R. W. Wilson, and E. Gendron, "Method of simulating infinitely long and non stationary phase screens with optimized memory storage," Opt. Express **14**, **3**, 988-999 (2004).

M. Born, and E. Wolf, *Principle of Optics* (Elsevier, 1975).

T. J. Brennan, and T. A. Rhoadarmer, "Advance Wavefront Control: Methods, Devices, and Applications IV," Proc. SPIE **6306**, 63060B (2006).

J.-M. Conan, G. Rousset, and P.-Y. Madec, "Wave-front temporal spectra in high-resolution imaging through turbulence," J. Opt. Soc. Am. A **12**, **7**, 1559-1570 (1995).

S. A. Cornelissen, P. S. Bierden, and T. G. Bifano, "Development of a 4096 elements MEMS continuous membrane deformable mirror for high contrast astronomical imaging," Proc. SPIE **6306**, 630606 (2006).

J. W. Evans, K. Morsinski, L. Reza, S. Severson, L. Poyneer, B. A. Macintosh, D. Dillon, G. Sommargen, D. Palmer, D. Gavel, and S. Olivier, "Extreme adaptive optics testbed: high contrast measurements with a MEMS deformable mirror," Proc. SPIE **5905**, 303-310 (2005).

P. Hampton, R. Conan, C. Bradley, and P. Agathoklis, "Control of a woofer tweeter system of deformable mirrors," Proc. SPIE **6274**, 62741Z (2006).

G. Herriot, S. Morris, S. Roberts, J. M. Fletcher, L. K. Saddlemyer, G. Singh, J.-P. Véran, and E. H. Richardson, "Innovation in Gemini Adaptive Optics System Design," Proc. SPIE **3353**, 488-499 (1998).

G. Herriot, P. Hickson, B. L. Ellerbroek, D. A. Andersen, T. Davidge, D. A. Erickson, I. P. Powell, R. Clare, L. Gilles, C. Boyer, M. Smith, L. Saddlemyer, and J.-P. Véran,

"NFIRAOS: TMT narrow field near-infrared facility adaptive optics," Proc. SPIE **6272**, 62720Q (2006).

S. Hu, B. Xu, X. Zhang, J. Hou, J. Wu, and W. Jiang, "Double-deformable-mirror adaptive optics system for phase compensation," Appl. Opt. **45**, 2638-2642 (2006).

B. A. Macintosh, M. Troy, R. Doyon, J. Graham, K. Baker, B. Bauman, C. Marois, D. Palmer, D. Phillion, L. Poyneer, I. Crossfield, P. Dumont, B. M. Levine, M. Shao, G. Serabyn, C. Shelton, G. Vasisht, J. K. Wallace, J.-F. Lavigne, P. Valée, N. Rowlands, K. Tam, and D. Hackett, "The Gemini Planet Imager," Proc. SPIE **6272**, 62720L (2006).

K. Morzinski, J. W. Evans, S. Severson, B. Macintosh, D. Dillon, D. Gavel, C. Max, and D. Palmer, "Characterizing the potential of MEMS deformable mirrors for astronomical adaptive optics," Proc. SPIE **6272**, 627221 (2006).

L. A. Poyneer, D. T. Gavel, and J. M. Base, "Fast Wavefront Reconstruction in Large Adaptive Optics Systems With Use of the Fourier Transform," J. Opt. Soc. Am. A **19**, 2100-2111 (2002).

L. A. Poyneer, and J.-P. Véran, "Optimal Modal Fourier-transform Wavefront Control," J. Opt. Soc. Am. A **22**, 1515-1526 (2005).

E. Roddier, M. J. Northcott, J. E. Graves, and D. L. McKenna, "One-dimensional spectra of turbulence-induced Zernike aberrations: time-delay and isoplanicity error in partial adaptive compensation," J. Opt. Soc. Am. A **10**, **5**, 957-965 (1993).

CHAPITRE 5

CONCLUSION

Cette thèse, qui se divise en trois parties, a comme but commun l'amélioration des techniques d'imagerie directe des exoplanètes. Elle s'inscrit dans le développement du *Gemini Planet Imager* (GPI) qui utilisera un spectromètre à champ intégral (SCI) pour atténuer le bruit de tavelure et pour caractériser les compagnons détectés et qui devra séparer la correction du front d'onde entre deux miroirs déformables pour obtenir la qualité de front d'onde recherchée.

La première partie a consisté à observer l'étoile GQ Lup et son compagnon de faible masse dans les bandes spectrales JHK à l'aide de la caméra NIFS, un SCI présentement en fonction sur le télescope Gemini Nord. Le bruit de tavelure a été atténué à l'aide de l'imagerie différentielle angulaire (IDA) en bande J et H pour augmenter le rapport signal-sur-bruit du spectre du compagnon d'un facteur ~ 4 en J et ~ 2 en H. Une méthode y a été développée pour évaluer et compenser l'impact de l'IDA sur le spectre du compagnon. Une comparaison des spectres avec ceux d'objets du champ et d'autres objets jeunes nous a permis de contraindre son type spectral infrarouge à $L1 \pm 1$. La comparaison avec une grille de spectres synthétiques générés à l'aide de modèles atmosphériques nous a permis de contraindre la température effective du compagnon à $T_{eff} = 2400 \pm 100$ et sa gravité à $\log g = 4.0 \pm 0.5$. Le flux du spectre synthétique correspondant a été calibré à l'aide de nos données et d'autres observations trouvées dans la littérature. La luminosité de GQ Lup b ($\log(L/L_{\odot}) = -2.47 \pm 0.28$) obtenue en intégrant le flux sur toutes les longueurs d'onde a ensuite été comparée aux prédictions des modèles évolutifs DUSTY pour obtenir une estimation de $8 - 60\ M_{\rm Jup}$ pour la masse du compagnon.

Au chapitre 3, la conception et l'évaluation des performances en laboratoire d'un SCI optimisé pour l'imagerie à haut-contraste sont présentées. Différents algorithmes ti-

rant avantage de la corrélation spectrale du bruit de tavelure, plus précisément la simple différence (SD), la double différence (DD), la déconvolution spectrale et les jumeaux spectraux, sont utilisés pour l'atténuer. Ainsi, nous trouvons que la SD utilisée sur les données d'un SCI est au minimum aussi performante qu'une SD utilisée sur les données d'une caméra multi-canaux, le bruit de tavelures étant atténué d'un facteur entre 2 et 10 selon la séparation angulaire dans nos données obtenues en laboratoire. De plus, nous trouvons que l'algorithme des spectres jumeaux est le plus performant permettant une augmentation du rapport signal-sur-bruit d'un facteur ~ 12 pour un compagnon méthanique et d'un facteur ~ 3 pour un compagnon non-méthanique. Ceci est plus que deux fois mieux que le deuxième algorithme le plus performant, la déconvolution spectrale.

Finalement, la nécessité d'utiliser deux miroirs déformables, *woofer* et *tweeter*, provient essentiellement de la limitation actuelle de la course des actionneurs du *tweeter* de type MEMS à ~ 2 μm alors que $\sim$ 10μm sont nécessaires à la correction de la turbulence atmosphérique. Ainsi, nous présentons une approche Monte Carlo et analytique pour déterminer l'ordre de correction du *woofer* et la course de ses actionneurs nécessaire pour compenser la turbulence atmosphérique en fonction de la course maximale des actionneurs du *tweeter*. Nous présentons ensuite une méthode efficace de séparation de la commande entre les deux MDs lorsqu'un reconstructeur de Fourier est utilisé. Cette méthode permet de réduire significativement le nombre de calculs nécessaires à l'accomplissement de cette tâche.

Ainsi, avec son amélioration significative de la correction du front d'onde comparativement aux systèmes actuels couplée avec l'utilisation d'un coronographe et un spectromètre à champ intégral optimisé pour l'imagerie à haut-contraste, GPI nous permettra de détecter des compagnons des millions de fois plus faibles que leur étoile hôte et ce, à une fraction d'une seconde d'arc. Nul doute que GPI ouvrira une nouvelle ère dans l'étude des exoplanètes.

Annexe I

Permissions de l’éditeur

Annexe II

Déclarations des coauteurs des articles